Modeling of high speed remote laser cutting of electrodes for lithium-ion batteries

by

Dongkyoung Lee

A dissertation submitted in partial fulfillment
of the requirements for the degree of
Doctor of Philosophy
(Mechanical Engineering)
In The University of Michigan
2012

Doctoral Committee:

Professor Jyotirmoy Mazumder, Chair
Professor J. Wayne Jones
Professor Ann Marie Sastry
Associate Professor Kevin Patrick Pipe

To my family and my 20s

ACKNOWLEDGEMENTS

In my early 20s, I had a goal to be an independent individual at the age of thirty. To be the independent individual, I defined four types of independence: Financial independence, Daily living independence, Spiritual independence, and Academic independence. Even though, there are many debates, my thought was that the academic independence can be achieved by accomplishing a Ph.D. study. At this moment, my heart is overflowing with joy due to the expectation of achieving my goal as completing the last independence, the Academic independence. I knew that this cannot be reached without sincere help and support from invaluable people.

First and foremost, I wish to express my deepest thanks to my advisor, Professor Jyotirmoy Mazumder, for his patient guidance, inspiration, encouragement and support for my Ph.D. study. His guidance throughout my entire studies enabled this work. I also truly appreciate my dissertation committee — Professor J. Wayne Jones, Professor Kevin Patrick Pipe, and Professor Ann Marie Sastry — for their insights and critiques in finishing this PhD thesis.

Also, I would like to express gratitude to the University of Michigan and Fraunhofer U.S.A. for the financial support through their "Alternative Energy for Transportation" program for this research. I would like to take time to thank Hans J. Herfurth and Rahul Patwa for all their helps during the studies.

TABLE OF CONTENTS

LIST OF FIGURES

LIST OF TABLES

NOMENCLATURE

A	Area, m^2
c	Concentration; Degree of continuity
C	Constant
C_{pl}	Liquid constant-pressure specific heat, J/kg·K
C_{ps}	Solid constant-pressure specific heat, J/kg·K
$\bar{C}_p$	Average constant-pressure mixture specific heat, J/kg·K
$\bar{C}_{pl}$	Average constant-pressure specific heat of liquid, J/kg·K
$\bar{C}_{ps}$	Average constant-pressure specific heat of solid, J/kg·K
d_s	Stabilized depth
D	Mass diffusion coefficient, m^2/s
$\boldsymbol{e_x, e_y, e_z}$	Unit vectors in x,y,z directions, respectively
f	Mass fraction
F	Force or speed function, m/s
F_{evap}	Speed function of the L/V interface due to evaporation, m/s
g	Volume fraction
h	Enthalpy, J/kg
$H_{\varepsilon,c}(\phi)$	Smoothing function
$\mathbf{i}$	Incoming ray

I	Second-order identity tensor
I	Laser intensity, W/m^2
k	Thermal conductivity, W/m·K
K	Permeability
L_m	Latent heat of fusion, J/kg
L_v	Latent heat of vaporization, J/kg
$\dot{m}$	Mass flux, kg/s
$\dot{m}''$	Mass flux per area, kg/s·m^2
max	MAX function, which calculates maximum value among all its arguments
min	MIN function, which calculates minimum value among all its arguments
n	Normal vector at liquid-vapor interface
p	Pressure, Pa
p_g	Hydrostatic pressure, Pa
p_h	Hydrodynamic pressure, Pa
p_l	Radiation pressure, Pa
p_σ	Surface tension pressure, Pa
p_v	Vaporization pressure, Pa
P	Power, W
$\dot{q}$	Energy flux, J/s
$\dot{q}''$	Energy flux per area, J/s·m^2
$\dot{q}''_{L/V}$	Spatial laser beam distribution after multiple reflections per area, J/s·m^2
r	Reflected ray
r	Radial distance, m

R_v	Specific gas constant, J/kg·K
t	Time, s
t_r	Rising time, s
t_s	Stabilized time, s
T	Stress tensor, N/m^2
T	Temperature, K
T_m	Melting temperature, K
T_b	Boiling temperature, K
u	Fluid velocity vector, m/s
u	x-direction velocity, m/s
u_v	Velocity of vapor, m/s
v	y-direction velocity, m/s
V_s	Scanning speed, mm/s
w	z-direction velocity, m/s; Beam radius
x	Spatial vector
x	Cartesian coordinate along beam scanning direction
y	width-wise Cartesian coordinate
z	depth-wise Cartesian coordinate

Physical constants

g	Gravity, 9.8 m/s
R	Gas constant, 8.314×10^{15} J/K·mol

σ Stefan-Boltzmann constant, 5.67×10^{-8} W/m$^2 \cdot$K^4

Greek letters & Symbols

α	Incident angle, °; Relaxation factor
δ	Delta function
ε	Emissivity; smoothing factor
κ	Curvature
μ	Viscosity, m^2/s
ρ	Density, kg/m^3
σ	Surface tension, N/m
θ	Angle between reference direction and the line from the origin
ϕ	Level set function for liquid-vapor interface
ϕ_0	Level set function
Ψ	Level set function for solid-liquid interface
Γ	Interface; diffusivity
Φ	Dependent variable
Ω	Domain
$\partial\Omega$	Boundary of domain Ω
∇	Gradient operator in tensor form
∇_s	Surface nabla

Superscripts & Subscripts

0	Initial value
*	Value from the previous iteration; Guessed value
AE	Active electrode materials
b	Normal boiling point; bottom
B	Bottom
CC	Current collectors
e	East
E	East
evap	Evaporation
l	Liquid
liq	Liquid
laser	Laser
L/V	Liquid-vapor interface
m	Metling
n	North
N	North
s	Solid; Evaporating surface; Scanning speed; South
S	South
t	Top
T	Transpose; Top
v	Vapor; Vaporization

vap	Vapor
w	West
W	West

Abbreviations

CNC	Computer Numerical Control
CW	Continuous
EV	Electric Vehicle
EDX	Energy-Dispersive X-ray spectroscopy
HAZ	Heat Affected Zone
HEV	Hybrid Electric Vehicle
L/V	Liquid-Vapor Interface
PHEV	Plug-in Hybrid Electric Vehicle
S/L	Solid-Liquid Interface
SEM	Scanning Electron Microscope
SIMPLEC	Semi-Implicit Method for Pressure-Linked Equations Consistent
TEM	Transverse Electromagnetic

ABSTRACT

This research investigates the underlying physics of the laser cutting of electrodes for lithium-ion batteries and validates important findings experimentally. The mathematical model considers heat transfer, mass transfer, fluid flow, melting, solidification, evaporation, kinetic Knudsen layers, multiple reflections, free surface evolution, and composite materials.

First, the developed model is applied to investigate effects of laser beam modes on the laser-material interaction. Cylindrical TEM_{00}, TEM_{01*}, TEM_{22}, and Top-hat laser beam are selected. Overall characteristics such as, response time, depth, width, and absorptivity of the proposed cases are investigated. The criteria of keyhole collapse are quantitatively obtained. The result indicates that the TEM_{00} and Top-hat laser beam cases are more efficient for the laser cutting process.

Second, the model is applied to the laser cutting of current collectors. Laser parameter thresholds for cutting are obtained. Moreover, L/V interface geometry, melt pool flow, and temperature distribution are examined. The analysis shows interaction characteristics of current collectors with the laser. Furthermore, results present the formation of crests and two consecutive deep penetration holes as well as explain possibilities of forming a spatter, recast layer, and a neck.

Third, the model is applied to the laser cutting of electrodes. Interesting results near the material interface between current collectors and active electrode materials are observed. For the anode, the L/V interface in the graphite region shows a smooth and clean surface, and a two-level surface is observed near the material interface. For the cathode, the deep penetration hole shows an uneven surface, crests, and a protrusion in the $LiCoO_2$ region. The narrower deep penetration hole forms near the material interface.

Finally, experimental results are presented. The kerf widths are compared near thresholds of the laser cutting of current collectors. The kerf width of electrodes and composition change along the cut surface of electrodes are validated. The theoretical prediction shows a reasonable agreement with experimental observations. Moreover, the optimum range of laser parameters providing both high speed and high quality cutting are obtained.

The proposed model can be utilized to predict and prevent defects, thermal stress, significant heat generation, and eventually catastrophic failures of the entire module.

CHAPTER I

INTRODUCTION

1.1. Background

Increasing numbers of natural disasters due to climate change alert most nations in the world to take account this issue with deep consideration. Climate change leads to the definition of long-term sustainability of societies [1]. A long-term sustainable society looks forward to the reduction of carbon emissions, which are the majority of greenhouse gases. According to the International Energy Agency (IEA), one of the main sources of CO_2 emissions is the transportation sector, representing 23% of global CO_2 emissions in 2009 [2]. Reducing carbon emissions in vehicles provides significant impacts to mitigate global carbon emissions. Reducing carbon emissions in vehicles became a more important issue in the United States after presidential memoranda were signed on January 26, 2009. One memorandum is directed to the Department of Transportation to set higher fuel efficiency standards for carmakers in the 2011 model year; the other is directed to the Environmental Protection Agency (EPA) to reconsider California's request to impose its own strict limits on vehicle emissions [3].

To meet these strict emission regulations, many automakers are developing new technologies, such as biofuels, fuel cells, and electric and hybrid vehicles. Among these

new technologies, battery-based hybridization of gasoline and diesel engines has been adapted within the last few years due to its efficiency, the availability of technologies and nation-wide infrastructures. Furthermore, according to a report by the Boston Consulting Group [4], estimated 14 million electric and hybrid vehicles may be sold in 2020 in the world's four largest automotive markets of North America, Japan, China, and Western Europe.
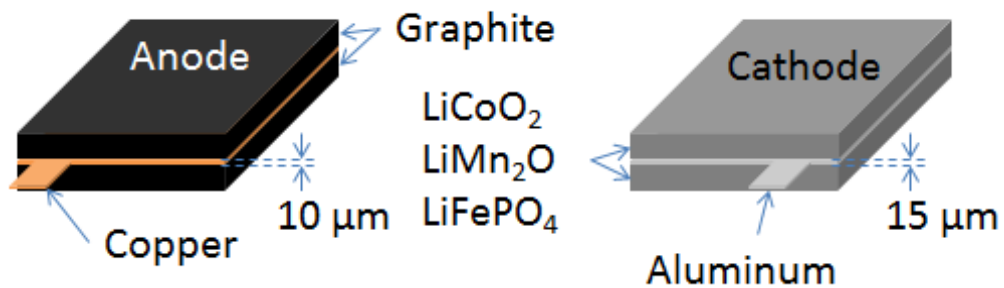
Figure 1.1. Electrodes

To develop more efficient hybrid and electric vehicles, an understanding of automotive battery technology is essential. Among many of the battery technologies, the lithium ion battery represents the most promising technology for the abovementioned vehicles due to their high energy-to-weight ratio, high power density, high energy density, and lighter weight than other energy-equivalent secondary batteries [5, 6]. A lithium-ion battery cell consists of the positive electrode (the cathode), the negative electrode (the anode), electrolyte, and separator. Electrodes are shown in Figure 1.1. An anode is usually graphite-coated copper and a cathode is lithium metal oxide-coated aluminum. Popular lithium metal oxides are lithium cobalt oxide ($LiCoO_2$), lithium iron phosphate ($LiFePO_4$), and lithium manganese oxide ($LiMn_2O_4$). Electrode thicknesses

can range from 10 μm (uncoated) to 200 μm (coated) depending on the cell design (cylindrical or planar) and the electrode type (cathode or anode). The brief charge and discharge principles of lithium-ion batteries are depicted in Figure 1.2. Copper and aluminum foils are positioned at the center and used as a current collector, conducting the current in and out of the cell. Graphite and lithium-metal oxide are called an active electrode material, where lithium ions leave the lithium-metal oxide during charge and intercalate into the graphite by electrochemical reaction. The reverse happens on discharge. A liquid electrolyte conducts lithium ions, acting as a carrier between the cathode and the anode when the lithium-ion battery passes an electric current through an external circuit. The separator prevents short-circuiting between the cathode and anode while allowing the flow of lithium ions and electrons during charge and discharge states.
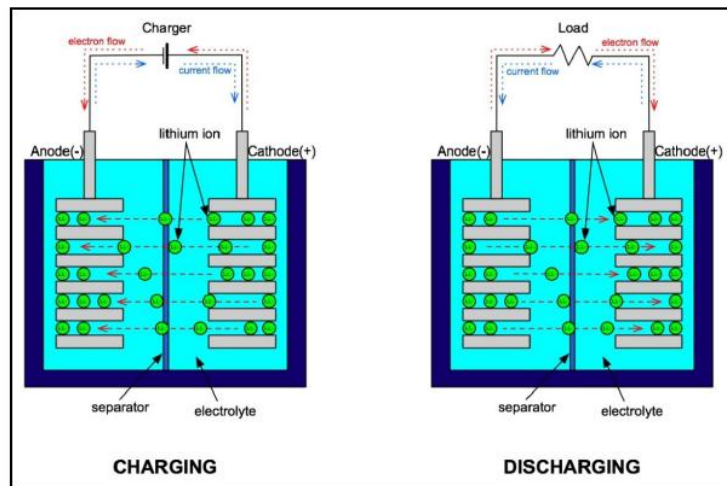
Figure 1.2. Charge and discharge principles of lithium-ion battery [7]

Many studies have focused on improving lithium ion battery performance. Two of the main streams of research are the development of the electrode materials and battery manufacturing processes [8]. Many researchers have been focused on developments of

electrode materials. Broussely *et al.* [9] described a short historical perspective of the positive materials by comparing battery performance, such as specific capacity. Recently, more attention has been focused on cathode materials in order to improve capacity for lithium ion batteries with nanotechnology [10-13]. Furthermore, to improve the capacity of the anode materials, silicon or silicon-based materials have been suggested as potential alternatives for the next generation of lithium ion battery systems [14-18].

1.2.   Lithium-ion Battery Manufacturing

Lithium-ion battery manufacturing processes are also an important issue to improve the battery performance. Due to the variety of materials, sizes, and formats of lithium ion battery cells, it is difficult to characterize lithium ion battery production with a single manufacturing process. However, these share key manufacturing process. In this study, the manufacturing process of prismatic lithium ion cells is described. The manufacturing process of prismatic lithium ion cells is divided into two parts: electrode coating and cell assembly [19]. The electrode coating process is shown in Figure 1.3 and explained as follows. First, a powder of active electrodes is mixed with a conductive binder and additives to form a slurry. This slurry is coated on both sides of current collector foils. The coated foils are compressed to satisfy a required thickness of coating layers, since the volumetric energy storage capacity of anode and cathode materials are usually different. After obtaining the desired thickness, the coated foils are dried, calendered to make the thickness of the coated foils more uniform, and then cut to the required dimensions.
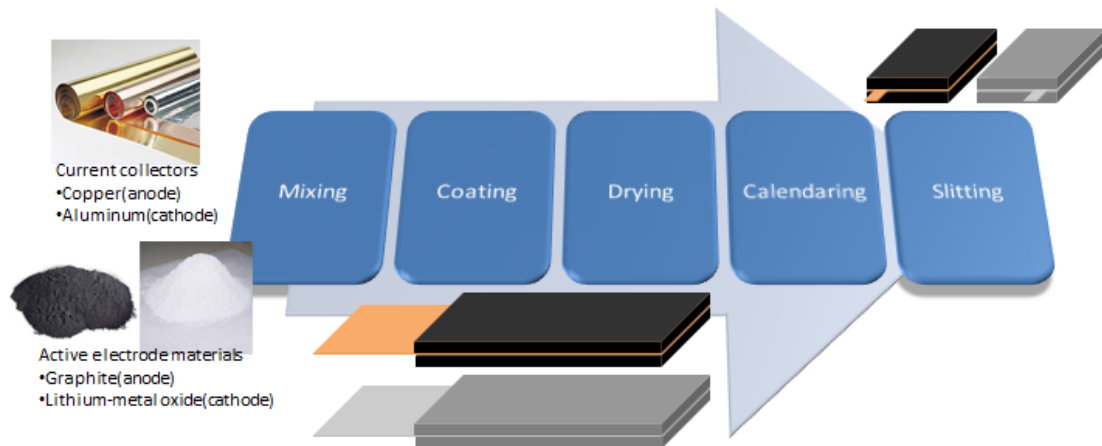
Figure 1.3. Electrode coating process
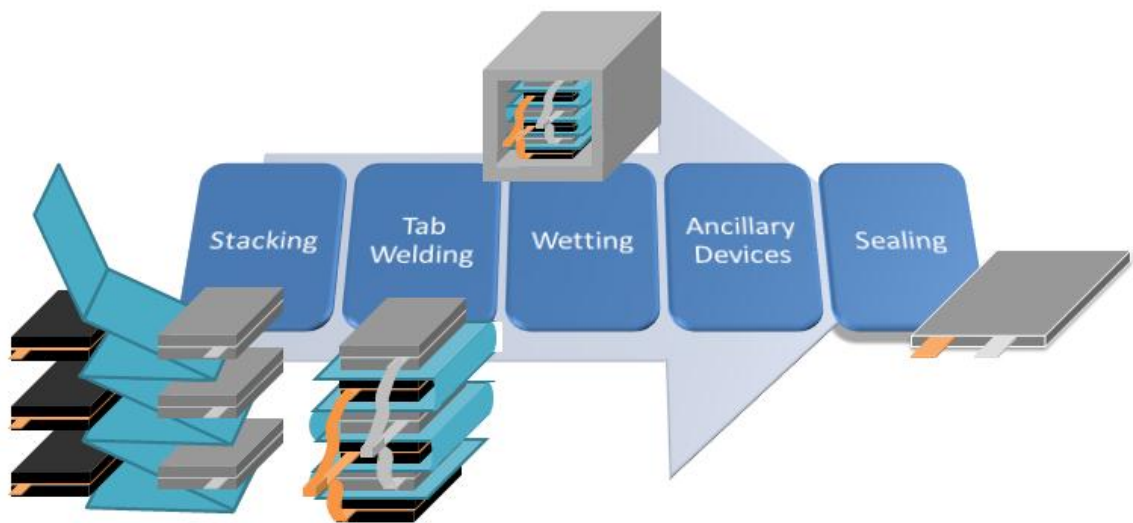
Figure 1.4. Cell assembly process

The cell assembly process is shown in Figure 1.4. The anode and cathode are stacked alternately and kept apart by the separator. The separator is applied in a long strip wound in a zig zag fashion between alternate electrodes in the stack. Tabs are welded to the cathode and anode to provide electrical connections. The connected electrodes are inserted into a pouch. The pouch is vacuumed and filled with electrolyte (called wetting). Ancillary components, such as vents and safety devices, are attached and the pouch is

sealed. After this cell assembly process is finished, individual cells are then packed together into modules, which are further integrated with other systems into a complete battery pack.

(a) Fast moving mirror **(b)**

y

x

Pressure gauge

F-theta lens

Gas inlet

Moving stage

Laser beam

Focusing lens

Nozzle

y

x

CNC Machine stage
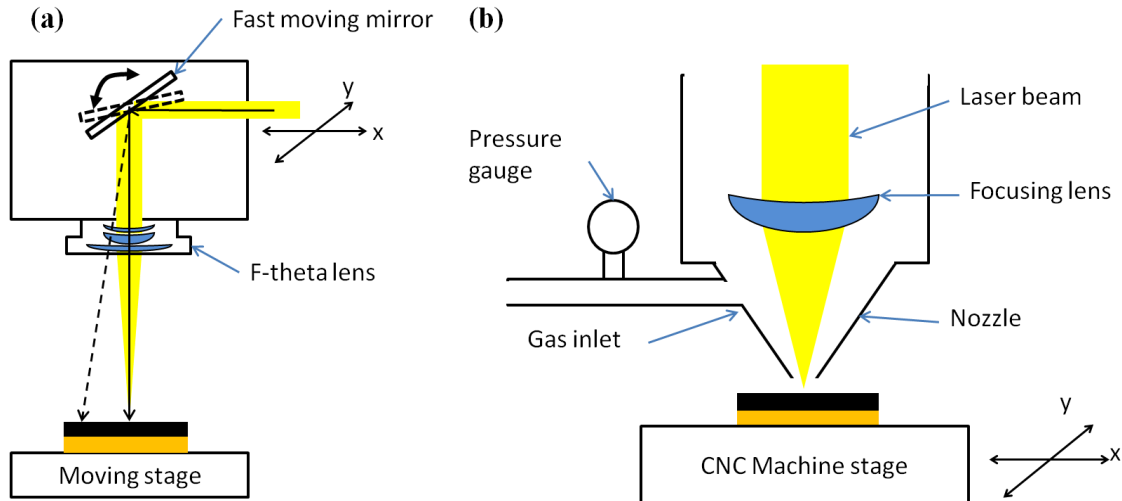
Figure 1.5. Schematics of (a) remote laser cutting (b) conventional laser cutting

1.3.   Remote laser cutting technology

In conventional laser cutting, as seen in Figure 1.5 (b), the cutting head includes fixed beam delivery optics, cutting gas delivery system, vision system and other options as required by specific cutting processes. The focusing optics focuses the collimated laser beam on the workpiece to a small spot size. The nozzle placed at the end of the cutting head has a very small opening to supply assist gas that ejects the melt from the cut kerf. The cutting head is typically mounted on a robot or on the vertical axis of a CNC machine tool system. Such a machine tool system must meet stringent system requirements regarding precision, accuracy and repeatability at high cutting speeds. In contrast to scanning systems, a conventional laser cutting machine requires significant

capital investment for fast moving linear axis systems. These systems are more bulky and massive, take more work space, and have lower accuracy that decreases further as their size gets larger. Moreover, the dynamics of the system constrain the maximum possible speed and acceleration. The programming of the cut path also requires special attention as the geometry of the cutting path becomes complex. High cutting speed and high cut quality can be achieved in conventional laser cutting; however optimization of a large number of process variables that affect the cutting quality is required. Besides common process parameters such as laser power, speed, spot size etc, for both conventional and remote laser cutting process, there are a number of other critical factors that affect the cut quality only in the conventional cutting process, such as nozzle size, distance from nozzle tip to the top of the material surface, cutting gas type, gas pressure, and flow rate.

Remote cutting technology, as seen in Figure 1.5 (a), is a relatively new laser cutting process, started since late 90s [20-22]. In general, remote cutting can be defined as a laser cutting process with focal length larger than in conventional laser cutting process [20]. The longer working distance allows small changes of the position of a mirror or optics effect fast and large deflections of the laser beam focus on the workpiece. The two essential components that have enabled remote cutting technology are advancements in (1) optical beam scanning systems and (2) high brightness lasers. Well established galvanometer scanner technology comprises of high-performance rotary motors that produce high dynamic beam deflection. Due to the low mass and inertia of these systems, high speeds and acceleration of up to 15 m/s and 10 g, respectively, can be achieved with the latest digital scanners. The image field size and the working distance are directly proportional to the focal length of the F-Theta focusing lens. In order to

generate larger image field size, longer focal length is required, which in turn requires better beam quality to generate small spot sizes. With the availability of high power and high brightness lasers such as fiber and disk lasers with excellent beam quality, it is possible to achieve very small spot sizes (< 20μm) with high power intensities (>10^8 W/cm^2).

In remote laser cutting, the material is cut by a combination of very high energy densities in a very small laser spot and fast beam movement. High cutting speeds result in very short cycle times and a minimal Heat Affected Zone (HAZ) given the thermal nature of the process. This is especially important for thin materials where conventional laser cutting has its limitations and has a larger thermal effect on the piece being cut. Larger image field sizes enable very flexible cutting processes, which can accommodate different electrode shapes and sizes while keeping the electrode stationary. Therefore, the high speed, high accuracies and repeatability can be achieved using the remote laser cutting technology.

1.4.   Motivations and objectives

From the manufacturing process of lithium ion cells, several problems have been reported during the cutting process. Currently, die cutting and rotary knife slitting have been used to cut the prismatic and cylindrical electrodes, respectively [23-25]. Both techniques require relatively expensive tooling that wears over time. This tool wear results in process instability and requires additional cost and downtime to replace the worn tools. Furthermore, redesign of mechanical cutting processes demanding extra

expenses is an inevitable step, since cell specifications vary depending on applications such as electronic devices and electric vehicles. The most significant disadvantage due to the tool wear is the problem of inconsistent cut surfaces with defects, which are characterized by burrs, delamination, edge bending, and micro-sized material attachments as shown in Figure 1.6. These defects cause the penetration of the separator giving rise to internal short circuits. Moreover, the quality of a poor cut surface makes electrodes susceptible to higher electrical stress, which can lead to significant heat generation and possible thermal runaway [19]. Internal short circuits and significant heat generation can eventually result in catastrophic failures of the entire system.

The abovementioned problems can be solved by using laser cutting, which is proven and widely utilized in industry [26] as well as is a high efficient and reliable manufacturing method. It has many advantages, such as no tool wear due to the contact-free process, high energy concentration, low noise level, fast processing speed, very narrow Heat Affected Zone (HAZ), applicability to nearly all materials, and flexibility of laser power [26]. Most importantly, laser cutting is relatively easily applicable to different cell specifications with less cost, since redesign of laser cutting processes is relatively simple and cheap compared to mechanical cutting processes.

Although laser cutting has many advantages for the electrode cutting process, the application of the laser cutting to size the lithium ion batteries has been investigated by few researchers. Achievable cutting speed and cut quality of the electrodes for the lithium-ion battery were studied with a pulsed solid state laser and a single mode fiber laser in combination with fixed optics and 2D scanning optics [24]. High speed laser cuttings of electrodes for the lithium-ion battery using single mode fiber lasers were also

9

investigated [25]. This study illustrated the achievable highest cutting speed, the effect of the focus beam and the number of cutting passes. In another study, a comparison between a CW laser and a pulsed laser cutting electrodes for lithium-ion batteries was examined [27]. Achievable cutting speeds, qualities, and the application areas for the two operating modes were also discussed. These experimental conclusions have been derived through a trial and error process. Investigating underlying physical phenomena with numerical analysis allows us to fully utilize the remote laser cutting of electrodes for lithium-ion batteries. To the best of the author's knowledge, although the understanding underlying physics during the high speed remote laser cutting of electrodes for the lithium-ion battery is important to improve the battery performances, it has not yet been studied.

Laser cutting involves phase changes, such as solidification, melting, and evaporation. A high evaporation speed forms the region, called the Knudsen layer, where the continuum hypothesis fails, at the Liquid-Vapor (L/V) interface. Furthermore, a deep penetration hole is observed prior to accomplishing the cutting, which requires full penetration of the materials. Laser energy can accumulate inside a deep penetration hole by multiple reflections so that energy absorption increases significantly. This increased energy absorption in turn expedites the penetration. Due to these physical characteristics, the modeling of the laser cutting of electrodes for lithium-ion batteries can be started from the mathematical model of laser-material interaction.
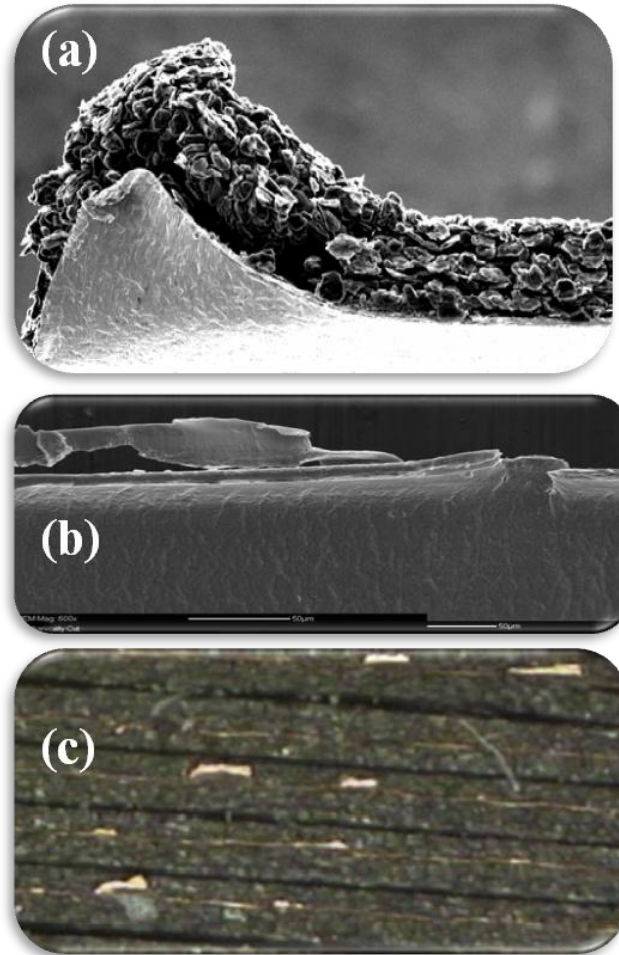
Figure 1.6. Defects from mechanical cutting process; (a) edge bending, (b) Micro sized material attachments [24], and (c) inconsistent cut quality [24]

The melt pool and heat flows, as well as intensity and pressure distributions during the laser-material interaction, are major factors affecting process quality. Many researchers have worked to understand the influence of these physical phenomena on the laser-material interaction. Chan and Mazumder [28] developed a simple one-dimensional steady-state laser-material interaction model. They examined the damage caused by vaporization and liquid expulsion. This mathematical model evolved to two- and three-dimensions. A two-dimensional model was developed not only for investigating material damage due to melting and vaporization [29], but also for analyzing effects of assist gas

and multiple reflections inside the cavity [30]. Ki *et al.* [31-35] developed a mathematical three-dimensional self-consistent laser-material interaction model with the aid of the level-set method. These studies included fluid flow, heat transfer, solidification, melting, evaporation, multiple internal reflections, free surface evolution, and surface forces on mild steel. Different from these single materials, electrodes are a sandwiched composite material. Due to this sandwiched shape layering, the interface of the each material must be carefully treated. On the material interface, melted materials are mixed and composition changes. The variation of composition results in varying mixture properties. These mixture properties affect the behaviors of the laser cutting of electrodes dramatically. Therefore, the objectives of this study is to understand physical phenomena affecting the cut quality and obtain robust laser parameters providing good quality and high speed during laser cutting of electrodes for lithium-ion batteries.

1.5.   Dissertation outline

Prior to considering the sandwiched composite material directly, understanding the effects of laser beam mode and behaviors of each material are a crucial step. Figure 1.7 shows the model development procedure. This work consists of five parts. First, in Chapter II, the general concepts and technical details of modeling of the high speed remote laser cutting will be described. In Chapter III, effects of laser beam modes on the laser-material interaction will be investigated with the developed model. In Chapter IV and Chapter V, the developed methods will be applied to the laser cutting of current

collectors and electrodes, respectively. Chapter VI will present the experiments conducted to verify the proposed cutting model.
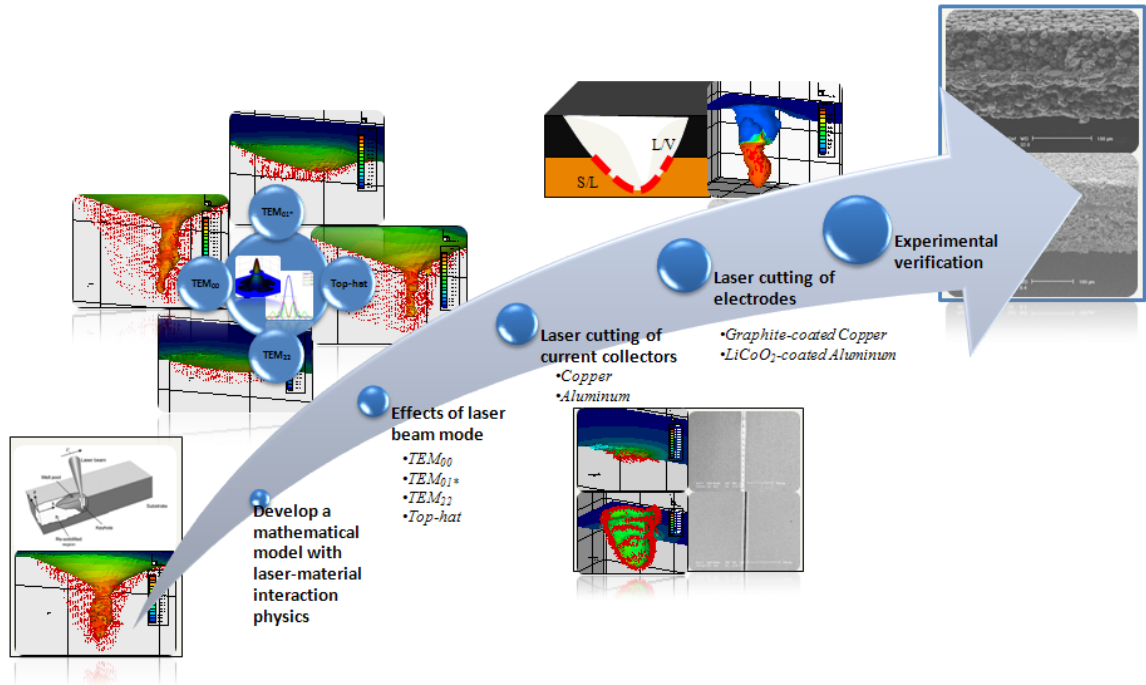
Figure 1.7. Model development procedure

In Chapter II, a mathematical model is established with the laser-interaction physics. The mathematical model of laser-interaction physics includes heat and fluid flow, composition change, multiple reflections, recoil pressure, surface tension, evaporation, solidification, and melting. Furthermore, with the assistance of the level-set technique, the liquid-vapor interface could be tracked in a self-consistent manner. With these consideration of the laser-interaction physics, the mathematical model of the high speed laser cutting of electrodes is developed as considering the physical phenomena, such as composition variation, changes of material properties with mass fractions, and absorption characteristics, near the material interface of current collectors and active electrode materials. The mathematical model developed in this chapter is for laser cutting

of electrodes for lithium-ion batteries. When applying this model to single materials, such as steel, copper, and aluminum, proper modifications need to be made and summarized in this chapter. Numerical computation are adapted to solve the proposed mathematical model.

In Chapter III, the developed mathematical model is applied to investigate the effect of laser beam modes on physical characteristics of the laser-material interaction. This model is originally developed for laser keyhole welding. This section provides a better understanding of keyhole formation and collapse under the given laser beam modes. Cylindrical TEM_{00}, TEM_{01*}, TEM_{22}, and Top-hat laser beam shapes are selected. Cylindrical TEM_{00}, TEM_{01*}, and Top-hat have been chosen due to their popularity as commercially available lasers and a high order beam mode, namely TEM_{22}, is also considered for comparison. Continuous (CW) CO_2 laser is selected. Laser beam power, scanning speed, and a focused beam radius are 4 kW, 16.93 mm/s, and 250 μm, respectively. Equations for these laser beam modes are derived to have the same average laser power. Steel plates with 5mm are assumed as a target material. The response time and overall characteristics of the proposed cases are investigated. The initial, transition, and final stages are defined based on response times to illustrate the evolution and physical phenomena of the melt pool. In addition, a dimensionless parameter is derived based on surface pressure balance to understand the deep penetration hole collapse quantitatively. The analysis of keyhole collapse with the dimensionless parameter shows strong relationship between the deep penetration hole collapse and the dimensionless parameter. Furthermore, melt pool flow, temperature, recoil pressure, and intensity field are investigated, within the defined stages. The four flow patterns are observed: the front-

wall strong flow pattern, the liquid material removal pattern following the L/V interface, the swirling vortex pattern initiated just below the L/V interface, and the circular motion pattern in the back and bottom of the rear melt pool. Specific characteristics of each laser beam mode are discussed based on these four patterns, recoil pressure, and intensity field. The model provides interesting conclusions with the given laser parameters. The TEM_{00} and Top-hat laser beam case are of the deep penetration mode. TEM_{01*} and TEM_{22} are of conduction mode. The deep penetration mode has a broader melt pool area and deep penetration hole, indicating that it might be more efficient for the welding, drilling, and cutting process. However, the unstable deep penetration hole is still a drawback. The conduction mode is a stable process with gradual depth grew and less severe fluctuation during the entire simulation, Hence, it could be utilized more efficiently for surface treatment processes, which change the micro structure of the surface, because it has a wide melt pool area and no substantial geometry changes. Hence, understanding physical phenomena under the given laser parameters and laser beam modes provides confidence on the model before applying this model to the laser cutting of electrodes for lithium-ion batteries.

In Chapter IV, behavior of the current collector materials such as copper and aluminum is studied numerically with the proposed mathematical model. Since the current collector materials are coated by the active electrode material on both top and bottom, understanding the behavior of the current collector material is essential and a pre-requisite step before expanding this modeling task to the electrode materials. Therefore, this mathematical model has been run on the copper and aluminum with several sets of the laser parameters such as scanning speed and laser power. The ranges of the laser

power and scanning speed are 50W to 450 W and 1000 mm/s to 5000 mm/s, respectively. A CW single mode fiber laser with a focused beam diameter of 11 μm is used. The thicknesses of the copper and aluminum are assumed to be 10 μm and 15 μm, respectively. Based on the simulation results, the characteristics of the laser cutting of copper and aluminum are analyzed and discussed, taking into consideration the penetration time, width, depth, and absorptivity. Based on the obtained results, laser parameter thresholds are provided for the laser cutting of the current collector materials. These results show that the copper may have both interaction time and laser intensity dependent processes, and the aluminum may have only a laser intensity dependent process. This part of the study has been published in Journal of Power Sources [36]. In addition, L/V interface geometry, melt pool flow, and temperature distribution are examined with selected laser parameters providing thorough cutting. Laser powers of 250W for copper and 150W for aluminium are chosen with the fixed scanning speed of 3000 mm/s. This analysis obtained very interesting observations such as crests formation for both materials and its possibility of forming a spatter or a recast layer. Furthermore, two consecutive deep penetration holes for the laser cutting of aluminum are observed and these two holes give rise to a neck and stronger flow speed around the neck.

In Chapter V, numerical studies of the laser cutting of electrodes for the lithium-ion battery are investigated. This study considers graphite as an active electrode material for anodes. Due to the sublimation characteristic of graphite, the proposed mathematical model is slightly modified. For cathode, $LiCoO_2$ is considered as an active electrode material. Since most of the material properties of $LiCoO_2$ are unavailable, material properties of $LiCoO_2$ are obtained with the law of fraction. Results are discussed in terms

of interaction time, penetration width, depth, and absorptivity. Furthermore, the geometry of the penetration hole, composition variation, and melt pool flow are analyzed with selected laser parameters. For anode, the L/V interface shows a smooth and clean surface due to the sublimation characteristics of graphite at the beginning of the simulation. When the deep penetration hole reaches the material interface, a melt pool starts to form, develops and results in a two-level surface due mainly to the sublimation property of graphite and the melt pool flow of liquid copper. At the material interface, many interesting results are presented such as higher values of the copper concentration, geometry changes, and strong melt pool flow around deformed graphite region. For cathode, at the beginning of the simulation, the deep penetration hole shows uneven surface and creates crests on the top surface. Moreover, a protrusion is observed. When the deep penetration hole reaches the material interface, the narrower deep penetration hole forms in the aluminum region due to the difference of the boiling temperatures between two materials, and the flow pattern moving toward the center of the deep penetration hole.

In Chapter VI, laser cutting experiments have been presented, comparing the model proposed in Chapter IV and Chapter V. Experimental set-up is described. A 500W IPG CW single mode fiber laser with a focused beam diameter of 11 μm is used as an energy source. To compare the simulation results, the same matrices for both laser power and scanning speed are selected. For copper, laser powers of 200W and 250W for the scanning speed of 1000 mm/s, laser powers of 200W and 250W for the scanning speed of 3000 mm/s, and laser powers of 250W and 300W for the scanning speed of 5000 mm/s are selected. For aluminum, laser power of 100W and 150W for the scanning speed of

1000 mm/s, laser power of 100W and 150W for the scanning speed of 3000 mm/s, and laser power of 150W and 200W for the scanning speed of 5000 mm/s are selected. Kerf widths of current collectors obtained by simulation and experimental results are compared near the threshold of laser cutting. For anode, the laser power of 450W and the scanning speed of 5000 mm/s are chosen. For cathode, the laser power of 150W and the scanning speed of 5000 mm/s are chosen. Image of side and top view of electrodes are taken by SEM and the surface cut quality is evaluated. Composition variation of electrodes along the straight vertical line is measured by EDX analysis. This composition variation obtained by the EDX analysis and simulation is investigated. The measured geometry of laser cutting of current collectors and electrodes match reasonably with the predictions of the numerical model developed in Chapter IV and Chapter V. Finally, the optimum range of laser parameters, which provide both high speed production and good surface cut quality are obtained.

The last Chapter, Chapter VII, summarizes the contributions and limitations of this work, and proposes the future work.

CHAPTER II

MATHEMATICAL MODEL

Laser cutting of electrodes includes interconnected physical phenomena. When laser irradiates on a substrate, the substrate absorbs light energy. This absorbed energy is enough to melt and evaporate materials. In the melted area, called melt pool, solid and liquid materials coexist so that they form a mushy zone. Since this mushy zone consists of solid and liquid phases, thermo-physical material properties are changed based on liquid and solid fraction.

In the evaporation interface, a very thin layer of several mean free paths is observed. This thin layer is called a kinetic Knudsen layer. Across the kinetic Knudsen layer, steep changes of temperature, pressure, and density occur, in which continuum hypothesis fails. Thus, a mathematical discontinuity needs to be considered as a jump condition with back pressure [37]. Furthermore, mass and thermal energy loss on the interface takes into account [38]. In addition to the evaporation, there are more physical phenomena can be observed in a Liquid/Vapor (L/V) interface. Vaporization behaves as a repulsive force on the melt pool, which refer to as recoil pressure. Due to its high pressure, it removes liquid and generates a narrow and deep penetration hole, called also keyhole. This keyhole changes the geometry of the L/V interface and absorbs more

energy by internal multiple reflections [32]. Moreover, surface tension exists due to this geometry changes. The recoil pressure forms upward melt pool flow and it tries to open the keyhole. On the other hands, the surface tension drives the melt pool flow down along the keyhole so that it tries to close the keyhole. Therefore, the L/V interface fluctuates[39]. When equilibrium of the surface forces is broken, the keyhole collapses and a void can be formed [40].

A material interface of the two sandwiched material plays a significant role to the behavior of the laser cutting of electrodes. First, liquid and solid mass fractions for each material need to be carefully considered. Second, an absorption coefficient varies depending on the material composition. Third, an existence of active electrode materials on a top surface of electrodes could disturb the melt pool flow of current collectors. Fourth, the geometry of melt pool can be affected significantly due to different material properties between active electrode materials and current collectors.

2.1. Assumptions

- Three dimensions are considered.

- Laser beam is moving in *x*-direction.

- Symmetric computational domain is used.

- The grids for multiple reflection calculations are much finer than the main grid for the sake of a good resolution of solutions.

- Material properties between vapor and liquid are smoothed out for numerical purposes on the L/V interface, since the differences in material properties between gas and liquid are so tremendous.

- Material properties for high temperature range are extrapolated.

- Unavailable part of phase diagram is extrapolated.

- Liquid and gas flows are assumed Newtonian and incompressible.

- Re-condensation phenomenon is neglected.

- Depth of focus is not considered.

- The constituents are assumed to be separable phase components.

- Chemical reactions between an active electrode material and current collector are not considered.

- Plasma is not taken into consideration.

These simplifications can cause error. Assuming gas flow as a Newtonian and incompressible may cause upto maximum 9% of error since the 9% of the computational domain is gas. Since laser power distribution is continuous phenomena, having a computational grid to express this laser beam may cause error. However, as setting a finer grid compared to a main grid, error caused by discretizing the laser beam distribution can be minimized. Ignoring the plasma-laser interaction may cause error. However, this error is insignificant, since the plasma signal measured experimentally by spectroscopy is very weak. Extrapolation of material properties is inevitable to maintain computational stability during the simulation.

2.2. Governing equations with the Solid-Liquid (S/L) interface boundary conditions in binary Solid-Liquid phase change system

Electrodes are a sandwiched composite material. The anode material consists of copper as a current collector and graphite as an active electrode material, and the cathode material consists of aluminum as a current collector and $LiCoO_2$ as an active electrode material. Once the depth of a deep penetration hole reaches an interface of the active electrode material and current collector, the liquid and solid phases of $LiCoO_2$ and aluminum exist together for the cathode. Due to the sublimation characteristic of graphite, the liquid phase of copper and both the solid phases of copper and graphite exist together for the anode. When this mushy zone is formed, composition varies at the interface. Thus, thermophysical properties of solid and liquid mixture of two materials need to be carefully considered based on the composition changes and mass fractions of two materials. Using the level set method to implement the mushy zone would be inappropriate for the S/L interface problem due to the nonlinearity of the phase change, the morphologically complex, and no exhibition of a sharp interface between the solid and liquid. Therefore, to incorporate the mushy zone, this study adopted a method developed by Bennon and Incropera [41], which is an extension of the classical mixture theory. In this model, a consistent set of continuum equations for the conservation of mass, momentum, energy and species in a binary, solid-liquid phase change system is developed. They assumed laminar and constant property flow in the liquid phase as well as characterized the mushy region as a porous solid of isotropic permeability K.

Principles of development of conservation equations are as follows. First, mixture components may be viewed as isolated subsystems if interactions with other mixture

components are properly treated. Second, all properties of the mixture are mathematical consequences of the component properties. Finally, the mean collective mixture behavior is governed by equations similar to those governing the individual components. Since the constituents of electrodes are assumed to be a separable phase components, simple summation rules can be used. Defining mass fraction f and volume fraction g with phases and materials, the velocity ($\mathbf{u}$), density (ρ), thermal conductivity (k), mass diffusion coefficient (D), concentration (c), and enthalpy (h) for the liquid and solid mixtures of two materials are

$$\mathbf{u} = f_{CC_s}\mathbf{u}_{CC_s} + f_{CC_l}\mathbf{u}_{CC_l} + f_{AE_s}\mathbf{u}_{AE_s} + f_{AE_l}\mathbf{u}_{AE_l} \tag{2.1}$$

$$\rho = g_{CC_s}\rho_{CC_s} + g_{CC_l}\rho_{CC_l} + g_{AE_s}\rho_{AE_s} + g_{AE_l}\rho_{AE_l} \tag{2.2}$$

$$k = \left(\frac{g_{CC_s}}{k_{CC_s}} + \frac{g_{CC_l}}{k_{CC_l}} + \frac{g_{AE_s}}{k_{AE_s}} + \frac{g_{AE_l}}{k_{AE_l}} \right)^{-1} \tag{2.3}$$

$$D = f_{CC_l}D_{CC_l} + f_{AE_l}D_{AE_l} \tag{2.4}$$

$$c = f_{CC_l}c_{CC_l} + f_{CC_s}c_{CC_s} \tag{2.5}$$

$$h = f_{CC_s}h_{CC_s} + f_{CC_l}h_{CC_l} + f_{AE_s}h_{AE_s} + f_{AE_l}h_{AE_l} \tag{2.6}$$

respectively. Subscripts CC and AE denote the current collector and active electrode material, respectively. The liquid phases and solid phases are connected in a serial manner since heat flows in the normal direction to the S/L interface in general [42]. The relationship between the volume and mass fractions are

$$f_{CC_s} = \frac{\rho_{CC_s}g_{CC_s}}{\rho} \tag{2.7}$$

$$f_{CC_l} = \frac{\rho_{CC_l}g_{CC_l}}{\rho} \tag{2.8}$$

$$f_{AE_s} = \frac{\rho_{AE_s} g_{AE_s}}{\rho} \tag{2.9}$$

$$f_{AE_l} = \frac{\rho_{AE_l} g_{AE_l}}{\rho} \tag{2.10}$$

The mass and volume fractions must add to unity as follows

$$f_{CC_s} + f_{CC_l} + f_{AE_s} + f_{AE_l} = 1 \tag{2.11}$$

$$g_{CC_s} + g_{CC_l} + g_{AE_s} + g_{AE_l} = 1 \tag{2.12}$$

and solid and liquid mass fractions are

$$f_s = f_{CC_s} + f_{AE_s} \tag{2.13}$$

$$f_l = f_{CC_l} + f_{AE_l} \tag{2.14}$$

With the defined mixture variables, continuity equation, momentum equations in x-,y-,z-directions, energy equation and solute conservation equation are written as [41]

$$\frac{\partial \rho}{\partial t} + \nabla \cdot (\rho \mathbf{u}) = 0 \tag{2.15}$$

$$\frac{\partial (\rho u)}{\partial t} + \nabla \cdot (\rho \mathbf{u} u) = \nabla \cdot \left(\mu_l \frac{\rho}{\rho_l} \nabla u \right) - \frac{\mu_l}{K} \frac{\rho}{\rho_l} u - \frac{\partial p}{\partial x} \tag{2.16}$$

$$\frac{\partial (\rho v)}{\partial t} + \nabla \cdot (\rho \mathbf{u} v) = \nabla \cdot \left(\mu_l \frac{\rho}{\rho_l} \nabla v \right) - \frac{\mu_l}{K} \frac{\rho}{\rho_l} v - \frac{\partial p}{\partial y} \tag{2.17}$$

$$\frac{\partial (\rho w)}{\partial t} + \nabla \cdot (\rho \mathbf{u} w) = \nabla \cdot \left(\mu_l \frac{\rho}{\rho_l} \nabla w \right) - \frac{\mu_l}{K} \frac{\rho}{\rho_l} w - \frac{\partial p}{\partial z} \tag{2.18}$$

$$\frac{\partial (\rho h)}{\partial t} + \nabla \cdot (\rho \mathbf{u} h) = \nabla \cdot (k \nabla T) - \nabla \cdot [\rho (h_l - h) \mathbf{u}] \tag{2.19}$$

$$\frac{\partial (\rho c)}{\partial t} + \nabla \cdot (\mathbf{u} \rho c) = \nabla \cdot (\rho D \nabla c) + \nabla \cdot [\rho D \nabla (c_l - c)] - \nabla \cdot [\rho f_s (c_l - c_s) \mathbf{u}] \tag{2.20}$$

where the second terms on the right hand side of Eqns. (2.16)-(2.18) is the Darcian damping force to treat the mushy region as a fine permeable solid matrix. K is the isotropic permeability and assumed to vary with liquid volume fraction according to the Kozeny-Carman equations [43]:

$$K = K_0 \frac{g_l^3}{(1-g_l)^2} \tag{2.21}$$

The second term on the right hand side of Eqn. (2.19) is the expression of the mushy zone. The first and second terms on the right hand side of Eqn. (2.19) is the net Fourier diffusion flux and the energy flux associated with relative phase motion. Expressing Eqn. (2.19) in the temperature form would be better for implementation purposes. This could be achieved by linearizing the phase enthalpies. The phase enthalpies are obtained as

$$h_{CCs} = \int_0^T C_{CC\_ps} dT \tag{2.22}$$

$$h_{AEs} = \int_0^T C_{AE\_ps} dT \tag{2.23}$$

$$h_{CC_l} = \int_0^{T_{CC_m}} C_{CC\_ps} dT + L_{CC_m} + \int_{T_{CC_m}}^T C_{CC\_pl} dT \tag{2.24}$$

$$h_{AE_l} = \int_0^{T_{AE_m}} C_{AE\_ps} dT + L_{AE_m} + \int_{T_{AE_m}}^T C_{AE\_pl} dT \tag{2.25}$$

$$h_s = f_{CCs} \int_0^T C_{CC\_ps} dT + f_{AEs} \int_0^T C_{AE\_ps} dT \tag{2.26}$$

$$h_l = f_{CCs} \left(\int_0^{T_{CC_m}} C_{CC\_ps} dT + L_{CC_m} + \int_{T_{CC_m}}^{T} C_{CC\_pl} dT \right) + f_{AEs} \left(\int_0^{T_{AE_m}} C_{AE\_ps} dT + L_{AE_m} + \int_{T_{AE_m}}^{T} C_{AE\_pl} dT \right)$$

(2.27)

where T_{CC_m} and T_{AE_m} are the melting temperature of a current collector and an active electrode material, respectively. L_{CC_m} and L_{AE_m} are the latent heat of fusion of a current collector and an active electrode material, respectively. C_{CC_pl} is the constant-pressure specific heat of the liquid phase of a current collector, C_{CC_ps} is the constant-pressure specific heat of the solid phase of a current collector, C_{AE_pl} is the constant-pressure specific heat of the liquid phase of an active electrode material, and C_{AE_ps} is the constant-pressure specific heat of the solid phase of an active electrode material. Furthermore, the average specific heats of solid and liquid ($\bar{C}_{ps}$ and $\bar{C}_{pl}$) are defined as

$$\bar{C}_{ps} = f_{CC_s} \bar{C}_{CC\_ps} + f_{AE_s} \bar{C}_{AE\_ps}$$

(2.28)

$$\bar{C}_{pl} = f_{CC_l} \bar{C}_{CC\_pl} + f_{AE_l} \bar{C}_{AE\_pl}$$

(2.29)

and the average specific heats of solid and liquid for current collector and active electrode materials are defined as

$$\bar{C}_{CC\_ps} = \frac{1}{T} \int_0^T C_{CC\_ps} dT$$

(2.30)

$$\bar{C}_{AE\_ps} = \frac{1}{T} \int_0^T C_{AE\_ps} dT$$

(2.31)

$$\bar{C}_{CC\_pl} = \frac{1}{T - T_{CC_m}} \int_{T_{CC_m}}^T C_{CC\_ps} dT$$

(2.32)

26

$$\bar{C}_{AE\_pl} = \frac{1}{T - T_{AE_m}} \int_{T_{AE_m}}^{T} C_{AE\_ps} dT \tag{2.33}$$

we obtain:

$$h_s = f_{CC_s} h_{CC_s} + f_{AE_s} h_{AE_s} = f_{CC_s} \bar{C}_{CC\_ps} T + f_{AE_s} \bar{C}_{AE\_ps} T = \bar{C}_{ps} T \tag{2.34}$$

$$h_l = f_{CC_l} h_{CC_l} + f_{AE_l} h_{AE_l}$$
$$= f_{CC_l} \left\{ \bar{C}_{CC\_ps} T_{CC_m} + L_{CC_m} + \bar{C}_{CC\_pl}(T - T_{CC_m}) \right\} + f_{AE_l} \left\{ \bar{C}_{AE\_ps} T_{AE_m} + L_{AE_m} + \bar{C}_{AE\_pl}(T - T_{AE_m}) \right\}$$
$$= \bar{C}_{pl} T + L$$

(2.35)

where $\quad L = f_{CC_l} \left\{ (\bar{C}_{CC\_ps} - \bar{C}_{CC\_pl}) T_{CC_m} + L_{CC_m} \right\} + f_{AE_l} \left\{ (\bar{C}_{AE\_ps} - \bar{C}_{AE\_pl}) T_{AE_m} + L_{AE_m} \right\}$ and

$\bar{C}_{pl} = f_{CC_l} \bar{C}_{CC\_pl} + f_{AE_l} \bar{C}_{AE\_pl}$. By using the defined mixture variables, the boundary

conditions for the S/L interface can be calculated as substituting Eqs. (2.34)-(2.35) into

Eqn. (2.6).

$$h = \bar{C}_{ps} T + \bar{C}_{pl} T + L = \bar{C}_p T + L \tag{2.36}$$

where $\bar{C}_p$ is the average mixture specific heat, defined as

$$\bar{C}_p = \bar{C}_{ps} + \bar{C}_{pl} \tag{2.37}$$

Substituting Eqs. (2.35) and (2.36) into the energy equation (Eqn. (2.19)) results in

$$\frac{\partial (\rho \bar{C}_p T)}{\partial t} + \frac{\partial (\rho L)}{\partial t} + \nabla \cdot (\rho \mathbf{u} \bar{C}_p T) + \nabla \cdot (\rho \mathbf{u} L) = \nabla \cdot (k \nabla T) - \nabla \cdot [\rho (\bar{C}_{pl} T + L - \bar{C}_p T - L) \mathbf{u}]$$
(2.38)

Substituting $\bar{C}_p$ by Eqn. (2.37), expanding the equation, and rearranging the result, we

attain

$$\frac{\partial\left(\rho\bar{C}_{pl}T\right)}{\partial t}+\nabla\cdot\left(\rho\mathbf{u}\bar{C}_{pl}T\right)=\nabla\cdot\left(k\nabla T\right)-\frac{\partial\left(\rho L\right)}{\partial t}-\frac{\partial\left(\rho\bar{C}_{ps}T\right)}{\partial t}-\nabla\cdot\left(\rho\mathbf{u}\bar{C}_{ps}T\right)+\nabla\cdot\left(\rho\bar{C}_{ps}T\right)\mathbf{u}$$
(2.39)

This equation can be simplified by

$$\frac{\partial\left(\rho\bar{C}_{pl}T\right)}{\partial t}+\mathbf{u}\cdot\nabla\left(\rho\bar{C}_{pl}T\right)=\nabla\cdot\left(k\nabla T\right)-\frac{\partial\left(\rho L\right)}{\partial t}-\frac{\partial\left(\rho\bar{C}_{ps}T\right)}{\partial t} \qquad (2.40)$$

At this point, the mass fractions have to be obtained and updated for each numerical iteration. Phase diagram can provide these values. The phase diagram of copper and graphite is shown in Figure 2.1. Due to very low solubility of graphite in copper [44, 45], the currently available phase diagram provides limited information. Therefore, the rest of the phase diagram is extended with continuous curve to the sublimation temperature of pure graphite for numerical purposes. The phase diagram of LiCoO$_2$ and aluminum is not available. So, the phase diagram of cobalt and aluminum is taken in this study, since weight percentage of cobalt is over 60% of LiCoO$_2$. This phase diagram is shown in Figure 2.2.
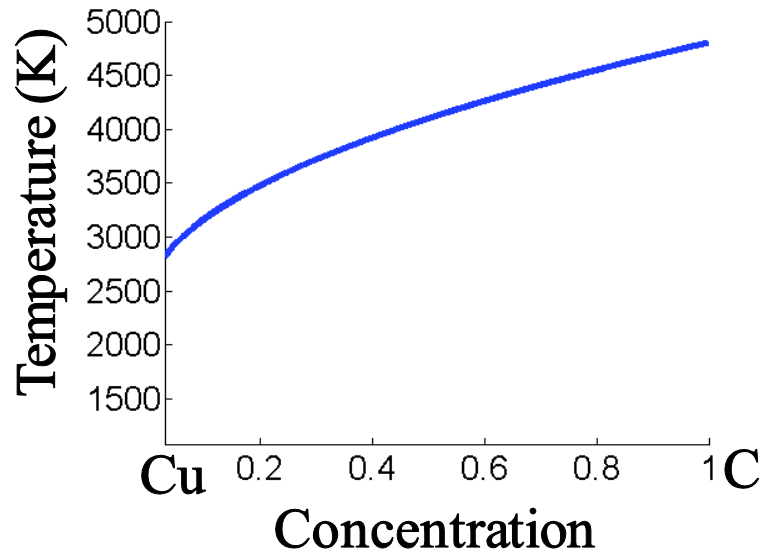
Figure 2.1. Extended phase diagram of graphite and copper

28
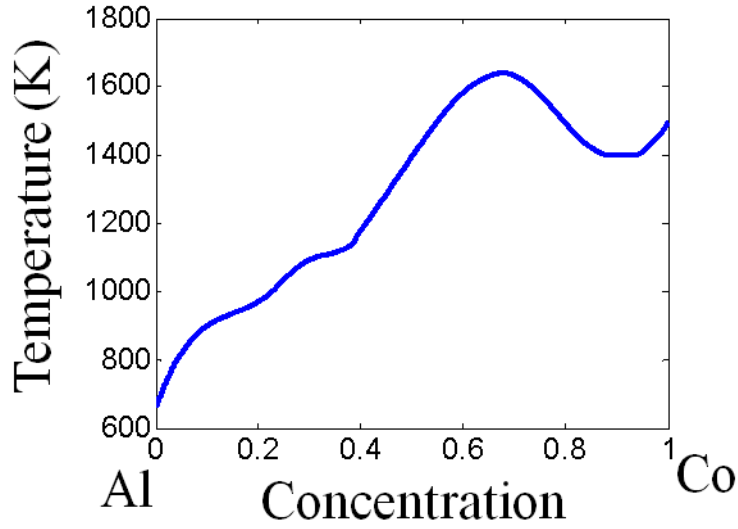
Figure 2.2. Phase diagram of cobalt and aluminum

The first two terms on the right hand side of Eqn. (2.20) account for the net diffusive species flux. The last term represents the species flux due to relative phase motion. During the cutting process, the liquid current collector is diffused into the S/L interface from the melting front of the current collector. A boundary condition for the S/L interface of the composition equation can be written as

$$c_0 \delta(\psi) = 1 \tag{2.41}$$

where c_0 is initial composition of a current collector and ψ indicates the melting front. Considering the boundary condition during the computation on the S/L interface, the concentration of a current collector into an active electrode material can be fully included in this mathematical model.

2.3. Governing equations with boundary conditions of the L/V interface

In this section, boundary conditions of the L/V interface for the continuity, momentum, and energy equations are incorporated in the governing equation.

2.3.1. Continuity equation

Since materials lose their mass due to vaporization, vaporization processes are treated as a volume source term in the continuity equation for the mass conservation. The value of mass loss by evaporation can be obtained by the Eqn.(2.59). Therefore, the continuity equation is written as

$$\frac{\partial \rho}{\partial t} + \nabla \cdot (\rho \mathbf{u}) = \dot{m}_{evap} \delta(\phi) \tag{2.42}$$

where $\delta(\phi)$ is the dirac delta function of the level set values and is defined as

$$\delta(\phi) = \begin{cases} 1 & if\ \phi = 0, \\ 0 & elsewhere \end{cases}$$

and ϕ is the value of level set function which will be discussed later in this chapter.

2.3.2. Momentum equation

Surface tension on the L/V interface plays a significant role to form a deep penetration hole with recoil pressure since surface tension and recoil pressure counteracts each other to maintain the deep penetration hole [39]. Recoil pressure will be implemented into the calculation as a jump condition, which will be mentioned later in this chapter. In this section, a method to implement capillary and thermo-capillary forces

into the momentum equation, which is proposed by Sussman *et el.*[46] and Ki [42], is summarized. Although implementing boundary conditions for the moving L/V interface with conventional methods is very difficult, a level set-based method can incorporate the interface boundary condition in the formula due to its ability to provide normal and curvature information, no matter how complicated it is.

Without considering gravity effect, Navier-Stokes equations for liquid and gas phases can be written as follows.

$$\rho_l \frac{D\mathbf{u}_l}{Dt} = \nabla \cdot \mathbf{T}_l \tag{2.43}$$

$$\rho_g \frac{D\mathbf{u}_g}{Dt} = \nabla \cdot \mathbf{T}_g \tag{2.44}$$

where $\mathbf{T}$ is the stress tensor. Newtonian and incompressible assumptions are used for both fluids. Therefore, we have

$$\mathbf{T}_l = -p_l \mathbf{I} + \mu_l \left(\nabla \mathbf{u}_l + \nabla \mathbf{u}_l^T \right) \tag{2.45}$$

$$\mathbf{T}_g = -p_g \mathbf{I} + \mu_g \left(\nabla \mathbf{u}_g + \nabla \mathbf{u}_g^T \right) \tag{2.46}$$

where $\mathbf{I}$ and superscript $\mathbf{T}$ denote the second-order identity tensor and the transpose of a tensor, respectively. Even though the gas flow is highly compressible due to the intense evaporation, it is assumed incompressible for simplicity. By integrating Eqn. (2.43) over Ω_l and Eqn. (2.44) over Ω_g, and adding the results together, we can obtain the momentum equation for Ω_p

$$\int_{\Omega_p} \rho \frac{D\mathbf{u}}{Dt} dV = \int_{\Omega_p} \nabla \cdot \mathbf{T} \, dV - \int_{\Gamma_p} \left(\mathbf{T}_l - \mathbf{T}_v \right) \cdot \mathbf{n} \, dS \tag{2.47}$$

where **n** is an outward normal for the gas phase. Since laser-material processing has the huge temperature gradient, spatial variation is considered for the accurate force balance at the interface [42].
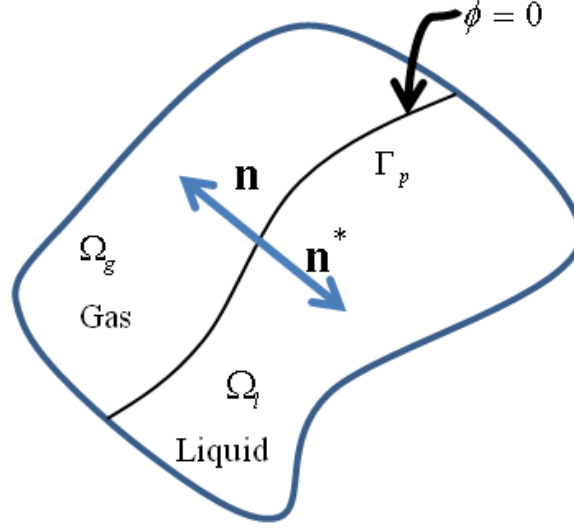
$\partial\Omega_g$: boundary of Ω_g
$\partial\Omega_l$: boundary of Ω_l
Ω_p : $\Omega_l \cap \Omega_g$
$\partial\Omega_p$: boundary of Ω_p
Γ_p : liquid/gas interface

Figure 2.3. Boundary of the L/V interface [42]

Therefore, both capillary and thermo-capillary forces for the L/V interface boundary condition are considered as follows

$$\left(\mathbf{T}_l - \mathbf{T}_g\right)\cdot\mathbf{n} = \sigma\mathbf{n}(\nabla\cdot\mathbf{n}) - \nabla_s\sigma \tag{2.48}$$

where σ and ∇_s are surface tension and surface nabla, respectively. Substituting Eqn. (2.48) into Eqn. (2.47), we obtain

$$\int_{\Omega_p} \rho\frac{D\mathbf{u}}{Dt}dV = \int_{\Omega_p} \nabla\cdot\mathbf{T}\,dV - \int_{\Gamma_p} \left\{\sigma\mathbf{n}(\nabla\cdot\mathbf{n}) - \nabla_s\sigma\right\}dS \tag{2.49}$$

From this point, Smereka [47] claimed as follows

32

$$\int_{\Gamma_p} \left\{ \sigma \mathbf{n}(\nabla \cdot \mathbf{n}) - \nabla_s \sigma \right\} dS = \int_{\Omega_p} \left\{ \sigma \mathbf{n}(\nabla \cdot \mathbf{n}) - \nabla_s \sigma \right\} \delta(\phi) \, dV \tag{2.50}$$

Thus, as applying divergence theorem to the first term on the right hand side of Eqn. (2.49), the Eqn. (2.49) becomes

$$\int_{\Omega_p} \rho \frac{D\mathbf{u}}{Dt} dV = \int_{\Omega_p} \nabla \cdot \mathbf{T} \, dV - \int_{\Omega_p} \left\{ \sigma \mathbf{n}(\nabla \cdot \mathbf{n}) - \nabla_s \sigma \right\} \delta(\phi) \, dV \tag{2.51}$$

and since all the terms are volume integrals, this equation can be written as

$$\int_{\Omega_p} \left[\rho \frac{D\mathbf{u}}{Dt} - \nabla \cdot \mathbf{T} + \left\{ \sigma \mathbf{n}(\nabla \cdot \mathbf{n}) - \nabla_s \sigma \right\} \delta(\phi) \right] dV = 0 \tag{2.52}$$

Since Eqn. (2.52) must be valid for any dV, we finally express the Navier-Stokes equation for both liquid and gas phases,

$$\rho \frac{D\mathbf{u}}{Dt} = \nabla \cdot \mathbf{T} - \left\{ \sigma \mathbf{n}(\nabla \cdot \mathbf{n}) - \nabla_s \sigma \right\} \delta(\phi) \tag{2.53}$$

Since $\mathbf{n}^* = -\mathbf{n}$ the normal obtained from the level set method, and $\nabla \cdot \mathbf{n}^*$ is the curvature, κ, by applying the chain rule, we can obtain

$$\rho \frac{D\mathbf{u}}{Dt} = \nabla \cdot \mathbf{T} - \left\{ \sigma \mathbf{n}^* \kappa - \nabla_s T \frac{d\sigma}{dT} \right\} \delta(\phi) \tag{2.54}$$

The L/V interface boundary conditions in the momentum equation are the two terms inside the bracket on the right hand side. The first term, $\sigma \mathbf{n}^* \kappa$ is the capillary effect acting in the normal direction because of curvature and surface tension. The second term is the thermo-capillary force considering spatial distribution of surface tension due to huge temperature gradient. Surface tension is obtained by the linear summation rule at the material interface of a current collector and an active electrode material.

2.3.3. Energy equation

The boundary conditions at the L/V interface for the energy equation are considered. Laser beam is the heat source during the laser material interaction. While most studies of laser-material interaction modeling have adapted a Gaussian laser beam shape for simplicity [48-50], one often finds several different laser beam shapes, called Transverse Electromagnetic (TEM) modes [51], in a real cavity for the following reasons. First, even in an accurately aligned cavity, some waves travel off-axis as they bounce back and forth, due to the effects of diffraction [52-54]. Second, there is considerable scattering loss that results from scratches on the mirror surface.

The TEM mode patterns are described by a combination of a Gaussian beam profile with a Laguerre polynomial. The modes are denoted TEM$_{pl}$ and can be written as

$$I_{pl}(\rho,\theta) = I_0 \rho^l \left[L_p^l(\rho) \right]^2 \cos^2(l\theta) e^{-\rho} \tag{2.55}$$

where I_0 is the laser intensity, $\rho = \dfrac{2r^2}{w^2}$, $\theta = \tan^{-1}\left(\dfrac{y}{x}\right)$ is the angle between the reference direction on the chosen plane and the line from the origin, and $r = \sqrt{x^2 + y^2}$ is radial distance. w is the beam radius of the mode corresponding to the Gaussian beam radius and L_p^l is the associate Laguerre polynomials of order p and index l, which is expressed as

$$L_p^l(\rho) = \frac{\rho^{-l} e^{\rho}}{p!} \frac{d^p}{d\rho^p} \left(e^{-\rho} \rho^{p+l} \right)$$

So, laser power can be obtained as integrating given TEM$_{pl}$ equation as

$$P_{laser} = \int_0^{2\pi} \int_0^\infty I_{pl}(\rho,\varphi)\, r\, dr\, d\varphi \tag{2.56}$$

where P_{laser} is the laser power. This laser beam distribution is assumed that the beam profile and radius do not change in z direction. Once the deep penetration hole exists, total energy transfer from the laser beam to a workpiece is significantly increased due to the multiple reflections inside the walls of the hole. Therefore, taking into account multiple internal reflections is important when dealing the boundary conditions for the energy equation. These multiple reflections can be realized by using the ray tracing method. If the laser beam is irradiated on the wall of the deep penetration hole, then the reflected rays can be calculated by the formula

$$\mathbf{r} = \mathbf{i} + 2(-\mathbf{i} \cdot \mathbf{n})\mathbf{n} \tag{2.57}$$

where $\mathbf{r}$ is the reflected ray, $\mathbf{i}$ is the incoming ray, and $\mathbf{n}$ is the surface unit normal. As mentioned earlier, the level-set method provides a surface unit normal vector at each point. In this method, the laser energy is absorbed into the wall at each reflection. When the rays escape the computational domain, the calculation of the multiple reflections is terminated.

In addition to multiple reflections, the variation of absorption coefficients due to composition change affects the amount of energy absorption dramatically. The absorption coefficients of a current collector and an active electrode material on the flat surface are different. Once, the deep penetration hole reaches the interface of a current collector and an active electrode material, the composition of the L/V interface changes. Moreover, incident angle is taken into account in determining the absorption coefficient, suggested by Fabbro and Chouf [55]. Therefore, the absorption coefficient on the L/V interface is obtained as a summation of the two absorption coefficient with considering mass fractions and incident angle. It is presented as following

$$A(\alpha) = \left(f_{CC} A_{CC_0} + f_{AE} A_{AE_0} \right) (\cos \alpha) \tag{2.58}$$

where f_{CC} and f_{AE} are mass fraction of a current collector and an active electrode material, respectively, and A_{CC_0} and A_{AE_0} are absorption coefficients on the flat surface of a current collector and an active electrode material, respectively. Again, the incident angle can be calculated based on the information from the level-set method.

There are two different energy loss mechanisms considered in the laser-material interaction. One is the latent heat loss due to evaporation, and the other is the radiation loss due to the high surface temperature. Evaporation occurs on the L/V interface when temperature reaches the boiling point. Just outside L/V interface a very thin layer of several mean free paths, called kinetic Kundsen layer, forms and continuum hypothesis fails across this layer. Hence, steep change in temperature, pressure, and density occurs and this is dealt as a mathematical discontinuity at the interface. Jump conditions with back pressure is used to take into account discontinuity at the interface caused by the Knudsen layer [37]. The net mass flux and energy flux [31, 37, 38] can be expressed as

$$\dot{m}''_{evap} = \rho_s \sqrt{\frac{RT_s}{2\pi}} - \rho_v \sqrt{\frac{RT_v}{2\pi}} \beta F_-(m) = \rho_l F_{evap} \tag{2.59}$$

$$\dot{q}''_{evap} = \rho_l L_v F_{evap} \tag{2.60}$$

where

$$m = \frac{u_v}{\sqrt{2R_v T_v}}$$

$$F_- = \sqrt{\pi} m [-1 + erf(m)] + \exp(-m^2)$$

$$G_- = (2m^2 + 1)[1 - erf(m)] - \frac{2}{\sqrt{\pi}} m \exp(-m^2)$$

$$\beta = \frac{2(2m^2 + 1)\sqrt{T_v/T_s} - 2\sqrt{\pi} m}{F_- + \sqrt{T_v/T_s} G_-}$$

Therefore, the actual laser energy on the L/V interface is:

$$q'' = q''_{L/V} - q''_{evap} - \sigma\varepsilon(T^4 - T_\infty^4) \tag{2.61}$$

where $q''_{L/V}$ is the spatial laser beam distribution in three-dimensional space after multiple internal reflections, and $\sigma\varepsilon(T^4 - T_\infty^4)$ is the energy loss due to radiation. L_v is the latent heat of vaporization and $\rho_l F_e$ is the mass loss due to evaporation. σ and ε are the Stefan-Bolzmann constant and emissivity, respectively. Convection heat loss is not considered since the vapor and liquid phases are solved [35]. Finally, the energy equation for both liquid and gas phases including the L/V interface boundary conditions is

$$\frac{\partial(\rho C_p T)}{\partial t} + \mathbf{u} \cdot \nabla(\rho C_p T) = \nabla \cdot (k\nabla T) + q''\delta(\phi) \tag{2.62}$$

2.4. Free surface evolution: level set

A key factor in the investigation of the interface shape and the process physics is tracking free surface. Osher and Sethian [56] developed the level set method. This method has increasingly been used for many complex problems due to its easy implementation, straightforward concept, ability to handle surface merging and separation automatically, and easy achievements of geometric qualities, such as the surface normal and the curvature on the surface.

To implement the level set method, the surface of interest, which is the L/V interface, is set as the zero iso-surface or zero level set. However, the equations are valid for both a zero level set, as well as all other level sets [57].

$$\phi\left(\mathbf{x},t\right)=\pm d \tag{2.63}$$

To derive PDE, d in Eqn.(2.63) is set to zero and the material derivative is taken as

$$\frac{D\phi}{Dt}=\frac{\partial\phi}{\partial t}+\mathbf{u}\cdot\nabla\phi=0 \tag{2.64}$$

This equation can be re-written as

$$\frac{\partial\phi}{\partial t}+\mathbf{u}\cdot\mathbf{n}\,|\nabla\phi|=0 \tag{2.65}$$

Since surface normal vectors can be obtained from the level set function as

$$\mathbf{n}=\frac{\nabla\phi}{|\nabla\phi|} \tag{2.66}$$

Here, $\mathbf{u}\cdot n$ is the speed of the interface in the normal direction and F is referred to as the speed function or force function. Thus, the final form of the level set function is a hyperbolic PDE.

$$\frac{\partial\phi}{\partial t}+F\,|\nabla\phi|=0 \tag{2.67}$$

The speed function, or F, is composed of numerical expression of fluid flow and evaporation. The L/V interface in the level set equation, i.e. $\phi=0$, is evolved by the speed function. The fluid flow can be obtained by solving momentum equations proposed in Eqs.(2.16)-(2.18). Evaporation mass flux into the level set equation is obtained from Eqn. (2.59). Hence, a final form of the speed function is

$$F=F_{evap}+\mathbf{u}\cdot\mathbf{n} \tag{2.68}$$

where $\mathbf{u}$ is the melt pool speed and $\mathbf{n}$ is the normal vector. The vaporizing mass flux, F_{evap}, is assumed perpendicular to the L/V interface.

2.5. Generalized transport equation

Combining the abovementioned boundary conditions, governing equation can be written as below.

$$\frac{\partial \rho}{\partial t} + \nabla \cdot (\rho \mathbf{u}) = \dot{m}_{evap} \delta(\phi) \tag{2.69}$$

$$\frac{\partial (\rho u)}{\partial t} + \nabla \cdot (\rho \mathbf{u} u) = \nabla \cdot \left(\mu_l \frac{\rho}{\rho_l} \nabla u \right) - \frac{\mu_l}{K} \frac{\rho}{\rho_l} u - \frac{\partial p}{\partial x} - \mathbf{e_x} \cdot (\sigma \mathbf{n}^* \kappa - \Delta_s T \frac{d\sigma}{dT}) \delta(\phi) \tag{2.70}$$

$$\frac{\partial (\rho v)}{\partial t} + \nabla \cdot (\rho \mathbf{u} v) = \nabla \cdot \left(\mu_l \frac{\rho}{\rho_l} \nabla v \right) - \frac{\mu_l}{K} \frac{\rho}{\rho_l} v - \frac{\partial p}{\partial y} - \mathbf{e_y} \cdot (\sigma \mathbf{n}^* \kappa - \Delta_s T \frac{d\sigma}{dT}) \delta(\phi) \tag{2.71}$$

$$\frac{\partial (\rho w)}{\partial t} + \nabla \cdot (\rho \mathbf{u} w) = \nabla \cdot \left(\mu_l \frac{\rho}{\rho_l} \nabla w \right) - \frac{\mu_l}{K} \frac{\rho}{\rho_l} w - \frac{\partial p}{\partial z} - \mathbf{e_z} \cdot (\sigma \mathbf{n}^* \kappa - \Delta_s T \frac{d\sigma}{dT}) \delta(\phi) \tag{2.72}$$

$$\frac{\partial (\rho \bar{C}_{pl} T)}{\partial t} + \mathbf{u} \cdot \nabla (\rho \bar{C}_{pl} T) = \nabla \cdot (k \nabla T) - \frac{\partial (\rho L)}{\partial t} - \frac{\partial (\rho \bar{C}_{pl} T)}{\partial t} + \left(q_{L/V}^{''} - \rho_l L_v F_e - \sigma \varepsilon (T^4 - T_\infty^4) \right) \delta(\phi)$$
(2.73)

$$\frac{\partial (\rho c)}{\partial t} + \nabla \square (\mathbf{u} \rho c) = \nabla \cdot (\rho D \nabla c) + \nabla \cdot [\rho D \nabla (c_l - c)] - \nabla \cdot [\rho (c_l - c) \mathbf{u}] \tag{2.74}$$

In this generalized transport equation, S/L and L/V boundary conditions are fully considered. The second terms on the right hand side of the momentum equations are the Darcian damping force to treat the mushy region as a fine permeable solid matrix. This mushyzone is incorporated to treat the mixture of solid and liquid current collectors as well as solid and liquid active electrode materials. K is the isotropic permeability and assumed to vary with liquid volume fraction according to the Kozeny-Carman equation as described in Eqn. (2.21). The first term on the right hand side of the energy equation is the net Fourier diffusion flux and the second and third terms on the right hand side of the

39

equation are the energy flux associated with relative phase motion expressed in terms of the temperature form. Furthermore, mass transfer of the mushy zone is also considered in the species equation. The first two terms on the right hand side of the species equations are the net diffusive species flux and the last term represents the species flux due to relative phase motion. In addition, evaporation, surface forces, and energy absorption and losses are included using the dirac delta function and level set function in each equation as the L/V boundary conditions. The first term on the right hand of the continuity is mass loss due to the evaporation. The last terms on the right side of the momentum equations are the surface forces, capillary and thermo-capillary forces caused by the geometry variation and high temperature gradient. On the energy equation, the last three terms in the parenthesis on the right hand side are the laser energy absorbed by the multiple reflections, energy loss by evaporation, and energy loss by radiation.

2.6. Modifications for each chapter

When this model is used to investigate the effects of the laser beam modes on laser-material interface and applied to the laser cutting of current collectors, single materials have to be used. The materials used for the Chapter III and Chapter IV are mild steel and current collectors, such as pure copper and aluminum, respectively. In addition, graphite, which has sublimation characteristic, is used as an active electrode material of the anode in Chapter V. Therefore, proper modifications must be made.

For single materials, mass fraction and mixture properties need to be modified. Since this is single materials, mixture properties, the volume fraction, and mass fractions from Eqn. (2.1) - (2.12) become simple. The solid mass fraction can be defined as

$$f_s = 1 - f_l \tag{2.75}$$

and these mass fractions for steel can be updated according to a scheme develop by Prakash and Voller [58]. For pure copper and aluminum, this model assigns the mass liquid fraction 1 and 0 when the temperature is above and below melting temperature, respectively. Similarly to the defined mass fraction, the volume fraction could be defined for liquid and solid (g_l and g_s) as the fractions of volume in one computational cell. The relationship between the mass fraction (f_l) and the volume fraction (f_s) can be described as

$$f_s = \frac{\rho_s g_s}{\rho} \tag{2.76}$$

$$f_l = \frac{\rho_l g_l}{\rho} \tag{2.77}$$

$$g_s + g_l = 1 \tag{2.78}$$

With these relations, the velocity (u), density (ρ), thermal conductivity (k), mass diffusion coefficient (D), and enthalpy (h) for the liquid and solid mixture are defined as

$$\mathbf{u} = f_s \mathbf{u}_s + f_l \mathbf{u}_l \tag{2.79}$$

$$\rho = g_s \rho_s + g_l \rho_l \tag{2.80}$$

$$k = \left(\frac{g_s}{k_s} + \frac{g_l}{k_l} \right)^{-1} \tag{2.81}$$

$$D = f_l D_l \tag{2.82}$$

$$h = f_s h_s + f_l h_l \tag{2.83}$$

The phase enthalpies are obtained as

$$h_s = \int_0^T C_{ps} dT \tag{2.84}$$

$$h_l = \int_0^{T_e} C_{ps} dT + L_m + \int_{T_e}^T C_{pl} dT \tag{2.85}$$

where T_e is the eutectic temperature, L_m is latent heat of fusion, C_{pl} is the constant-pressure specific heat of liquid, C_{ps} is the constant-pressure specific heat of the solid. Furthermore, the average specific heats ($\bar{C}_{pl}$ and $\bar{C}_{pl}$) are defined as

$$\bar{C}_{ps} = \frac{1}{T} \int_0^T C_{ps} dT \tag{2.86}$$

$$\bar{C}_{pl} = \frac{1}{T - T_e} \int_{T_e}^T C_{pl} dT \tag{2.87}$$

By using the defined mixture variables,

$$h_s = \bar{C}_{ps} T \tag{2.88}$$

$$h_l = \bar{C}_{pl} T + L \tag{2.89}$$

$$h = \bar{C}_p T + f_l L \tag{2.90}$$

where $L = (\bar{C}_{ps} - \bar{C}_{pl})T_e + L_m$. As substituting Eqns. (2.89) - (2.90) in Eqn. (2.19). The final form of the energy equation can be written as

$$\frac{\partial\left(\rho\bar{C}_{pl}T\right)}{\partial t} + \mathbf{u}\cdot\nabla\left(\rho\bar{C}_{pl}T\right) = \nabla\cdot\left(k\nabla T\right) - \frac{\partial(\rho f_l L)}{\partial t} + \frac{\partial(\rho f_s \bar{C}_p T)}{\partial t} + \left(q_{L/V}^{"} - \rho LF - \sigma\varepsilon(T^4 - T_\infty^4)\right)\delta(\phi)$$
(2.91)

The detail derivation of the Eqn. (2.91) can be described in [33].

There is no liquid phase on the graphite laser cutting. To keep demonstrate the important physical phenomena included in the three-dimensional self-consistent laser-material interaction model, modifications are carefully made for the graphite region. First, since there is no liquid phase, no mushy zone is considered. Second, a liquid viscosity is assumed to be a large number compared to the gas phase because Eqns. (2.70) - (2.74) are modeled to solve the both liquid and gas phases. Third, liquid properties are set to be the same as solid properties. Fourth, no surface tension is considered. Furthermore, with given assumptions, Eqns. in section 2.2 can be modified as follows

$$\mathbf{u} = f_{Cu_s}\mathbf{u}_{Cu_s} + f_{Cu_l}\mathbf{u}_{Cu_l} + f_{C_s}\mathbf{u}_{C_s}$$
(2.92)

$$\rho = g_{Cu_s}\rho_{Cu_s} + g_{Cu_l}\rho_{Cu_l} + g_{C_s}\rho_{C_s}$$
(2.93)

$$k = \left(\frac{g_{Cu_s}}{k_{Cu_s}} + \frac{g_{Cu_l}}{k_{Cu_l}} + \frac{g_{C_s}}{k_{C_s}}\right)^{-1}$$
(2.94)

$$D = f_{Cu_l}D$$
(2.95)

$$c = f_{Cu_l}c_{Cu_l} + f_{Cu_s}c_{Cu_s}$$
(2.96)

$$h = f_{Cu_s}h_{Cu_s} + f_{Cu_l}h_{Cu_l} + f_{C_s}h_{C_s}$$
(2.97)

where the subscripts Cu and C denote copper and graphite, respectively. The relationship between the volume and mass fractions are

$$f_{Cu_s} = \frac{\rho_{Cu_s} g_{Cu_s}}{\rho} \tag{2.98}$$

$$f_{Cu_l} = \frac{\rho_{Cu_l} g_{Cu_l}}{\rho} \tag{2.99}$$

$$f_{C_s} = \frac{\rho_{C_s} g_{C_s}}{\rho} \tag{2.100}$$

The mass and volume fractions must add to unity as follows

$$f_{Cu_s} + f_{C_s} + f_{Cu_l} = 1 \tag{2.101}$$

$$g_{Cu_s} + g_{Cu_l} + g_{C_s} = 1 \tag{2.102}$$

and the solid and liquid mass fractions are

$$f_s = f_{Cu_s} + f_{C_s} \tag{2.103}$$

$$f_l = f_{Cu_l} \tag{2.104}$$

These defined mixture variables are considered in the continuity equation, momentum equations in x-, y-, and z- directions, energy equation and species equation. The phase enthalpies are obtained as

$$h_{Cu_s} = \int_0^T C_{ps\_Cu} dT \tag{2.105}$$

$$h_{C_s} = \int_0^T C_{ps\_C} dT \tag{2.106}$$

$$h_{Cu_l} = \int_0^{T_m} C_{ps\_Cu} dT + L_m + \int_{T_m}^T C_{pl\_Cu} dT \tag{2.107}$$

where T_m is the melting temperature of copper, L_m is the latent heat of fusion, C_{Cu_pl} is the constant-pressure specific heat of the liquid phase of copper, C_{Cu_ps} is the constant-pressure specific heat of the solid phase of copper, and C_{C_ps} is the constant-pressure specific heat of the solid phase of graphite. Furthermore, the average specific heats of solid and liquid ($\bar{C}_{ps}$ and $\bar{C}_{pl}$) are defined as

$$\bar{C}_{Cu\_ps} = \frac{1}{T}\int_0^T C_{Cu\_ps}dT \tag{2.108}$$

$$\bar{C}_{Cu\_pl} = \frac{1}{T-T_m}\int_{T_m}^T C_{Cu\_pl}dT \tag{2.109}$$

$$\bar{C}_{C\_ps} = \frac{1}{T}\int_0^T C_{C\_ps}dT \tag{2.110}$$

$$h_{C_s} = \bar{C}_{C\_ps}T \tag{2.111}$$

$$h_{Cu_s} = \bar{C}_{Cu\_ps}T \tag{2.112}$$

$$
\begin{aligned}
h_{Cu_l} &= \bar{C}_{Cu\_ps}T_m + L_m + \bar{C}_{Cu\_pl}(T-T_m) \\
&= \bar{C}_{Cu\_pl}T + \left(\bar{C}_{Cu\_ps}-\bar{C}_{Cu\_pl}\right)T_m + L_m \\
&= \bar{C}_{Cu\_pl}T + L
\end{aligned}
\tag{2.113}
$$

$$
\begin{aligned}
h &= \left(f_{C_s}\bar{C}_{C\_ps} + f_{Cu_s}\bar{C}_{Cu\_ps} + f_{Cu_l}\bar{C}_{Cu\_pl}\right)T + f_{Cu_l}L \\
&= \bar{C}_p T + f_{Cu_l}L
\end{aligned}
\tag{2.114}
$$

where $L = \left(\bar{C}_{Cu\_ps} - \bar{C}_{Cu\_pl}\right)T_m + L_m$ and $\bar{C}_p$ is the average mixture specific heat, defined as

$$\bar{C}_p = f_{C_s}\bar{C}_{C\_ps} + f_{Cu_s}\bar{C}_{Cu\_ps} + f_{Cu_l}\bar{C}_{Cu\_pl} \tag{2.115}$$

and can be written as

$$\bar{C}_p = \bar{C}_{Cu\_pl} - f_s\Delta\bar{C}_p \tag{2.116}$$

$$\Delta \bar{C}_p = \frac{f_{Cu_s}}{f_s}(\bar{C}_{Cu\_pl} - \bar{C}_{Cu\_ps}) + \frac{f_{C_s}}{f_s}(\bar{C}_{Cu\_pl} - \bar{C}_{C\_ps})$$ (2.117)

By using the defined mixture variables, the boundary conditions for the S/L interface can be calculated by substituting Eqs. (2.113) and (2.114) into Eqn. (2.6). Now, eqn (2.91) can be obtained by substituting the above relations.

2.7. Solution scheme

The solution procedure for transportation equation is summarized, closely following [59]. General form in a Cartesian coordinate system in the reference frame can be written as follows

$$\frac{\partial(\rho\Phi)}{\partial t} + \frac{\partial(\rho u\Phi)}{\partial x} + \frac{\partial(\rho v\Phi)}{\partial y} + \frac{\partial(\rho w\Phi)}{\partial z} = \frac{\partial}{\partial x}\left(\Gamma\frac{\partial\Phi}{\partial x}\right) + \frac{\partial}{\partial y}\left(\Gamma\frac{\partial\Phi}{\partial y}\right) + \frac{\partial}{\partial z}\left(\Gamma\frac{\partial\Phi}{\partial z}\right) + S_\Phi(x,y,z,t)$$

(2.118)

where ρ is the density of material, t is time, Φ is the dependent variable, Γ is diffusivity, and $S_\Phi(x,y,z,t)$ is any additional terms, which do not follow the generalized formulation. Then the momentum and energy equations are discretized

$$\frac{a_P}{a_\Phi}\Phi_P = a_E\Phi_E + a_W\Phi_W + a_N\Phi_N + a_S\Phi_S + a_T\Phi_T + a_B\Phi_B + b + (1-a_\Phi)\frac{a_P}{a_\Phi}\Phi_P^*$$ (2.119)

where

$$a_E = D_e + <-F_e,0> \qquad a_W = D_w + <F_w,0>$$
$$a_N = D_n + <-F_n,0> \qquad a_S = D_s + <F_s,0>$$
$$a_T = D_t + <-F_t,0> \qquad a_B = D_b + <F_b,0>$$

$$a_P^0 = \frac{\rho_P^0\Delta x\Delta y\Delta z}{\Delta t}$$

$$b = S_C \Delta x \Delta y \Delta z + a_P^0 \Phi_P^0$$

$$a_P = a_E + a_W + a_N + a_S + a_T + a_B + a_P^0 - S_P \Delta x \Delta y \Delta z$$

$<A, B>$ is defined the greater of A and B. α_Φ is the relaxation factor for the dependent

variable Φ, and Φ_P^* is the value of Φ_P from the previous iteration. To avoid unpredicted

divergence, under-relaxation factors are used for velocity, temperature, and composition

variables. Relaxation factors are 0.7 for velocity, temperature and composition variables.

Flow rate F and conductances D can write

$$F_e = (\rho u)_e \Delta y \Delta z \qquad\qquad D_e = \frac{\Gamma_e \Delta y \Delta z}{(\delta x)_e}$$

$$F_w = (\rho u)_w \Delta y \Delta z \qquad\qquad D_w = \frac{\Gamma_w \Delta y \Delta z}{(\delta x)_w}$$

$$F_n = (\rho v)_n \Delta z \Delta x \qquad\qquad D_n = \frac{\Gamma_n \Delta z \Delta x}{(\delta y)_n}$$

$$F_s = (\rho v)_s \Delta z \Delta x \qquad\qquad D_s = \frac{\Gamma_s \Delta z \Delta x}{(\delta y)_s}$$

$$F_t = (\rho w)_t \Delta x \Delta y \qquad\qquad D_t = \frac{\Gamma_t \Delta x \Delta y}{(\delta z)_t}$$

$$F_b = (\rho w)_b \Delta x \Delta y \qquad\qquad D_b = \frac{\Gamma_b \Delta x \Delta y}{(\delta z)_b}$$

A staggered grid is used to obtain the physically proper pressure field [60]. Scalar and

vector quantities are stored at the nodes of an ordinary control volume and at the center of

the cell faces, respectively. On the staggered grid system, Semi-Implicit Method for

Pressure-Linked Equations Consistent (SIMPLEC) is adopted to solve the coupled

pressure-velocity fields [61]. The discretized momentum equations can be written as

$$a_e u_e = \sum a_{nb} u_{nb} + b + (p_P - p_E) A_e \tag{2.120}$$

$$a_w u_w = \sum a_{nb} u_{nb} + b + (p_W - p_P) A_w \tag{2.121}$$

$$a_n v_n = \sum a_{nb} v_{nb} + b + (p_P - p_N) A_n \tag{2.122}$$

$$a_s v_s = \sum a_{nb} v_{nb} + b + (p_S - p_P) A_s \tag{2.123}$$

$$a_t w_t = \sum a_{nb} w_{nb} + b + (p_P - p_T) A_t \tag{2.124}$$

$$a_b w_b = \sum a_{nb} w_{nb} + b + (p_B - p_P) A_b \tag{2.125}$$

Only when the pressure field is given or is somehow estimated, the momentum equations can be solved. So, guessed values of velocity (u^*, v^*, w^*) will result from the solution of the following discretization equations:

$$a_e u_e^* = \sum a_{nb} u_{nb}^* + b + (p_P^* - p_E^*) A_e \tag{2.126}$$

$$a_w u_w^* = \sum a_{nb} u_{nb} + b + (p_W^* - p_P^*) A_w \tag{2.127}$$

$$a_n v_n^* = \sum a_{nb} v_{nb} + b + (p_P^* - p_N^*) A_n \tag{2.128}$$

$$a_s v_s^* = \sum a_{nb} v_{nb} + b + (p_S^* - p_P^*) A_s \tag{2.129}$$

$$a_t w_t^* = \sum a_{nb} w_{nb} + b + (p_P^* - p_T^*) A_t \tag{2.130}$$

$$a_b w_b^* = \sum a_{nb} w_{nb} + b + (p_B^* - p_P^*) A_b \tag{2.131}$$

If we subtract Eqn.(2.126) from Eqn.(2.120), we have

$$a_e u_e^{'} = \sum a_{nb} u_{nb}^{'} + A_e p_P^{'} - A_e p_E^{'} \tag{2.132}$$

where $u_e^{'} = u_e - u_e^*$, $u_{nb}^{'} = u_{nb} - u_{nb}^*$, $p_P^{'} = p_P - p_P^*$, and $p_E^{'} = p_E - p_E^*$. Rearranging

Eqn.(2.132) without the first term of the Eqn. (2.132) on the right had side provides

$$u_e^{'} = d_e (p_P^{'} - p_E^{'}) \tag{2.133}$$

where $d_e = \dfrac{A_e}{a_e}$. For the SIMPLEC algorithm, $\dfrac{A_e}{a_e - \sum a_{nb}}$ is used for d_e instead of $\dfrac{A_e}{a_e}$.

Eqn. (2.133) is called the velocity-correction formula, which is also can be written as

$$u_e = u_e^* + d_e(p_P' - p_E')$$

(2.134)

The other directions of the velocity-correction formula can be written in the similar manner:

$$u_w = u_w^* + d_w(p_W' - p_P')$$

(2.135)

$$u_n = u_n^* + d_n(p_P' - p_N')$$

(2.136)

$$u_s = u_s^* + d_s(p_S' - p_P')$$

(2.137)

$$u_t = u_t^* + d_t(p_P' - p_T')$$

(2.138)

$$u_b = u_b^* + d_b(p_B' - p_P')$$

(2.139)

Now, continuity equation is discretized by integrating it over a cell for scalar variables and expressed as

$$\frac{(\rho_P - \rho_P^0)\Delta x \Delta y \Delta z}{\Delta t} + \left[(\rho u)_e - (\rho u)_w\right]\Delta y \Delta z + \left[(\rho v)_n - (\rho v)_s\right]\Delta z \Delta x + \left[(\rho w)_t - (\rho w)_b\right]\Delta x \Delta y = 0$$

(2.140)

If we substitute all the velocity-correction formula into Eqn. (2.140), we can obtain the following discretization equation for p':

$$a_P p_P' = a_E p_E' + a_W p_W' + a_N p_N' + a_S p_S' + a_T p_T' + a_B p_B' + b$$

(2.141)

where

$$a_E = \rho_e d_e \Delta y \Delta z \qquad a_W = \rho_w d_w \Delta y \Delta z$$
$$a_N = \rho_n d_n \Delta z \Delta x \qquad a_S = \rho_s d_s \Delta z \Delta x$$
$$a_T = \rho_t d_t \Delta x \Delta y \qquad a_B = \rho_b d_b \Delta x \Delta y$$

$$a_P = a_E + a_W + a_N + a_S + a_T + a_B$$

$$b = \frac{(\rho_P^0 - \rho_P)\Delta x \Delta y \Delta z}{\Delta t} + \left[(\rho u^*)_w - (\rho u^*)_e\right]\Delta y \Delta z + \left[(\rho v^*)_s - (\rho v^*)_n\right]\Delta z \Delta x + \left[(\rho w^*)_b - (\rho w^*)_t\right]\Delta x \Delta y$$

The interface density such as ρ_e obtained linear interpolation of the density values on the main grid points since scalar values are available on the main grid points.

The sequence of operations for SIMPLEC is summarized as follows:

1. Guess the pressure field p^*

2. Solve the momentum equations to obtain u^*, v^*, and w^*

3. Solve the p' equation.

4. Calculate p by adding p' to p^*

5. Calculate velocity from their starred values using the velocity-correction formulas Eqs.(2.134)-(2.139).

6. Solve the discretization equations for temperature and concentration.

7. Treat the corrected pressure p as a new guessed pressure p^*, return to step 2, and repeat the whole procedure until a converged solution is obtained.

The pressure-correction equation is also prone to diverge unless some under-relaxation is used. The L/V interface has significantly different properties to those of the S/L interface. Therefore, the material properties are smoothed out from the liquid to the vapor phase using discrete functions proposed as

$$H_{\varepsilon,c}(\phi) = \begin{cases} 1 & \text{if } \phi \leq 0, \\ c\left(\dfrac{1}{2}\right)^{\frac{\phi}{\min(\Delta z)}} & \text{if } 0 < \phi \leq \varepsilon, \\ 0 & \text{if } \phi > \varepsilon, \end{cases} \tag{2.142}$$

where ε and *c* represent the width of the interface and the degree of continuity, respectively. The *c* ranges from 0 to 1. Thus, the material properties can be expressed by this function. This is shown in Figure 2.4. Viscosity, for example, is defined as

$$\mu_{\varepsilon,c} = \mu_{vap} + (\mu_{liq} - \mu_{vap})H_{\varepsilon,c}(\phi) \tag{2.143}$$
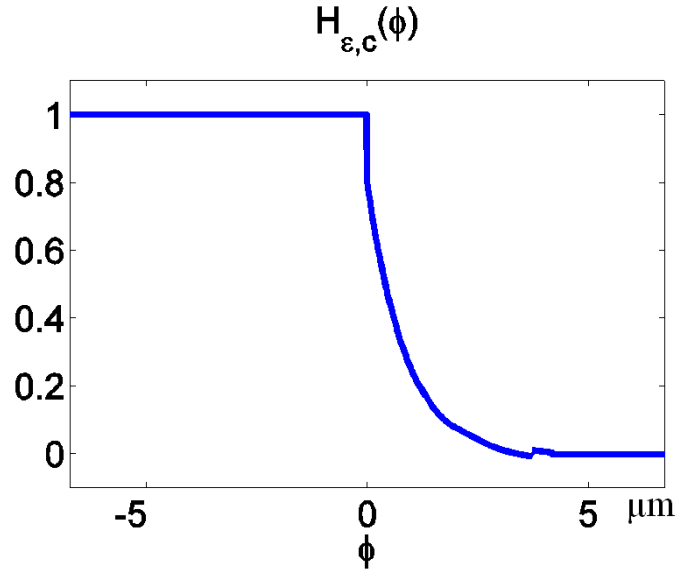
Figure 2.4. Material properties smoothing out

The value of c for all of the material properties is taken as 1 and 7 x min(Δz) is chosen for ε in this study to smooth the material properties. Δz is the length of the smallest grid in the z direction.

The level set function can be discretized as following [62].

$$\phi_{ijk}^{n+1} = \phi_{ijk}^{n} - \Delta t \left[\max(F_{ijk}, 0)\nabla^{+} + \min(F_{ijk}, 0)\nabla^{-} \right] \tag{2.144}$$

where

$$\nabla^{-} = \left[\max(B,0)^{2} + \min(A,0)^{2} + \max(D,0)^{2} + \min(C,0)^{2} + \max(F,0)^{2} + \min(E,0)^{2} \right]^{1/2}$$
$$\nabla^{+} = \left[\max(A,0)^{2} + \min(B,0)^{2} + \max(C,0)^{2} + \min(D,0)^{2} + \max(E,0)^{2} + \min(F,0)^{2} \right]^{1/2}$$

51

Spatial derivative in Eqn. (2.144) can be approximated to second order accuracy with the second-order space convex scheme as follows.

$$A = D_{ijk}^{-x} + \frac{\Delta x}{2} m\left(D_{ijk}^{-x-x}, D_{ijk}^{+x-x}\right) \qquad (2.145)$$

$$B = D_{ijk}^{+x} + \frac{\Delta x}{2} m\left(D_{ijk}^{+x+x}, D_{ijk}^{+x-x}\right)$$

$$C = D_{ijk}^{-y} + \frac{\Delta y}{2} m\left(D_{ijk}^{-y-y}, D_{ijk}^{+y-y}\right)$$

$$D = D_{ijk}^{+y} + \frac{\Delta y}{2} m\left(D_{ijk}^{+y+y}, D_{ijk}^{+y-y}\right)$$

$$E = D_{ijk}^{-z} + \frac{\Delta z}{2} m\left(D_{ijk}^{-z-z}, D_{ijk}^{+z-z}\right)$$

$$F = D_{ijk}^{+z} + \frac{\Delta z}{2} m\left(D_{ijk}^{+z+z}, D_{ijk}^{+z-z}\right)$$

where

$$m(x, y) = \begin{cases} x & \text{if } xy \geq 0 \text{ and } |x| \leq |y| \\ y & \text{if } xy \geq 0 \text{ and } |x| > |y| \\ z & \text{if } xy < 0 \end{cases}$$

A short hand notation,

$$D_i^{+x} = D^{+x}\phi_i^n = \frac{\phi_{i+1,j,k}^n - \phi_{i,j,k}^n}{x_{i+1} - x_i}.$$

Since the level set function is the hyperbolic problem, the CFL condition must be used. Thus, we have

$$\max_{\Omega} F\Delta t \leq \Delta x \qquad (2.146)$$

52

The surface normal and curvature can be calculated from the level set function. Capillary term, thermo-capillary terms as well as multiple internal reflections using the ray tracing technique can be obtained with the normal and curvature values. The surface normal can be discretized with the central difference scheme. The one-sided difference approximations to the unit normal in each possible direction are all obtained and then averaged to deal with the surface geometry, which may undergo a jump at a corner[63].

$$
n_{ijk} = \left[\frac{\phi_x}{\left(\phi_x^2 + \phi_y^2 + \phi_z^2\right)^{1/2}}, \frac{\phi_y}{\left(\phi_x^2 + \phi_y^2 + \phi_z^2\right)^{1/2}}, \frac{\phi_z}{\left(\phi_x^2 + \phi_y^2 + \phi_z^2\right)^{1/2}} \right]
$$

$$
\approx \frac{1}{8} \left[\frac{\left(D_x^+\phi_{ijk}, D_y^+\phi_{ijk}, D_z^+\phi_{ijk}\right)}{\left(\left(D_x^+\phi_{ijk}\right)^2 + \left(D_y^+\phi_{ijk}\right)^2 + \left(D_z^+\phi_{ijk}\right)^2\right)^{1/2}} + \frac{\left(D_x^+\phi_{ijk}, D_y^+\phi_{ijk}, D_z^-\phi_{ijk}\right)}{\left(\left(D_x^+\phi_{ijk}\right)^2 + \left(D_y^+\phi_{ijk}\right)^2 + \left(D_z^-\phi_{ijk}\right)^2\right)^{1/2}} \right.
$$
$$
+ \frac{\left(D_x^+\phi_{ijk}, D_y^-\phi_{ijk}, D_z^+\phi_{ijk}\right)}{\left(\left(D_x^+\phi_{ijk}\right)^2 + \left(D_y^-\phi_{ijk}\right)^2 + \left(D_z^+\phi_{ijk}\right)^2\right)^{1/2}} + \frac{\left(D_x^-\phi_{ijk}, D_y^+\phi_{ijk}, D_z^+\phi_{ijk}\right)}{\left(\left(D_x^-\phi_{ijk}\right)^2 + \left(D_y^+\phi_{ijk}\right)^2 + \left(D_z^+\phi_{ijk}\right)^2\right)^{1/2}}
$$
$$
+ \frac{\left(D_x^+\phi_{ijk}, D_y^-\phi_{ijk}, D_z^-\phi_{ijk}\right)}{\left(\left(D_x^+\phi_{ijk}\right)^2 + \left(D_y^-\phi_{ijk}\right)^2 + \left(D_z^-\phi_{ijk}\right)^2\right)^{1/2}} + \frac{\left(D_x^-\phi_{ijk}, D_y^+\phi_{ijk}, D_z^-\phi_{ijk}\right)}{\left(\left(D_x^-\phi_{ijk}\right)^2 + \left(D_y^+\phi_{ijk}\right)^2 + \left(D_z^-\phi_{ijk}\right)^2\right)^{1/2}}
$$
$$
\left. + \frac{\left(D_x^-\phi_{ijk}, D_y^-\phi_{ijk}, D_z^+\phi_{ijk}\right)}{\left(\left(D_x^-\phi_{ijk}\right)^2 + \left(D_y^-\phi_{ijk}\right)^2 + \left(D_z^+\phi_{ijk}\right)^2\right)^{1/2}} + \frac{\left(D_x^-\phi_{ijk}, D_y^-\phi_{ijk}, D_z^-\phi_{ijk}\right)}{\left(\left(D_x^-\phi_{ijk}\right)^2 + \left(D_y^-\phi_{ijk}\right)^2 + \left(D_z^-\phi_{ijk}\right)^2\right)^{1/2}} \right] \tag{2.147}
$$

Curvature can be obtained using the calculated normal as follows.

$$
\kappa = \nabla \cdot \mathbf{n}
$$
$$
= \frac{\left(\phi_{yy} + \phi_{zz}\right)\phi_x^2 + \left(\phi_{xx} + \phi_{zz}\right)\phi_y^2 + \left(\phi_{xx} + \phi_{yy}\right)\phi_z^2 - 2\phi_x\phi_y\phi_{xy} - 2\phi_x\phi_z\phi_{xz} - 2\phi_y\phi_z\phi_{yz}}{\left(\phi_x^2 + \phi_y^2 + \phi_z^2\right)^{3/2}} \tag{2.148}
$$

A flow diagram of the solution procedure in one time step is shown in Figure 2.5. At the beginning of the simulation, initialization is completed to tabulate the variables on the Knudsen layer and to assign the simulation parameters. After the initialization,

multiple reflections are executed. The temperature and velocities are solved sequentially in an inner loop with coupled solutions until their computational residuals satisfy certain criteria. Note that a maximum iteration is set to prevent unnecessary computations due to slow convergence, even though the residual values may not be satisfied. After obtaining temperature, velocity, pressure, and composition, the level set is calculated with the value of evaporation and convection that affects interface deformation. Finally, physical properties are updated with a given liquid mass fraction. This procedure is repeated until it satisfies the designated computation time.
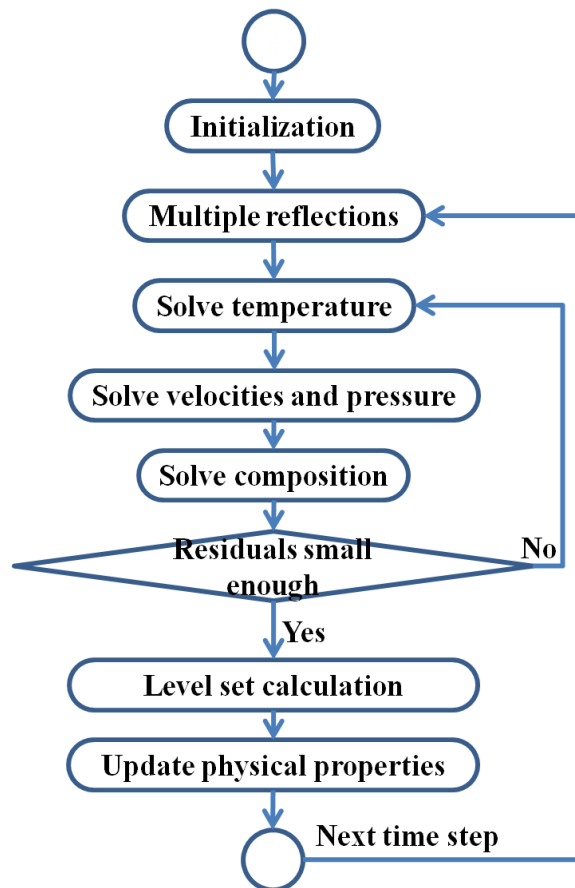
Figure 2.5. Flow diagram of the solution procedure

CHAPTER III

EFFECT OF LASER BEAM MODES ON LASER-MATERIAL PROCESSING

Lasers have been used in wide range of scientific and industrial applications because they offer high energy concentrations, various temporal and spatial distribution and fast processing times. To maximize these advantages, the study of the quality of the processed materials is essential. The quality of the processed materials is highly influenced by various laser parameters, including laser power, moving speed, beam radius, and beam shape. The optimal processing of laser power and moving speed has been the focus of considerable interest. A growing body of theoretical and experimental work has also explored the spatial structure of the laser beam modes in the areas of

modern optics and laser physics [64]. However, one area that has received little quantitative attention is the effects of laser beam spatial distribution or modes on the laser-material interaction process.

While most studies of laser-material interaction modeling have adapted a Gaussian laser beam shape for simplicity [48-50], one often finds several different laser beam shapes, called Transverse Electromagnetic (TEM) modes [51], in a real cavity for the following reasons. First, even in an accurately aligned cavity, some waves travel off-axis as they bounce back and forth, due to the effects of diffraction [52-54]. Second, there is considerable scattering loss that results from scratches on the mirror surface.

A small number of studies have examined the effects of laser beam shapes. For instance, to approximate real beam shapes, Kaplan investigated surface processing with non-Gaussian laser beams obtained by the superposition of several Gaussian beams [65]. To eliminate thermally induced cracks on high alumina ceramics, Triantafyllidis [66] suggested dual laser beam processing consisting of a CO_2 laser with continuous TEM_{01*} and a diode laser with a continuous wave beam. Triantafyllidis also investigated the effects of nonconventional beam geometries on surface cooling rates for Al_2O_3-based ceramic materials [67]. In another work, the effects of laser beam mode on melt pool flow and temperature distribution was studied by Han [68]. In his study, TEM_{00}, cylindrical TEM_{01*} and TEM_{01}, and rectangular TEM_{01} laser beams are considered to be a stationary laser beam.

In this chapter, cylindrical TEM_{00}, TEM_{01*}, TEM_{22}, and Top-hat laser beam shapes are selected. Cylindrical TEM_{00}, TEM_{01*}, and Top-hat have been chosen due to their popularity as commercially available lasers. For comparison, a high order beam

56

mode is also considered, namely TEM$_{22}$. The general formula of TEM modes proposed by Enderlein and Pampaloni [64] are modified for all cases to have the same laser power since the definition of the beam radius is different for each cases. The four different laser beam modes were used to simulate laser-material interaction. The remainder of this chapter is organized as follows.

In section 3.1, formulation of laser beam mode is obtained from Eqn. (2.55). In section 3.2, the response time and overall characteristics of the proposed cases are investigated by comparing absorptivity, depth, width, and the aspect ratio of the laser melted zone. In addition, a dimensionless parameter is derived based on surface pressure balance to understand the deep penetration hole collapse quantitatively for the deep penetration mode. Furthermore, the three stages are further categorized into the initial, transition, and final stages. Within each of these stages, melt pool flow, temperature, recoil pressure, and intensity field are investigated. In section 3.3, the effects of laser beam modes on the laser-material interaction process are discussed and conclusions are offered.

3.1. Formulation of laser beam modes

The energy source terms in the energy equation are considered for several laser beam modes. A three dimensional Cartesian coordinate system is used. A laser is assumed to move the positive x axis at beam scanning speed V_s. Single material such as mild steel is chosen due to its popularity as an engineering material. The laser beam mode functions and shapes are presented in Eqs (2.149)-(2.152) and Figure 3.1. TEM$_{00}$, TEM$_{01*}$,

57

TEM$_{22}$, and Top-hat are derived and modified from Eqn. (2.55) so that all of the laser beams have the same amount of laser power. Specifically, the integration of laser beam intensity distribution functions over the beam area is the same for all cases, as calculated in Eqn. (2.56).

$$\text{TEM}_{00} : I(r) = \frac{2P_0}{\pi w^2} e^{-\frac{2r^2}{w^2}} \tag{2.149}$$

$$\text{TEM}_{01*} : I(r) = \frac{P_0}{2\pi w^2} \frac{8r^2}{w^2} e^{-\frac{2r^2}{w^2}} \tag{2.150}$$

$$\text{TEM}_{22} : I(r,\theta) = \frac{9P_0}{\pi w^2} \left(\frac{2r^2}{w^2}\right)^2 \left[\frac{1}{2}\left(\frac{2r^2}{w^2}\right)^2 - 4\left(\frac{2r^2}{w^2}\right)^2 + 6\right]^2 \cos^2(2\theta) \exp(-\frac{2r^2}{w^2}) \tag{2.151}$$

$$\text{Tophat} : I(r) = \frac{P_0}{\pi w^2} \tag{2.152}$$

where P_0 is given laser power and w is beam radius.
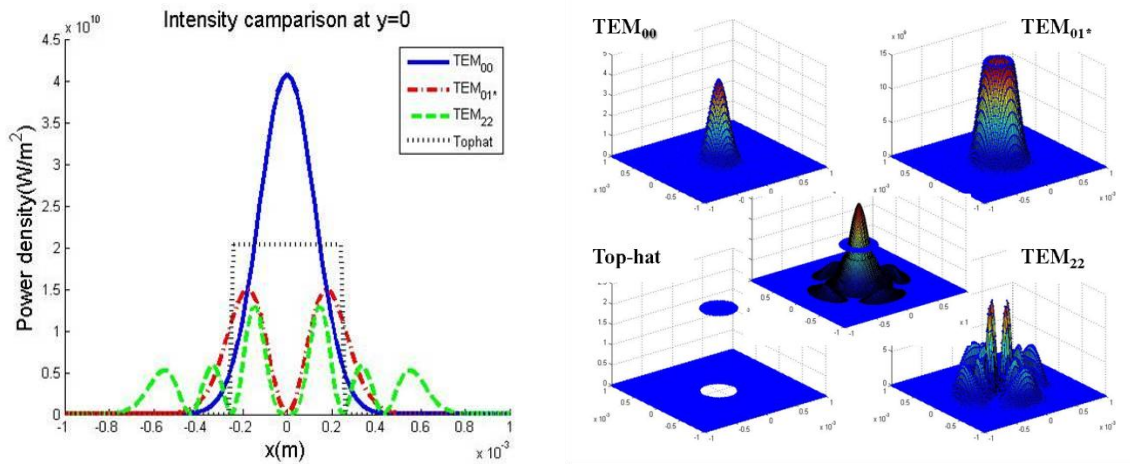
Figure 3.1. Power density of beam modes

Comparisons of the four cases are shown in Figure 3.1. The Gaussian beam shape has a peak laser power density at its center. The laser power density is uniform for the Top-hat shape and its value is exactly half of the peak laser power of a Gaussian beam. The TEM_{01*} laser beam has an annular shape with a peak power smaller than the peaks of the Top-hat laser beam. However, the center of the beam has no laser power. Additionally, the TEM_{22} laser beam has several peak points. Four of which are the strongest peaks. The strongest peaks are located around the center. Another eight peaks are distributed around the strongest peaks. The figure shows that while there are 12 peaks, their respective laser power density values are much smaller than that of a Gaussian beam.

The numerical domain of this simulation is 12.5mm × 5mm × 10mm with the non-uniform mesh. The mesh size becomes the smallest very close to the laser-material interaction zone and its size is 42.8571 μm . Properties of iron are taken and can be found in [69]. A 4 kW CW CO_2 laser with a focused beam radius of 250 μm is assumed to be moving in the positive x direction at 16.93 mm/s (P_{laser} =4kW, w =250 μm, and V_s =16.93mm/s). An initial absorption coefficient is assumed as 0.1.

3.2. Results and discussion

3.1.1. Response times

An average value of penetration depth after 60 ms in the simulation is set as a stabilized final depth, d_s. Based on this penetration depth, rising (t_r) and stabilized (t_s)

times are defined as the time the depth reaches 15% and 90% of the stabilized final depth (d_s), respectively. Together with given response times, initial, transition, and final stages are determined. The initial stage is defined as the period from 0 to t_r and the transition stage is from t_r to t_s. Automatically, the final stage will be the period from t_s to the end of the simulation.

Table 3.1. Response times, stabilized final deep penetration depth (d_s), aspect ratio, and absorptivity

	Response (msec)		Depth (mm)			Aspect ratio			Absorptivity		
	T_R	T_S	Max	Min	Ave.	Max	Max	Ave.	Max	Min	Ave.
TEM$_{00}$	1.57	11.51	2.666	1.852	2.336	2.07	1.13	1.6	0.36	0.17	0.26
TEM$_{01*}$	4.77	17.55	0.696	0.439	0.553	0.56	0.29	0.4	0.14	0.1	0.11
TEM$_{22}$	22.4	78.71	0.139	0.054	0.108	0.13	0.06	0.1	0.10	0.10	0.10
Top-hat	3.04	8.848	2.238	1.21	1.858	1.72	0.74	1.19	0.34	0.15	0.23

Table 3.1 summarizes the response times and the stabilized final depth, d_s, aspect ratio, and absorptivity with its maximum, minimum, and averaged values in the final stage. This result shows that the TEM$_{00}$ laser beam case has the fastest rising time, which is 1.570 ms. The rising times of the top-hat and the TEM$_{01*}$ laser beam cases are 3.04 ms and 4.77 ms, which are almost 2 times and 3 times slower than the time of the TEM$_{00}$ laser beam case, respectively. Furthermore, the TEM$_{22}$ laser beam case has the slowest rising time, which is almost 14 times slower than that of the TEM$_{00}$ laser beam case. We can clearly observe that these rising times are related almost linearly to the laser peak intensity of the TEM$_{00}$, TEM$_{01*}$, and Top-hat laser beam cases. Because of the broader distribution of the laser beam in the TEM$_{22}$ laser beam case, laser power cannot be concentrated, causing the initial response time to be very slow.

The Top-hat laser beam case has the fastest stabilized time, followed in order, by TEM$_{00}$, TEM$_{01*}$, and TEM$_{22}$ laser beam cases. The stabilized time of the TEM$_{01*}$ laser beam case could be simply explained by the relatively low peak intensity. The TEM$_{22}$ laser beam case has the slowest stabilized time because of both its low peak intensity and its broader energy distribution. For the Top-hat laser beam case, the uniform distribution of the laser beam allows the edge of the laser beam to have the same amount of laser beam intensity as the center, shown in Figure 3.1. Thus, near the edge of the laser beam, a target material in the Top-hat laser beam case melts relatively earlier than in the TEM$_{00}$ laser beam case, leading to the formation of a broader and deeper melt pool during the transition stage. Since the thermal diffusivity of liquid iron is greater than that of solid iron, this larger melt pool causes materials to reach their boiling point faster so that the materials are quickly removed. This wider and deeper melt pool allows the Top-hat laser beam case to attain a faster stabilized time.
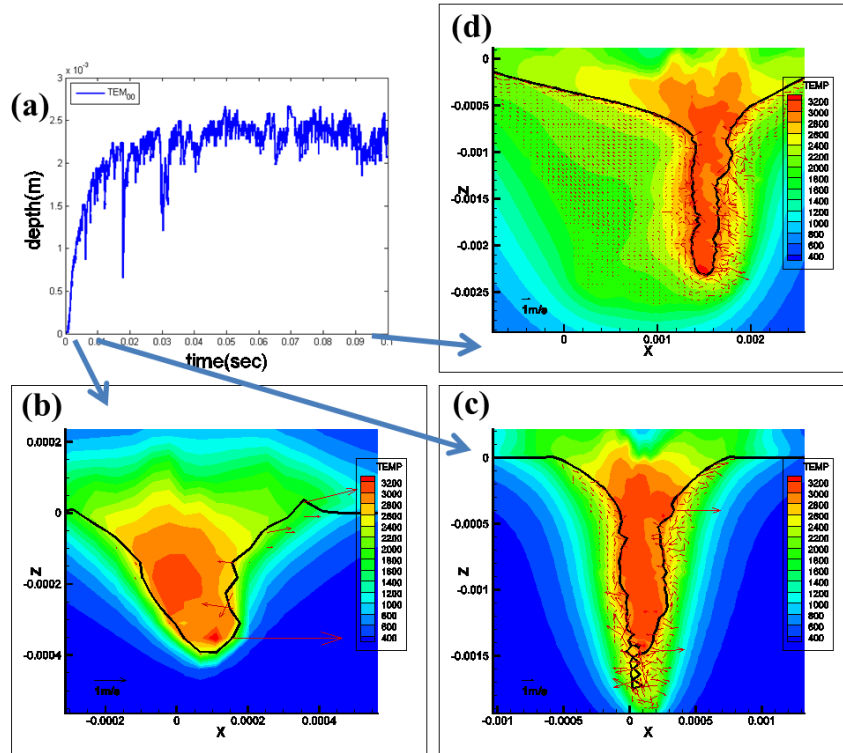
Figure 3.2. Penetration depth, melt pool flow, and temperature distribution of TEM$_{00}$ (a) penetration depth, (b) t=1.610ms (c) t=9.794ms, (d) t=99.70ms
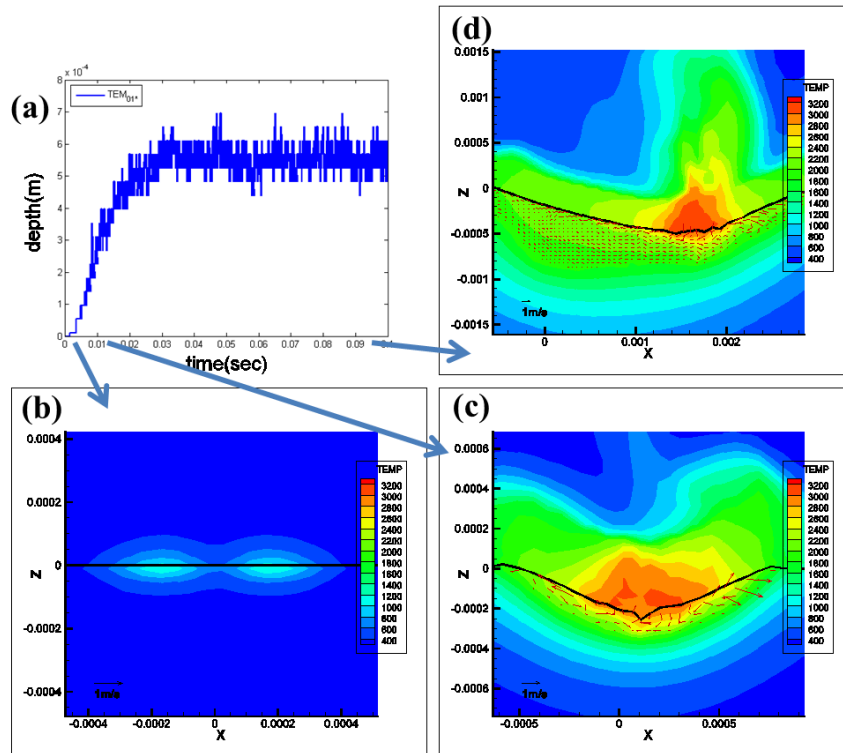
Figure 3.3. Penetration depth, melt pool flow, and temperature distribution of TEM$_{01*}$ (a) penetration depth, (b) t=0.410ms, (c) t=9.410ms, (d) t=98.40ms
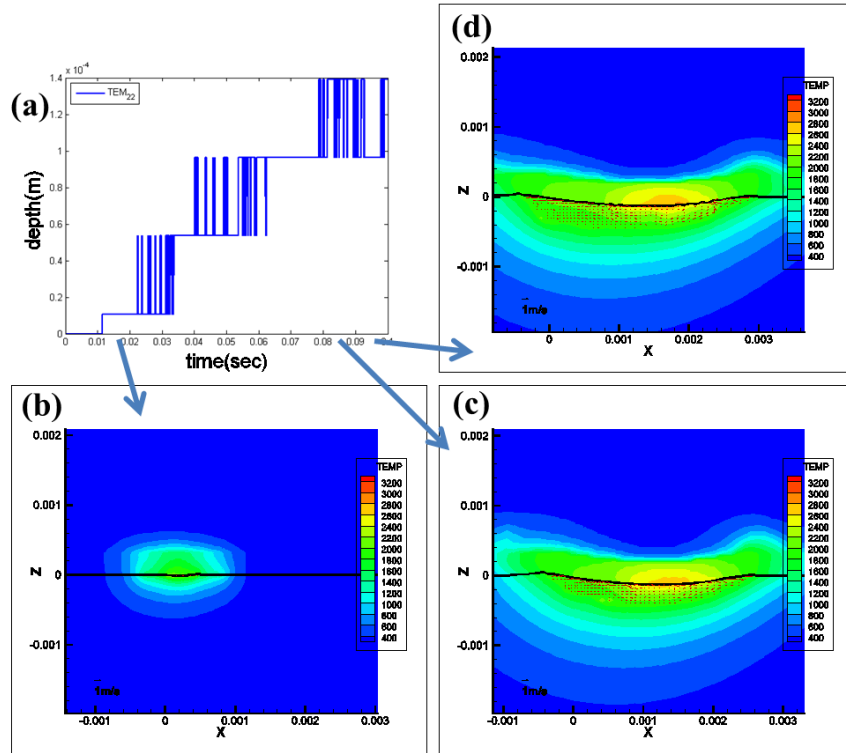
Figure 3.4. Penetration depth, melt pool flow, and temperature distribution of TEM$_{22}$ (a) penetration depth, (b) t=15.01ms, (c) t=85.20ms, (d) t=99.80ms
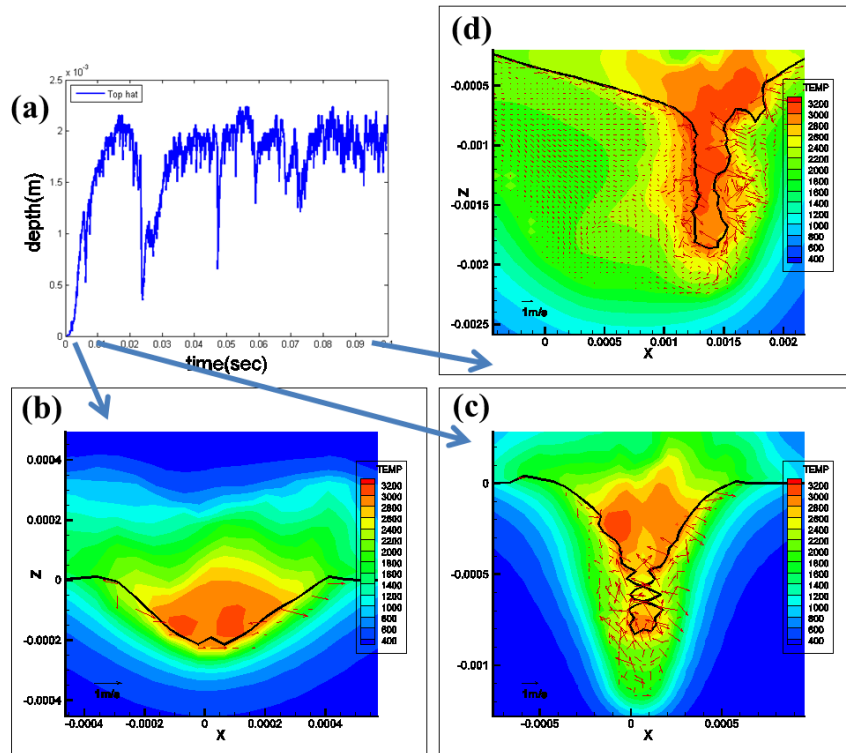
Figure 3.5. Penetration depth, melt pool flow, and temperature distribution of Tophat (a) penetration depth, (b) t=3.010ms, (c) t=6.209ms, (d) t=91.35ms

3.1.2. Effective laser beam absorptivity, and penetration geometry

The variation of depth, width, and aspect ratio is compared and summarized in Table 3.1 which provides maximum, minimum, and average values in the final stage. The aspect ratio in the entire time domain is shown in Figure 3.6 (b). In general, the largest aspect ratio value for each laser beam mode is observed at its transition stage, and then the aspect ratio decreases and stabilizes in the final stage. This trend can be explained by looking at the variation of both depth and width, as shown in Figure 3.2 (a) - Figure 3.5 (a), Figure 3.6 and Table 3.1 . For the TEM_{00}, TEM_{01*}, and Top-hat laser beam cases, the depths reach their final stages within at least 20 ms. However, the width of all cases reach their final stages after 80ms. In other words, the depth is stabilized earlier than the width. This can be explained by the direction of the laser beam, heat transfer, and evaporation. In the initial stage, for most of the cases, the laser is irradiated directly on the flat surface, i.e. the beam comes from the minus z direction in our simulation, there is strong energy concentration on the flat surface in the vertical direction. The concentrated energy makes the target material reach its vaporization temperature, and then, material is removed upward in its vapor phase. Hence, penetration gets deeper as soon as the laser irradiates, whereas width grows gradually while transferring the energy from the center to the wall by conduction and convection, i.e. both positive and negative y directions in our simulation.
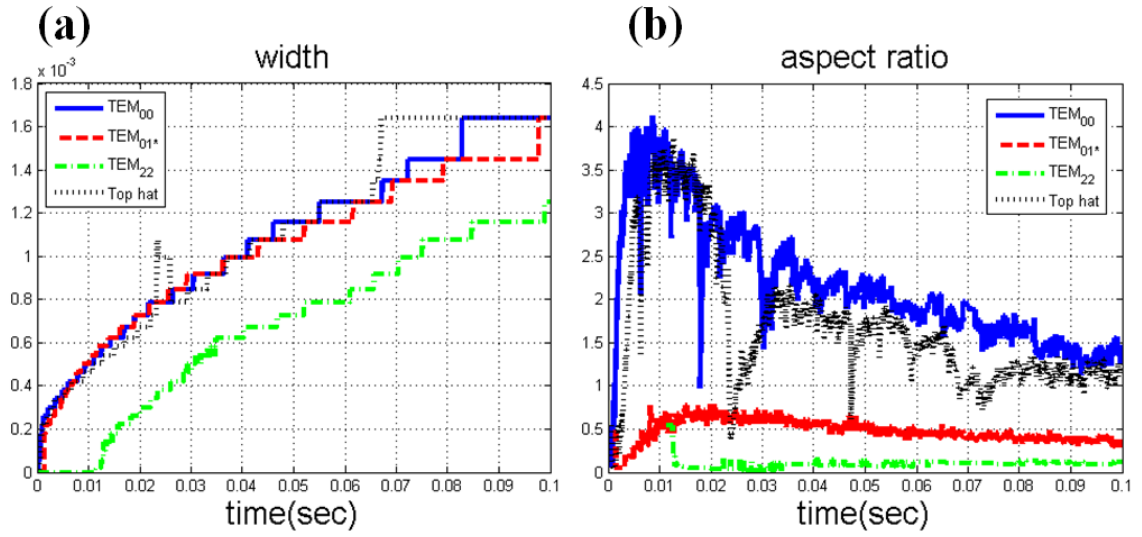
Figure 3.6. Comparison of penetration width (a) and aspect ratio (b)
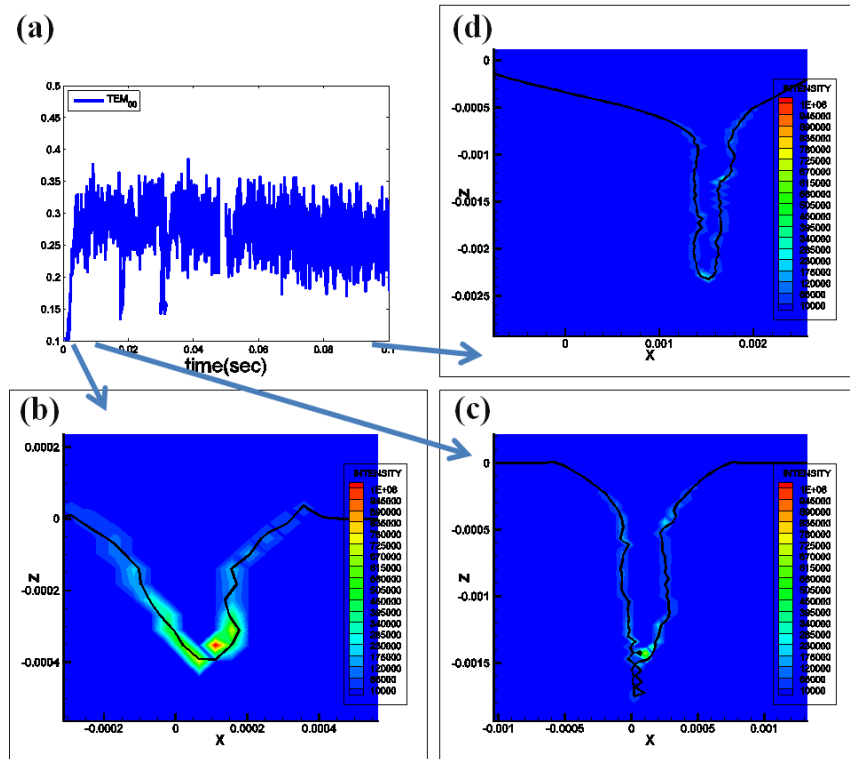
Figure 3.7. Absorptivity and intensity distribution of TEM_{00}, (a) absorptivity, (b) t=1.610ms (c) t=9.794ms, (d) t=99.70ms
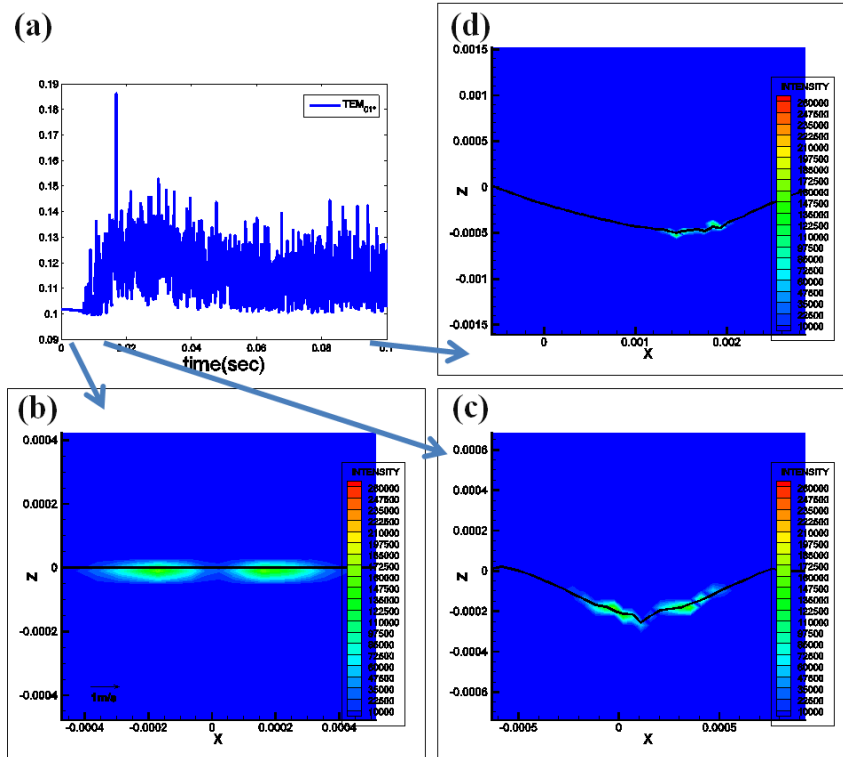
Figure 3.8. Absorptivity and intensity distribution of TEM_{01*}, (a) absorptivity, (b) t=0.410ms, (c) t=9.410ms, (d) t=98.40ms
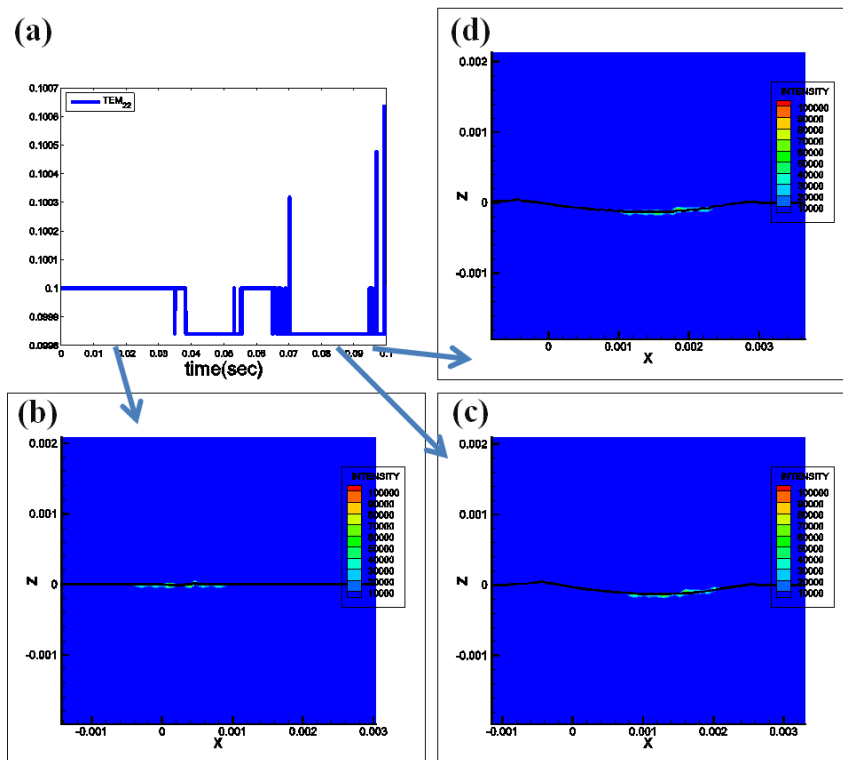
Figure 3.9. Absorptivity and intensity distribution of TEM_{22}, (a) absorptivity, (b) t=15.01ms, (c) t=85.20ms, (d) t=99.80ms
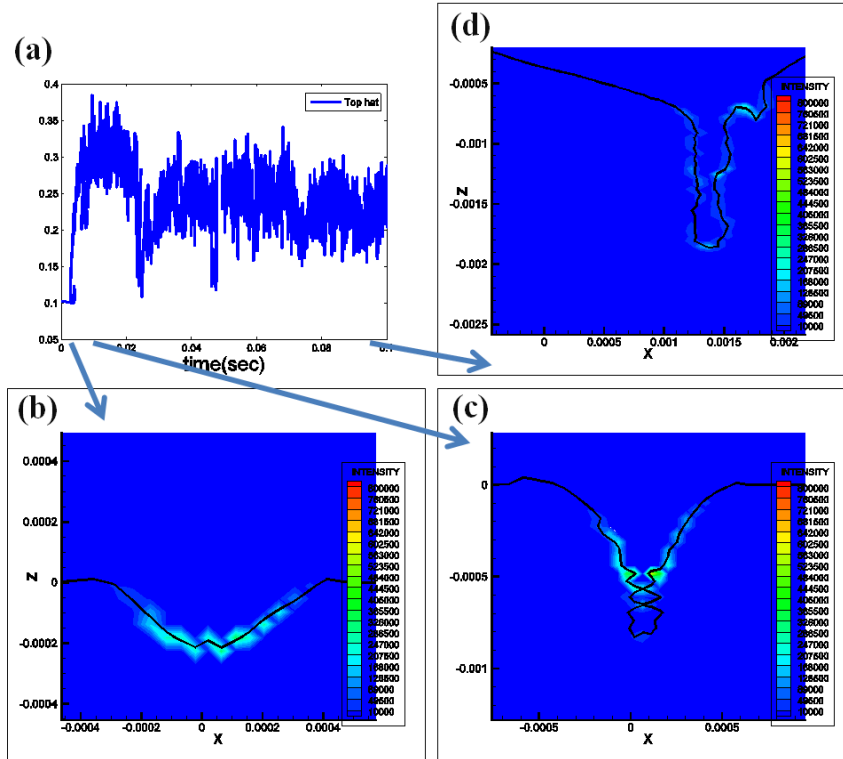
Figure 3.10. Absorptivity and intensity distribution of Tophat, (a) absorptivity, (b) t=3.010ms, (c) t=6.209ms, (d) t=91.35ms

Since there is not enough laser energy to evaporate the target material, for the TEM$_{22}$ laser beam case, no significant depth changes are observed for entire simulation time. However, after 10 ms, width starts to form as shown in Table 3.1 and it becomes 1.2 mm wide. Aspect ratios for the TEM$_{00}$ and Top-hat laser beam cases are greater than 1, while TEM$_{01*}$ and TEM$_{22}$ laser beam cases have values less than 1 in the final stage. In the fields of the laser-material interaction, various definitions of penetration mode are found. In this study, the deep penetration mode and the conduction mode can be defined as where aspect ratio is greater or equal to 1 and less than 1, respectively. According to this definition, the TEM$_{00}$ and Top-hat laser beam cases are clearly of the deep penetration mode. Although, the evaporation phenomenon is observed in the TEM$_{01*}$, the removed material is not enough to make its aspect ratio greater or equal to 1. Therefore, TEM$_{01*}$ and TEM$_{22}$ laser beam cases would be categorized of the conduction mode.

Absorptivity is closely related to penetration depth because of multiple reflections [70-73]. Our results also show this relationship with more detail in Figure 3.7 through Figure 3.10. In the initial and transition stage, the TEM_{00} and Top-hat laser beam cases show an smooth increase of absorptivity. In the final stage, the absorptivity values of these two cases are between 0.1 and 0.45, which reflects the fluctuation in the deep penetration hole. This fluctuation can be explained by the variation of surface forces, especially the thermo-capillary force, capillary force, and recoil pressure. The thermo-capillary force and capillary force tend to close the deep penetration hole. On the other hand, the recoil pressure tends to open the deep penetration hole. These forces exist together and mostly maintain the equilibrium with little variation during the laser-material interaction. This little variation creates the fluctuation of depth of the deep penetration hole. However, when the humps and necks are observed, these geometric variations increase surface tension forces. Due to increased surface tension forces, the equilibrium on the surface is broken. Therefore, a penetration hole collapses and penetration depth decreases suddenly as shown in Figure 3.2 (a) and Figure 3.5 (a). For the TEM_{01*} and TEM_{22} laser beam cases, however, no strong relation is observed since no deep penetration occurs.

3.1.3. Criteria for keyhole collapse

Keyhole formed in the deep penetration mode is fluctuating due to the pressure balance of the recoil pressure and surface tensions. If the balance is broken, keyhole is collapsed. This phenomenon is well depicted with the sudden depth drop, as seen in the Figure 3.2 (a) and Figure 3.5 (a). This keyhole collapse can be predicted as analyzing

surface forces. The strong laser intensity, obtained by the multiple reflections, causes evaporation and creates high recoil pressure on the L/V interface. This high recoil pressure changes the surface geometry and this geometry variation changes the capillary force, since the capillary force is highly influenced by the geometric parameters such as the curvature and normal. Since the surface tension plays a critical role to close keyhole, absolute values of the surface tension increases as the capillary force increases. Therefore, keyhole is closed and collapsed. [40].

To explain this keyhole collapse quantitatively, a dimensionless parameter is introduced as

$$\frac{\left(\dfrac{\rho_s v_s + \rho_v v_v}{2\rho_s v_s} P_{sat}(T_s) - \| -\sigma n \kappa + \Delta_s T \dfrac{d\sigma}{dT} \| \right) V_s}{I(r)} = C_1 \tag{2.153}$$

This parameters is derived from the pressure balance on the surface [74] as

$$p_v - p_\sigma = p_g + p_h - p_l \tag{2.154}$$

where p_v is vaporization pressure, p_l is radiation pressure, p_σ is surface tension pressure, p_g is hydrostatic pressure, and p_h is hydrodynamic pressure. Duley [74] compared these numerical values and showed that the p_l, p_h, and p_g are significantly smaller than the p_v and p_σ. Therefore, the formal variables are regarded as a constant value C.

$$p_v - p_\sigma = C \tag{2.155}$$

when substituting the vaporization pressure [69] and surface tension terms into Eqn. (2.155), we can obtain

$$\frac{\rho_s v_s + \rho_v v_v}{2\rho_s v_s} P_{sat}(T_s) - \| -\sigma \mathrm{n}\kappa + \Delta_s T \frac{d\sigma}{dT} \| = C \tag{2.156}$$

To nondimensionalize, a laser power density is divided and the laser scanning speed is multiplied from Eq (2.156). Hence, the dimensionless parameter is presented in Eqn. (2.153).

This dimensionless parameter is obtained during the laser-material interaction and shown in Figure 3.11 for the deep penetration mode, TEM_{00} and Top-hat laser beam cases. For the TEM_{00} laser beam case, the relationship between the dimensionless parameter and the deep penetration collapse can be found as comparing Figure 3.2 (a) and Figure 3.11 (a). The range of this dimensionless parameter is between -2×10^{-6} and 2×10^{-6} when there is no significant geometric change. However, when the deep penetration hole is collapsed, the dimensionless parameter becomes -6.73×10^{-6} and -9.02×10^{-6} at 0.0173s and 0.0293s, respectively. Figure 3.5 (a) and Figure 3.11(b) show the depth and dimensionless parameter for the Top-hat laser beam case, respectively. The relationship between the dimensionless parameter for the Top-hat laser beam case is obvious as comparing Figure 3.5 (a) and Figure 3.11 (b). The range of this dimensionless parameter is similar to the case of TEM_{00} laser beam when there is no significant geometric change. However, the deep penetration hole is collapsed when the dimensionless parameter becomes -1.118×10^{-5} and -7.792×10^{-6} at 0.0233s and 0.0465s, respectively. The dimensionless parameter of the Top-hat laser beam case is greater than the TEM_{00} laser beam case. This value indicates that the time period of keyhole collapsed is longer and geometry of the melt pool is less stable. This analysis shows strong relationship between the deep penetration hole collapse and the dimensionless parameter

quantitatively. Hence, this dimensionless parameter could be used to provide criteria of the deep penetration hole collapse.
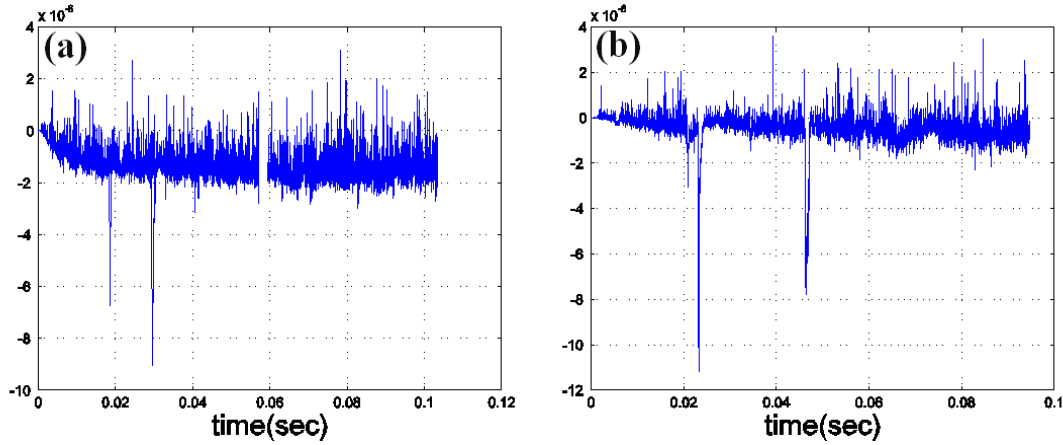
Figure 3.11. Variation of dimensionless parameter for the TEM_{00} (a) and Top-hat (b) laser beam case.

3.1.4. Melt pool formation and flow

The fastest liquid flow within the melt pool is chosen and plotted in time domain. This velocity is called the fastest within-melt-pool speed and the fastest within-melt-pool speed is shown in Figure 3.12 (a) - Figure 3.15 (a). Maximum, minimum, and average values in the final stage are summarized in Table 3.2. The TEM_{00} laser beam case has the largest value, followed by the Top-hat, TEM_{01*}, and TEM_{22} laser beam cases. The average fastest within-melt-pool speed is about 440 times, 380 times, 222 times, and 59 times faster than the laser scanning speed of 16.93 mm/s for the TEM_{00}, Top-hat, TEM_{01*} laser beam case, and TEM_{22} laser beam cases, respectively. In particular, the average value of the fastest within-melt-pool speed during the final stage of the TEM_{00} and Top-hat laser beam cases are 7.46 m/s and 6.44 m/s, respectively. Since both cases are of the deep penetration mode containing the deep penetration hole and multiple reflections, the deep penetration wall is heated over the boiling point so that the strong evaporation

exists. This evaporation generates high pressure, called recoil pressure, on the L/V interface. Hence, this recoil pressure becomes a driving force to move the melted material severely compared to the TEM_{01*} and TEM_{22} laser beam cases. The maximum values of the fastest within-melt-pool speed in the final stage for the TEM_{00}, TEM_{01*}, and Top-hat laser beam cases are 54.93 m/s, 46.97 m/s, and 38.74 m/s, respectively. These values are 1 order higher than that of the TEM_{22} laser beam case. These results recount that the existence of evaporation phenomena affects the melt pool speed strongly through the generation of recoil pressure. For the TEM_{01*} laser beam case, an average value of the fastest within-melt-pool speed is 3.77 m/s which is almost a half less than the TEM_{00} and Top-hat laser beam cases, even though they have similar maximum values of the fastest within-melt-pool speed. This can be explained by comparing the speed and area where the recoil pressure is observed. The TEM_{00} and Top-hat laser beam cases have large areas of recoil pressure as seen in Figure 3.12 and Figure 3.15. By comparing the large areas of recoil pressure with the fastest within-melt-pool speed, the strong relationship between the existence of the recoil pressure and the high melt pool velocity is clear. On the other hand, as predicted, the recoil pressure for the TEM_{01*} laser beam case is hardly seen as shown in Figure 3.13. Furthermore, for the TEM_{22} laser beam case, the melt pool speed is increased slowly due to the absence of the evaporation phenomena as seen in Figure 3.14.

Table 3.2. The fastest within-melt-pool speed in the final stage

	Fastest within-melt-pool speed (m/s)		
	Max val.	Min val.	Ave. val
TEM_{00}	54.93	1.56	7.46
TEM_{01*}	46.97	1.09	3.77
TEM_{22}	1.36	0.84	1

Tophat	38.74	1.56	6.44

According to our simulation results, all of the cases share four flow patterns. These characteristics in flow motion can be seen in Figure 3.2 - Figure 3.5. The first flow pattern is a front-wall strong flow pattern. While the laser beam irradiates the front wall of the penetration hole directly, the rear wall absorbs the energy indirectly by the reflected laser beam. Since the front wall accumulates more energy than the rear wall, the heat in the front wall evaporates more material. The more the material evaporates, the higher the pressure of the melted area. Thus, the front wall has strong flow patterns.

The second flow pattern is a liquid material removal pattern following the L/V interface. Matsunawa and Semak [75, 76] found this flow pattern in their simulation. This pattern can be found by looking at directions of melt pool flows around the L/V interfaces in all cases. Recoil pressure removes the liquid material not only toward the side walls, but also, up the front wall. In addition, the rear wall also contributes to the elimination of the liquid material formed near the laser-material interaction zone.

The third flow pattern is a swirling vortex pattern initiated just below the L/V interface. Material properties change dramatically at the L/V interface. Since viscosity is the function of the position, temperature, and liquid fraction, a very thin flow layer is formed at the L/V interface. Hence, different values of the viscosity along the flow layer cause velocity variation, such as boundary layers. This velocity variation generates pressure gradients. The existence of the pressure gradients initiates separation and forms swirling vortices immediately beneath the L/V interface.
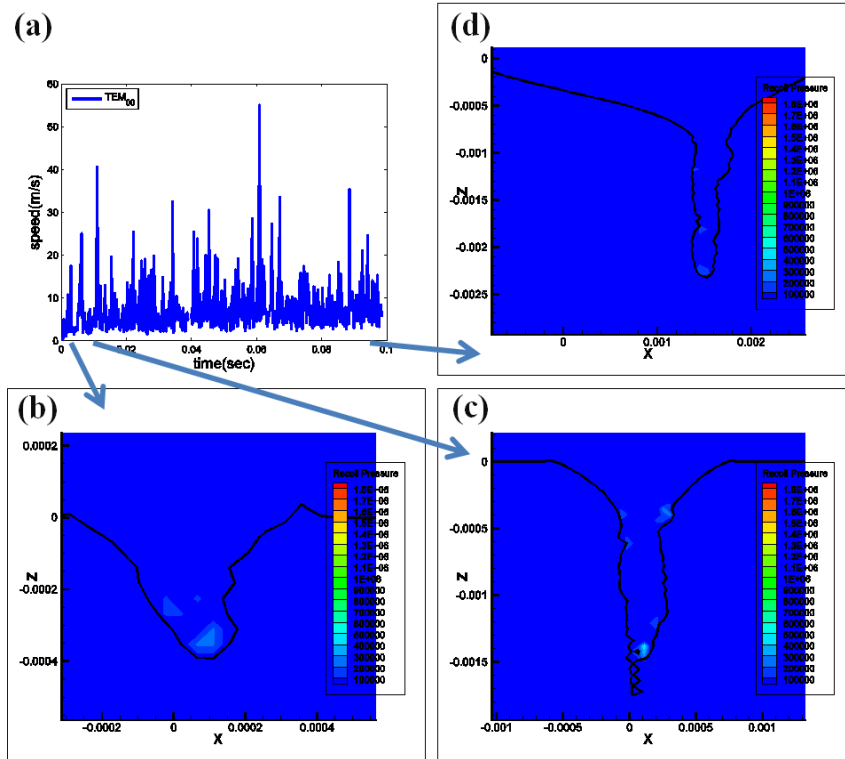
Figure 3.12. The fastest within-melt-pool speed and pressure distribution of TEM_{00}, (a) the fastest within-melt-pool speed, (b) t=1.610ms (c) t=9.794ms, (d) t=99.70ms
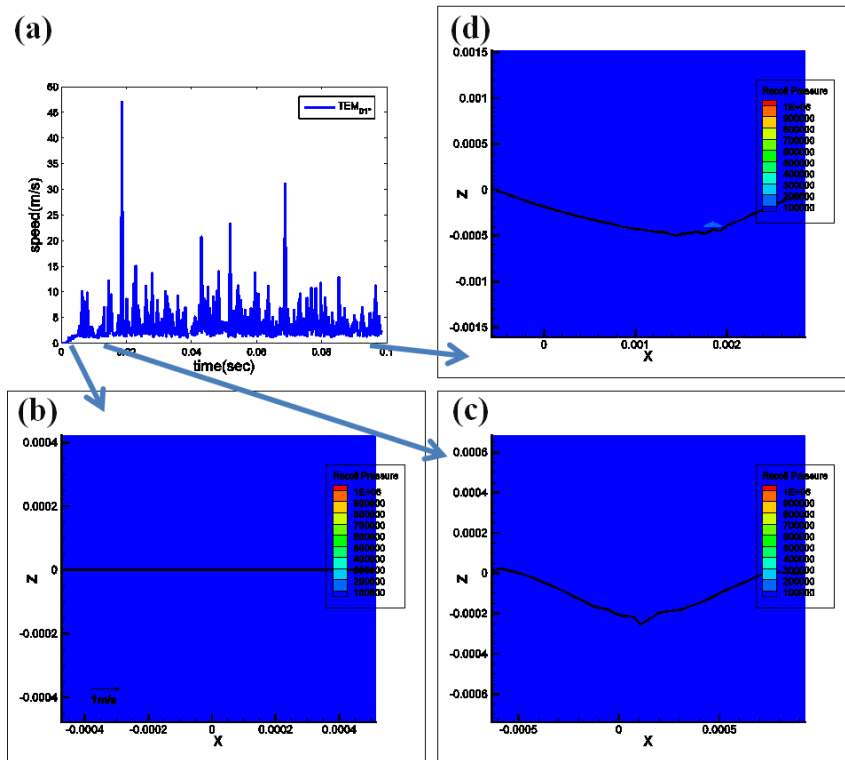
Figure 3.13. The fastest within-melt-pool speed and pressure distribution of TEM_{01*}, (a) the fastest within-melt-pool speed, (b) t=0.410ms, (c) t=9.410ms, (d) t=98.40ms
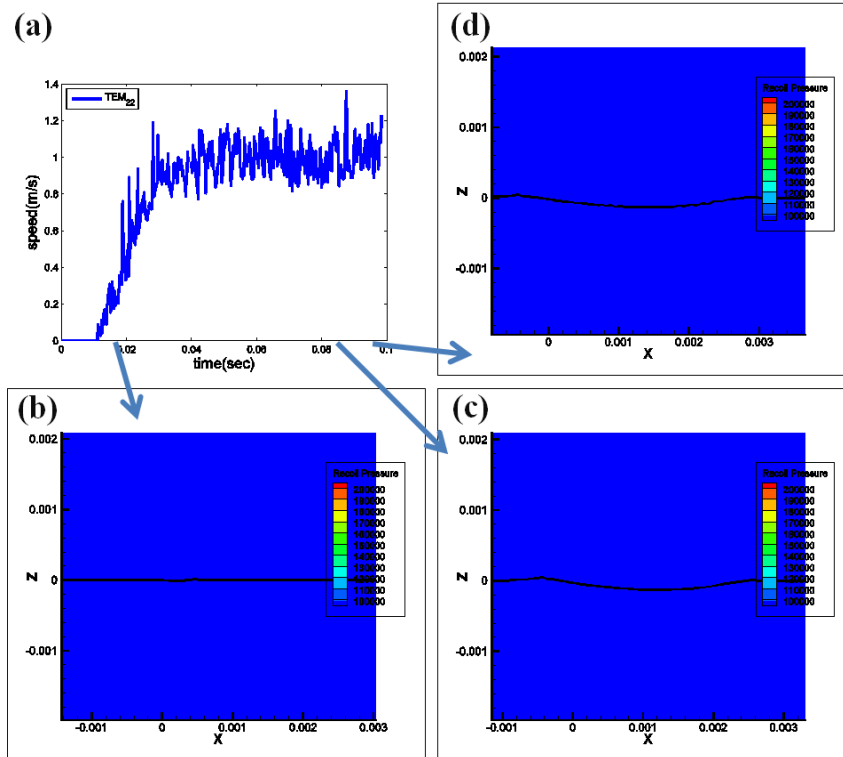
Figure 3.14. The fastest within-melt-pool speed and pressure distribution of TEM_{22}, (a) the fastest within-melt-pool speed, (b) t=15.01ms, (c) t=85.20ms, (d) t=99.80ms
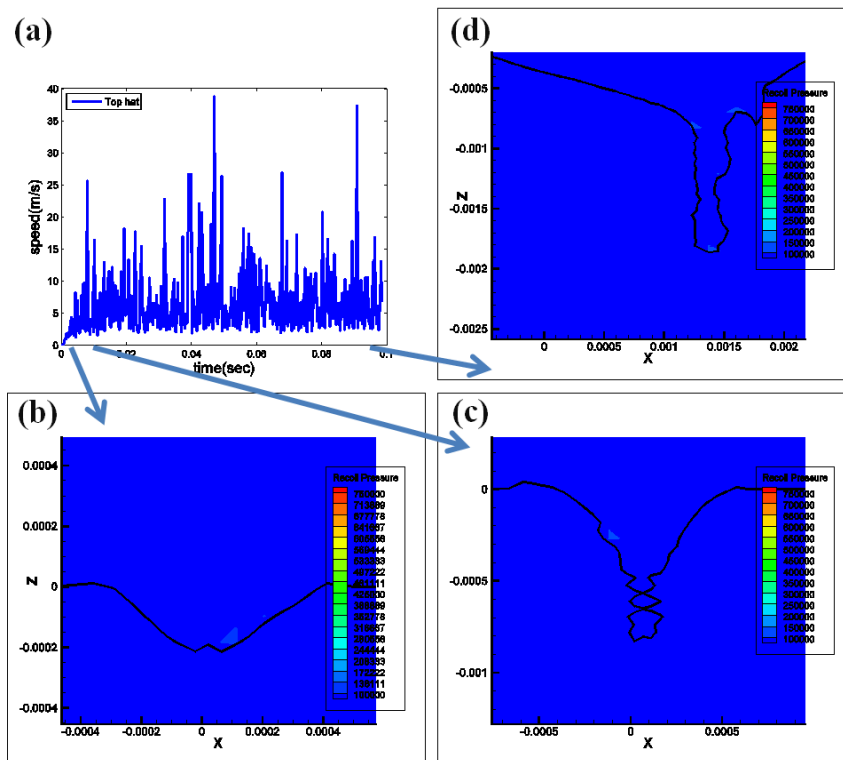
Figure 3.15. The fastest within-melt-pool speed and pressure distribution of Tophat (a) the fastest within-melt-pool speed, (b) t=3.010ms, (c) t=6.209ms, (d) t=91.35ms

Finally, a circular motion pattern can be seen in the back and bottom of the rear melt pool. The removed liquid material from the laser-material interaction zone gathers at the tail of the rear melt pool and is redirected to the bottom of the melt pool. These regional flows, along with the other flows initiated by localized swirling flows at the L/V interface, coalesce into one flow. This merged flow moves back toward the laser-material interaction zone and encounters the flow generated from the laser-material interaction zone. Hence, these flows start to mix and form several circular motions.

While the laser-material interaction with different laser modes overlaps these four flow patterns, there are specific flow patterns for each laser beam case. For the TEM$_{00}$ laser beam case, the variations of the flows and temperature in the X-Z plane are shown in Figure 3.2. The front-wall strong flow pattern can be seen on the walls where there exists recoil pressure during the entire process. Figure 3.2 (b) shows a "tilted" L/V interface, which illustrates how multiple reflections play a key role in deep penetration formation. During the transition stage as shown in Figure 3.2 (c), the melt pool moves randomly due to the existence of recoil pressure and the shallow layer of the melt pool. This flow in the transition stage agrees with Ki's simulation results [77]. This randomly moving flow around the penetration hole observed during the transition stage is carried on until the termination of the simulation as shown in Figure 3.2 (d). The front-wall strong flow pattern is also observed at both the front wall and the tip of the penetration hole as shown in Figure 3.2 (d), where the high temperature region has a good match with the recoil pressure distribution shown in Figure 3.2 (d). The circulation motion pattern, which was observed previously [78], is seen in Figure 3.2 (d). Figure 3.2 (d) observes five circulation motions. Three of these small circulation motions are found just below

the L/V interface. The other two circulation motions form near the bottom of the rear melt pool, where (X, Z) = (0.2~0.5 mm, -1.9 ~ -2.3 mm) and (X, Z) = (0.5~1.0 mm, -1.9~ -2.3 mm). The flow characteristics, initiated from the laser-material interaction zone, determine the locations of these circulation motions, usually near the bottom of the rear melt pool. It is, however, hard to estimate flow patterns around the laser-material interaction zone due to the existence of high recoil pressure and the continuous fluctuation of the deep penetration hole.

For the TEM_{01*} laser beam case, temperature and velocity distribution of the X-Z plane are shown in Figure 3.3. Because of the annular beam shape, both the front and rear walls have the front-wall strong flow pattern during the transition stage, as shown in Figure 3.3 (c). The melt pool thickness is about 0.2 mm during the transition stage and it becomes at maximum 0.6 mm in the rear melt pool during the final stage. The TEM_{01*} laser beam case during the final stage develops more examples of swirling vortex patterns near the L/V interface than any other case. Four swirling vortices are observed in Figure 3.3 (d). The diameter of two vortices, which could be seen almost at the tip of the rear melt pool, is about 0.3 mm each. Another two vortices, which are located near the laser-material interaction zone, have a diameter of about 0.1 mm. No circular motion pattern is observed in the rear melt pool, since there are shallow melt pools and a lack of recoil pressure.

Figure 3.4 shows the temperature and flow fields of the TEM_{22} laser beam case in the X-Z plane. The melt pool is developed slowly during the transition stage compared to any other cases, since there is no evaporation. No liquid metal can be seen until 10.2 ms. Next, a melt pool starts to form and the thickness of the melt pool is about 0.15 mm.

Furthermore, the flow moves moderately during the transition stage as shown in Figure 3.4 (c). In the final stage, the thickness of the melt pool has grown to about 0.4 mm shown in Figure 3.4 (d) which is thinner than the TEM_{01*} laser beam case. During the final stage, as shown in Figure 3.4 (d), the TEM_{22} laser beam case has three examples of a swirling vortex pattern in the rear melt pool. One swirling vortex forms near the tail of the L/V interface. The other two swirling vortices are formed on both the front and rear melt pools. Interestingly, their locations are found to be immediately below the edge of the laser beam radius, when comparing the flow distribution with intensity distribution shown in Figure 3.4 and Figure 3.9. An implication of this result is the possibility that the sudden laser energy drop at the edge of the laser beam generate the swirling vortex pattern due to the significant temperature gradient. However, this implication might be impossible to apply to all the laser-material interaction studies since the existence of the strong evaporation creates the deep penetration hole so that additional physical phenomena, such as the multiple reflection and deep penetration hole fluctuation, influence the flow patterns more significantly. According to this investigation, the TEM_{22} laser beam case performs using the conduction mode. Since the conduction mode has very little evaporation phenomena there are no huge geometry changes in the melted area. These aspects are also well simulated and analyzed by Han [79]. The TEM_{22} laser beam case exhibits a circular motion pattern due to the swirling flow formed by the laser intensity distribution. The location of the circular motion can be varied by the amount of liquid flows. However, no huge difference is made due to the shallow nature of the melt pool. This location of the circular motion is shown in Figure 3.4 (d).

Figure 3.5 depicts temperature and velocity distribution for the Top-hat laser beam case. For the initial stage in Figure 3.5 (b), the melt pool starts to form and its shape looks like an upside down top-hat. This melt pool shape shows the direct impact of the laser beam distribution since the melt pool is shallow so that the multiple reflections are not observed. For the transition stage, the melt pool shape is wider than the TEM_{00} laser beam case. This is reasonable because the intensity of the edge of the Top-hat laser beam is about 4 times greater than that of the TEM_{00} laser beam case. Figure 3.5 (c) shows the collapse of the deep penetration hole. The collapse of the deep penetration hole creates two voids. The flow around the voids moves without any clear pattern, since the equilibrium of the surface forces, such as surface tension and recoil pressure, are broken. Since this case absorbs more energy on the rear wall than the TEM_{00} laser beam case, both the front and rear wall contain the front-wall strong flow pattern during the transition. For the final stage, it shows similar behavior to the TEM_{00} laser beam case. However, the locations of circular motions formed in the rear melt pool changes more frequently. Although the flow coming from the tail of the rear melt pool shows similar flow motions, the flow initiated from the deep penetration hole is different to the TEM_{00} laser beam case due to the substantial depth fluctuation of the deep penetration hole. This aspect is shown in Figure 3.5 (d) on the rear wall. Figure 3.5 (d) has the three circular motions at the locations of (X, Z) = (0.5 mm, -0.8 mm), (X, Z) = (0.8 mm, -1.22 mm), and (X, Z) = (0.85 mm, -0.9 mm).

Based on the understanding of the fluid motion around the keyhole, the fluid flow during the laser cutting process can be discussed. Half of a cone with an open end can be assumed with a moving laser to describe the laser cutting process. Around this half-cone

keyhole during laser cutting process, fluid flow may show several interesting phenomena. The flow pattern at the top surface may be similar to the flow patterns, observed in this section. However, elongated and widened melt pool can be observed at the bottom surface due to surface tension-driven Marangoni convective flows [80]. Furthermore, the formation of eddies along the bottom of a substrate can be seen around this elongated and widened melt pool [33, 81, 82]. So, these flow patterns at the bottom of the substrate with the half-cone keyhole may affect the quality of the bottom area of electrodes during the high speed remote laser cutting as forming micro-sized attachments. To prevent this quality degradation, a narrow groove can be placed right under electrodes where the cutting takes place. The existence of groove may change flow patterns as the molten material is removed both by top and bottom area without forming any eddies [20, 25]. Therefore, consistent cut quality can be obtained.

3.1.5. Intensity and Recoil pressure distribution

The correlation between the peak intensity of the laser beam and stabilized final depth (d_s) is shown in Figure 3.16 summarized in Table 3.3. Despite the different laser beam intensity distribution, the peak intensity of the laser beam and the stabilized final depth show an almost linear relationship. This relationship indicates that the peak intensity plays an important role to estimate the deep penetration hole depth. Many researchers have investigated this relationship with the Gaussian laser beam mode to attain a threshold of the laser power to generate the deep penetration mode [83-85]. Our study may extend the idea of the importance of laser power to estimate the penetration depth of the different laser beam modes.

Table 3.3. Relation between the peak intensity and d_s

	Peak intensity (W/m^2)	Ave. depth (mm)
TEM$_{00}$	4.074 x10^{10}	2.336
TEM$_{01*}$	1.498 x10^{10}	0.553
TEM$_{22}$	1.305 x10^{10}	0.108
Top-hat	2.037 x10^{10}	1.858

The absorbed laser beam intensity and recoil pressure distribution in the X-Z plane for the TEM$_{00}$ beam case are presented in Figure 3.7 and Figure 3.12, respectively. At the initial and the beginning of the transition stages, the laser beam distributes the intensity almost evenly around the deep penetration hole wall as shown in Figure 3.7 (b). Furthermore, the absorbed laser beam intensity near to the tip of the deep penetration hole is 10^{10} W/m^2. This absorbed laser beam on the tip of the deep penetration hole is higher than the absorbed laser beam on the flat surface, where the absorption coefficient is 0.1. A possible explanation of this might be the multiple reflections and the slanted hole shape, which demonstrate this aspect in Figure 3.7 (b). One additional reason for the laser beam concentration at the tip of the deep penetration hole is the cone shape of the deep penetration hole. Since the deep penetration hole has an upside down conical shape, the reflected rays are travelling inside and finally reach the tip of the cone. Figure 3.7 (b) show this result which corroborates the findings of a great deal of the previous works in this field [73, 86, 87]. Because of the lag time between the deep penetration hole formation speed and the laser Scanning speed, the laser beam frequently concentrates on the front deep penetration hole wall. This laser beam concentration makes the front wall deeper, such as in a drilling process [76]. Because of the deepened front wall, humps are formed. With this humps, the deep penetration hole forms a "neck", as shown in Figure

3.7 (d), so that the laser energy is concentrated on both the front and rear deep penetration hole walls. This neck is formed and collapsed repeatedly, which is the one of the indications of creating voids. This void generation mechanism has been well illustrated by Kaplan [88] and it is clearly seen through our simulation results of the TEM_{00} beam case. The recoil pressure distribution is shown in Figure 3.12. Locations of existing recoil pressure correspond to the existence of intensity concentrations and high melt pool velocity, as shown in Figure 3.2, Figure 3.7 and Figure 3.12.
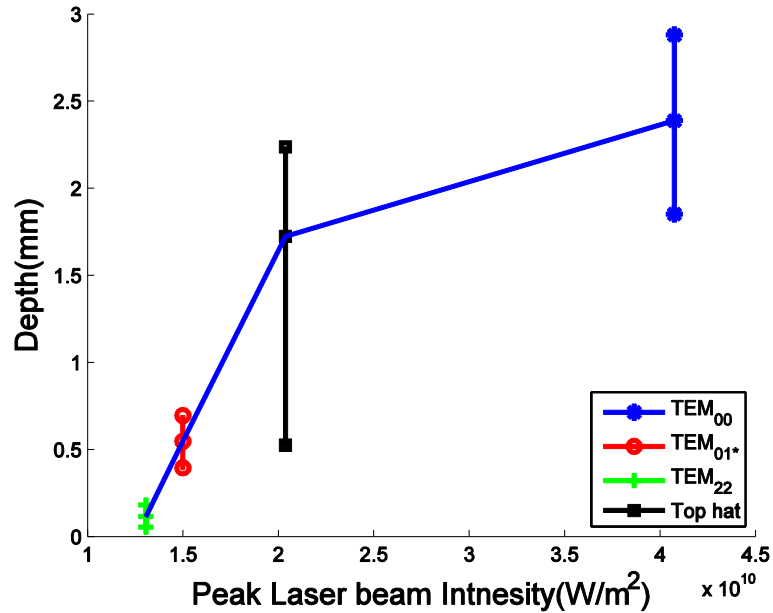
Figure 3.16. Peak laser beam intensity VS averaged final depth

This relationship between intensity and recoil pressure distribution is also observed in the Top-hat laser beam case. While the TEM_{00} and Top-hat laser beam cases share some aspects, since both of them are of the deep penetration mode, there are particular differences to be pointed out. Figure 3.10 and Figure 3.15 show the absorbed laser beam intensity and recoil pressure distributions, respectively, for the Top-hat laser case. First, as shown in Figure 3.10 (b), the absorbed laser beam intensity distributes

around the deep penetration hole wall more uniformly than the TEM_{00} laser beam case, which has a laser concentration usually on the tip of the deep penetration hole and its front wall. The humps are observed occasionally during the final stage, as shown in Figure 3.10 (d) and the deep penetration hole neck is hardly found. The Top-hat laser beam distribution may explain these different features. Since laser energy at the edge of the laser beam is the same as the center, this distribution broadens the melt pool area when compared to the TEM_{00} laser beam case.

The absorbed laser beam intensity and recoil pressure distribution of the TEM_{01*} laser beam case in the X-Z plane are shown in Figure 3.8 and Figure 3.13, respectively. Figure 3.8 (b) shows side views of the TEM_{01*} beam shape. The center of the material has almost no absorbed laser beam intensity. Since the absorbed laser beam intensity is not enough to generate intense boiling, recoil pressure is rarely observed as shown in Figure 3.13. This absence of the recoil pressure explains the relatively slow melt pool velocity compared to the deep penetration mode process, such as the TEM_{00} and Top-hat laser beam cases in this study. The L/V interface geometry and the absorptivity value assure that multiple reflections exist in this case. However, multiple reflections play a less significant role, since there is none of the essential physical phenomenon, evaporation, to create the deep penetration hole.

The absorbed laser beam intensity and recoil pressure distribution of the TEM_{22} laser beam case are shown in Figure 3.9 and Figure 3.14, respectively. The intensity distribution is shown in Figure 3.9 with almost no changes through the entire simulation. This changeless intensity distribution implies that the laser-material interaction with the TEM_{22} laser beam has no significant geometry changes. This unvarying geometry is

closely related to the laser beam distribution. A spread out laser beam energy irradiates a broader area on the material so that the laser beam intensity is low compared to other cases. This low laser beam intensity generates no evaporation of the liquid material. Therefore, no recoil pressure is observed through whole simulation. Figure 3.14 explains well these phenomena.

3.3. Conclusions

This single model fully solved the thermal and the velocity fields in 3D together with the transient evolution of the melt pool, considering the four laser beam modes. Results can be categorized into two modes in terms of laser-material interaction: the deep penetration and conduction modes. While the deep penetration mode is dominant for the TEM_{00} and Top-hat laser beam cases, the TEM_{01*} and TEM_{22} laser beam cases are of the conduction mode. However, the TEM_{01*} laser beam case has one more physical feature, namely evaporation, which is usually observed during the deep penetration process.

The deep penetration mode has faster responses than the conduction mode. More specifically, the TEM_{00} laser beam case forms a melt pool as soon as the laser is irradiated due to energy concentration at its center. The Top-hat laser beam case reaches its stabilized final penetration depth (d_s) first since a broader melt pool area forms. Although the TEM_{01*} laser beam case is categorized in the conduction mode, the existence of evaporation expedites the TEM_{01*} response compared to the typical conduction mode processes, such as seen with the TEM_{22} laser beam case. The average value of the fastest within-melt-pool speed is 440 times greater than that of the laser

beam scanning speed. In addition, the maximum value of the fastest within-melt-pool speed for the TEM_{00}, TEM_{01*}, and Top-hat laser beam cases in the final stage is significantly faster due to evaporation-induced recoil pressure. The relation between the stabilized final depth (d_s) and peak intensity shows an almost linear relationship indicating that peak intensity plays an important role in altering the process from the conduction mode to the deep penetration mode, even with different laser beam modes.

Velocity, temperature, intensity, and recoil pressure distributions together with the evolution of the melt pool and the deep penetration hole are presented. All laser beam modes share four patterns. The four flow patterns are the front-wall strong flow pattern, the liquid material removal pattern following the L/V interface, the swirling vortex pattern initiated just below the L/V interface, and the circular motion pattern in the back and bottom of the rear melt pool.

Furthermore, keyhole collapse is understood quantitatively by analyzing the dimensionless number, obtained using the surface pressure balance. The dimensionless number causing keyhole collapse is less than -6.73×10^{-6}. In addition, the mechanism of keyhole stability and keyhole collapse is also well explained.

Finally, with the given laser parameters, a deep penetration hole forms neck, thus allowing for the potential to create voids during the process. Our simulation results indicate that the deep penetration mode might be more efficient for the welding, drilling, and cutting processes. However, the unstable deep penetration hole, characterized by the keyhole collapse, is still a drawback. The conduction mode demonstrates a stable process. Even though the evaporation occurred, the depth gradually grew and was maintained without severe fluctuation during the entire simulation. Therefore, this mode could be

utilized more efficiently for surface treatment processes, which change the micro structure of the surface, because it has a wide melt pool area and no substantial geometry changes.

CHAPTER IV

LASER CUTTING OF CURRENT COLLECTORS

In this chapter, behaviors of current collectors during the laser cutting are presented. Pure copper and aluminum is chosen for current collectors of the anode and cathode, respectively. The numerical domain of simulation is 75 μm × 30 μm × 75μm with the non-uniform mesh size. A staggered grid is used to obtain the physically proper pressure field [60]. The smallest discrete mesh size is 0.42857μm. The properties of copper and aluminum are shown in Table 4.1 and Table 4.2, respectively.. A CW single mode fiber laser with a focused beam diameter of 11 μm is used and it is moving in positive x direction. A Gaussian laser beam distribution is assumed. The grids for multiple reflection calculations are much finer than the main grid for the sake of a good resolution of solutions. The size of grid for the laser beam is 0.1062μm. The ranges of the

laser power and scanning speed are 50W to 450 W and 1000 mm/s to 5000 mm/s, respectively. The thicknesses of the copper and aluminum are assumed to be 10 μm and 15 μm, respectively. Variable laser parameters are power and scanning speed. The combinations of the simulation conditions are tabulated in Table 4.3 for copper and aluminum. When the depth of the deep penetration hole reaches thicknesses of the substrate materials, called a full penetration cutting, penetration time is provided following simulation termination. When there is partial cutting, maximum penetration depth during the simulation is obtained first, and then the corresponding penetration time is obtained. For the detail analysis of behaviors of current collectors during the laser cutting, copper with the laser power of 250W and scanning speed of 3000 mm/s and Aluminum with the laser power of 150W and scanning speed of 3000 mm/s are chosen.

Table 4.1. Material properties of copper

Property	Value
Melting temperature	1357.77 (K)
Normal boiling temperature	2835.15 (K)
Critical point temperature	8280 (K)
Liquid density	7920 (Kg/m^3)
Solid density	8960 (Kg/m^3)
Kinematic viscosity	3.50E-07 (m^2/s) [89]
Surface tension	1.257-0.0002*(T-1356) (N/m) [90]
Latent heat of vaporization	5.23E+06 (J/kg)
Latent heat of fusion	2.05E+05 (J/kg)
Solid thermal conductivity	317 (W/mK) [91]
Liquid thermal conductivity	157 (W/mK) [91]
Liquid constant-pressure specific heat	571.6218 (J/kgK)
Solid constant-pressure specific heat	385 (J/kgK)[92]
Liquid thermal diffusivity	3.62E-05 (m^2/s)
Solid thermal diffusivity	7.63E-05 (m^2/s)
Laser absorptivity for flat surface	0.05

The simulation results are analyzed and discussed taking into consideration the penetration time and depth. Based on the numerical analysis, laser parameter thresholds are provided for the laser cutting of the current collector materials. Based on the laser parameter thresholds, laser parameters providing thorough cutting for both cases are selected. With given laser parameters, characteristics of full penetration cutting are analyzed. Moreover, melt pool flow, L/V interface geometry and temperature distribution are investigated at selected moments in three-dimensions.

Table 4.2. Material properties of Aluminum

Property	value
Melting temperature	933.47 (K)
Normal boiling temperature	2792 (K)
Critical point temperature	7963 (K)
Liquid density	2333 (Kg/m^3)
Solid density	2700 (Kg/m^3)
Kinematic viscosity	4.43635E-07 (m^2/s)[93]
Surface tension	0.860-0.000115*(T-933.47) (N/m) [94]
Latent heat of vaporization	1.09E+07 (J/kg)
Latent heat of fusion	3.97E+05 (J/kg)
Solid thermal conductivity	237 (W/mK)
Liquid thermal conductivity	93.752 (W/mK)
Liquid constant-pressure specific heat	1255.2 (J/kgK)
Solid constant-pressure specific heat	896.9607116 (J/kgK)
Liquid thermal diffusivity	3.20E-05 (m^2/s)
Solid thermal diffusivity	9.79E-05 (m^2/s)
Laser absorptivity for flat surface	0.07

4.1. Overall behaviors of current collectors and threshold for laser cutting

4.1.1. Thresholds for cutting

The penetration times and depths are shown in Table 4.4 and Table 4.5. When the full penetration cutting occurs, the thickness of substrates is assigned as the depth. For copper, laser power between 250W and 300W is the threshold for 5000 mm/s scanning speed. Laser power between 200W and 250W is the threshold for both 3000 mm/s and 1000 mm/s scanning speeds. For aluminum, laser power between 100W and 150W is the threshold for 5000, 3000, and 1000 mm/s. Laser-material interaction characteristics can be derived for both materials from these thresholds. Interaction time and laser intensity are closely related to laser speed and power. Since the thresholds for copper vary by scanning speed and laser power, interaction time and laser intensity are both effective factors. However, the laser power thresholds for aluminum are the same regardless of the given laser scanning speeds. This indicates that the aluminum laser cutting is more affected by laser intensity than the interaction time. Therefore, both interaction time and laser intensity are important for the copper laser cutting. Moreover, the aluminum laser cutting is highly influenced by the laser intensity.

Table 4.3. Laser processing parameters for simulations on copper and aluminum

Sim #	Copper		Aluminum	
	Power (W)	Speed (mm/s)	Power (W)	Speed (mm/s)
1	200.00		100.00	
2	250.00		150.00	
3	300.00	5000	200.00	5000
4	350.00		250.00	
5	400.00		300.00	
6	450.00		350.00	
7	100.00		50.00	
8	150.00		100.00	
9	200.00	3000	150.00	3000
10	250.00		200.00	
11	300.00		250.00	

12	50.00		50.00	
13	100.00		100.00	
14	150.00	1000	150.00	1000
15	200.00		200.00	
16	250.00		250.00	

4.1.2. Penetration time

Penetration times of the full penetration cutting for copper and aluminum are presented in Figure 4.1 and Figure 4.2, respectively. The total penetration times during full penetration cutting for copper and aluminum have significant differences. The penetration times for aluminum are always less than 1 μs. On the other hand, only when laser power is greater than 300W is the penetration time less than 1 μs for copper.

For copper, the penetration time decreases exponentially when laser power is increased from 250W to 450W. For a laser power of 250W, no full penetration cutting is obtained with a 5000 mm/s scanning speed, and the difference in penetration time between 3000 mm/s and 1000 mm/s scanning speeds is larger than other laser power cases. For a laser power of 300W, slight differences in the penetration time are seen among the 5000, 3000, and 1000 mm/s scanning speeds.

Table 4.4. Simulation results of laser cutting penetration time and depth for copper

Sim #	Penetration	
	Time (μs)	Depth (μm)
1	1.8819	0.957
2	6.7452	4.787
3	0.9064	10.000
4	0.5452	10.000
5	0.4308	10.000
6	0.3762	10.000
7	0.0000	0.000
8	3.2125	0.531
9	6.7681	1.808
10	4.3982	10.000
11	0.8228	10.000

12	0.0000	0.000
13	0.0000	0.000
14	0.7176	0.106
15	6.8708	2.233
16	3.5166	10.000

For the aluminum case, the overall trend is the same as the copper case. However, the aluminum case shows a smoother decrease of penetration time with increasing laser power. While the copper case exhibits significant differences in penetration time with the laser powers of 250W and 300W, relatively less differences in penetration time for the aluminum case are observed.

Table 4.5. Simulation results of laser cutting penetration time and depth for aluminum

Sim #	Penetration	
	Time (μs)	Depth (μm)
1	0.4576	1.382
2	0.3913	15.000
3	0.2541	15.000
4	0.2006	15.000
5	0.1728	15.000
6	0.1606	15.000
7	3.5509	1.382
8	0.4102	1.382
9	0.4018	15.000
10	0.2672	15.000
11	0.2101	15.000
12	3.1564	1.382
13	8.5736	1.808
14	0.3577	15.000
15	0.2498	15.000

16	0.2170	15.000

These results indicate again that the copper may have both interaction time and laser intensity dependent processes, and the aluminum may have only a laser intensity dependent process, likely due to absorption coefficients. The absorption coefficients for a wavelength of 1.070 μm of copper and aluminum are 0.05 and 0.07, respectively. These absorption coefficients are obtained by Bramson's empirical relation [95], which is a a function of wave length and electrical resistivity. The higher the absorption coefficient of the material, the more the energy that can be deposited on the material with the aid of multiple reflections. Furthermore, the melting point of copper is 424.3K higher than that of aluminum. If the melt pool forms, there is more chance to remove liquid material due to the existence of recoil pressure and create the deep penetration hole. Therefore, aluminum is penetrated more rapidly than copper, even though aluminum foils are thicker.
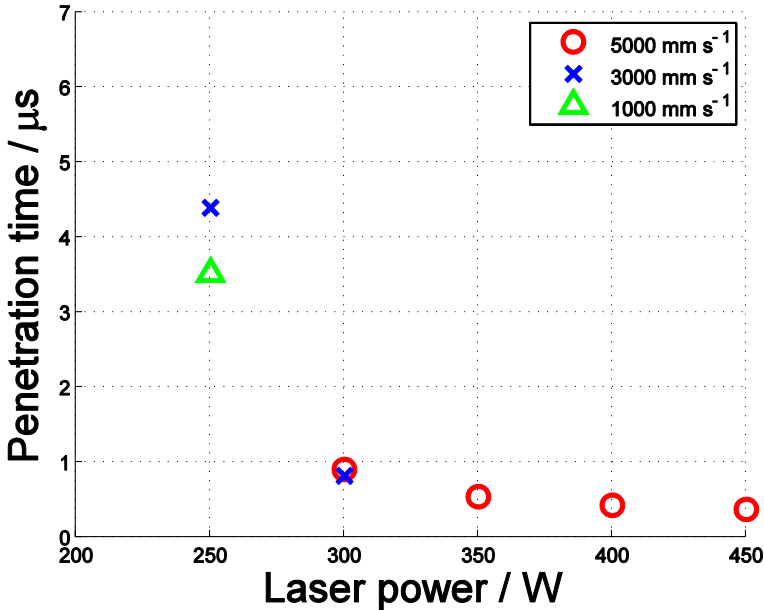
Figure 4.1. Laser cutting penetration time for copper
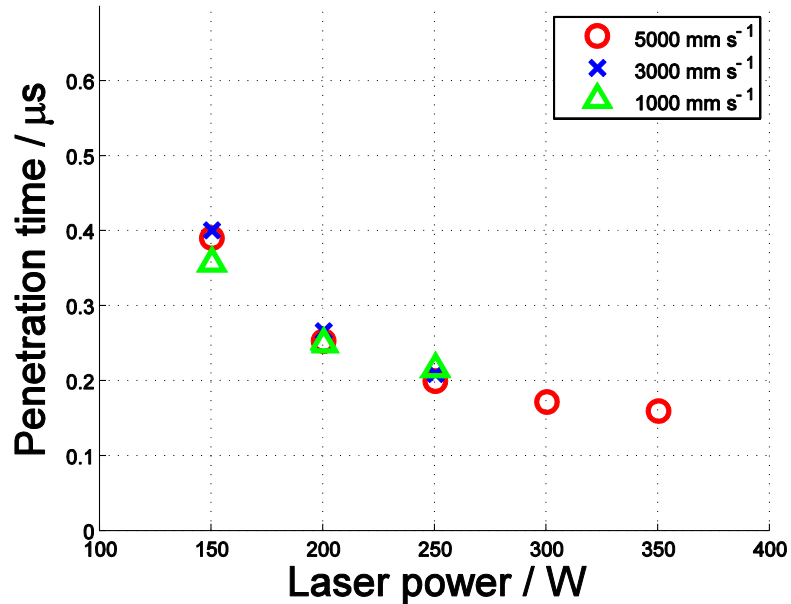
Figure 4.2. Laser cutting penetration time for aluminium

4.1.3. Penetration depth

Full penetration cutting is obtained when the depth of the penetration hole reaches the materials' thicknesses, which are 10 μm and 15 μm for copper and aluminum, respectively. Once full penetration occurs, the penetration depths are automatically assigned. However, partial penetration, which is less penetration depth than the specimens' thicknesses, is obtained if insufficient energy is provided. Therefore, a relationship between the laser operating parameters and the penetration depths could be observed. These results for copper and aluminum are shown in Figure 4.3 and Figure 4.4, respectively. Furthermore, numerical values are shown in Table 4.4 and Table 4.5. For copper, the partial penetration depth increases exponentially when increasing the laser power. Values of the partial penetration vary from 0.106 μm to 4.797 μm, which is half

of the specimen thickness. On the other hand, for aluminum, the partial penetration and full penetration cutting are clearly distinguished between 100W and 150W. The laser power of 150W provides the full penetration. However, the laser power of 100W can provide the partial penetration and the maximum partial penetration depth is 1.808 μm, which is 12% of the specimen thickness. From these results, we conclude again that the aluminum laser cutting is laser intensity dependent.

These results may be possible due to the materials' properties, such as absorptivity and melting points. Since aluminum has a high absorptivity as well as low melting and boiling points compared to copper, aluminum absorbs more energy. Once aluminum absorbs enough energy, the material is evaporated at a relatively fast speed. Therefore, the aluminum laser cutting shows clear differences between partial penetration and full penetration cutting.
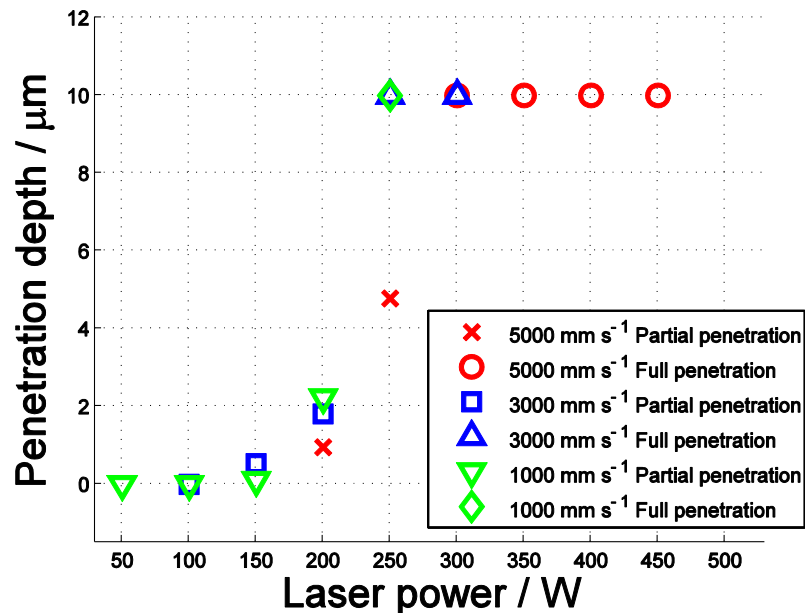
Figure 4.3. Laser cutting penetration depth for copper
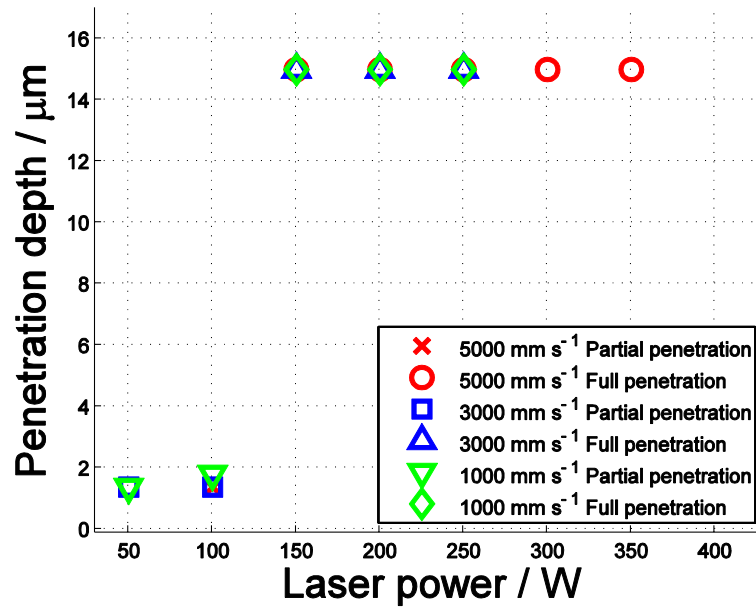
Figure 4.4. Laser cutting penetration depth for aluminium

4.2. Effects of physical characteristics on surface cut quality near the threshold of laser cutting

4.2.1. Characteristics of full penetration cutting for current collectors

Laser parameters are chosen to investigate characteristics of full penetration cutting for current collectors from the previous section. The laser powers of 250W and 150W are chosen for copper and aluminum, respectively. The scanning speed of both materials are 3000 mm/s. Penetration time, depth, width and absorptivity of copper and aluminum are shown in Figure 4.5 and Figure 4.6, respectively. The time necessary for the full penetration of the 10 μm-thick copper and 15 μm-thick aluminum are 4.398 and 0.402 μs, respectively. The penetration time of aluminum is 10.94 times faster than the penetration time of copper even with the thicker substrate of aluminium and lower laser power compared to that of copper. This fact can be explained primarily by investigating

the absorptivity of these materials. Absorptivity is obtained as the ratio of total absorbed energy to given energy density in this study. The total absorbed energy for different materials varies due to different values of the absorption coefficient on a flat surface, the geometry of the deep penetration hole, and the multiple reflections during the process. The absorption coefficients on the flat surfaces of copper and aluminum for the wavelength of 1.070 μm are 0.05 and 0.07, respectively. Those absorption coefficients are increased to 0.135 and 0.304 due to the multiple reflections at the moment where full penetration occurs. Accordingly absorptivity increases and the amount of the absorbed energy on the aluminum substrate is significantly greater than the copper substrate even with a lower laser power. This energy absorption expedites the penetration for aluminum.

Figure 4.5. Penetration time (a) , width (b), and absorptivity (c) of copper with the laser power of 250W and scanning speed of 3000 mm/s
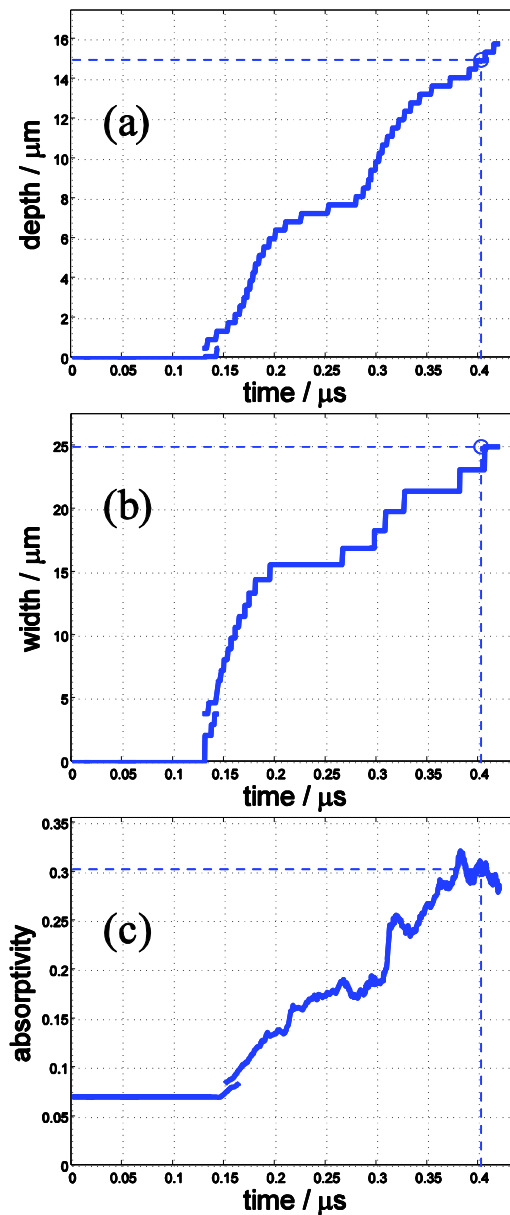
Figure 4.6. Penetration time (a) , width (b), and absorptivity (c) of aluminum with the laser power of 150W and scanning speed of 3000 mm/s

Penetration depth and width with time for copper is shown in Figure 4.5 (a)-(b). Finding the exact width of the deep penetration hole during the process is difficult due to the existence of liquid flow. Hence, in this study, the width of the deep penetration hole is
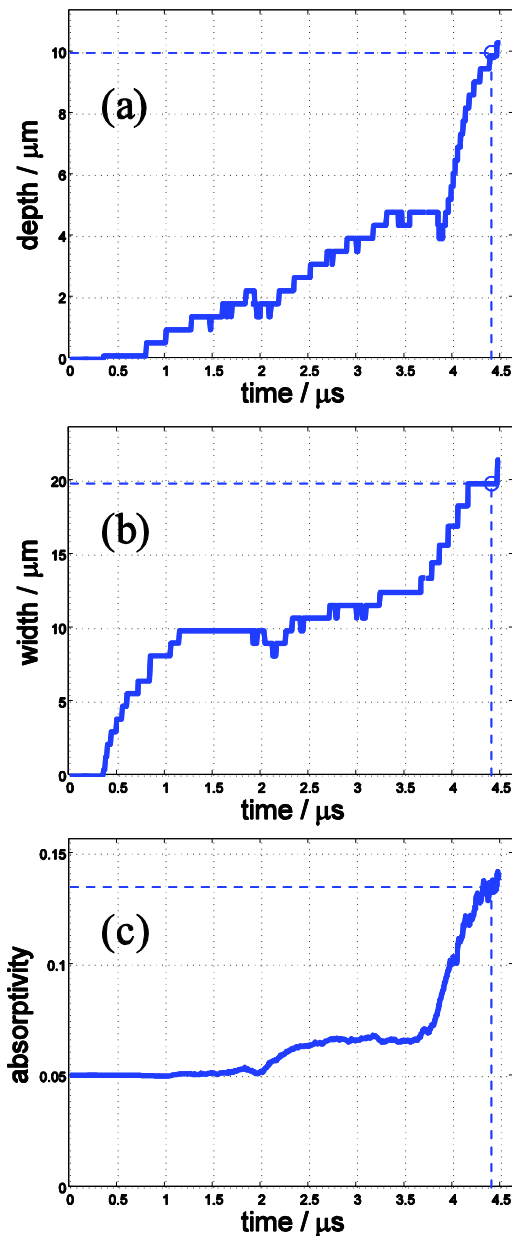
97

defined as the transverse distance between the point where the center of the laser beam is and the closest L/V interface of the deep penetration hole at z=0. As shown in Figure 4.5 (a), the depth increases almost linearly until 3.925μs, at which point it increases suddenly. This may be possible because the laser parameters used for the copper laser cutting are very close to the threshold of laser cutting [96]. With the laser parameters, there exists a transition from partial to full penetration laser cutting. Therefore, 3.925μs can be thought of as a transition point from partial to full penetration laser cutting. The width also increases during the penetration with two different slopes for the full penetration of copper, as clearly seen in Figure 4.5 (b). Fast slopes are shown in the initial and final stages of the laser cutting. The slow slope is shown between these stages. A linear interpolation describes the fast slope as 8.207 m/s and slow slope as 1.208 m/s. This is a significant difference, and it might be caused by the existence of the transition from the partial to full penetration laser cutting. In contrast to copper, aluminum increases both its penetration depth and width relatively smoothly except the time between 0.210 and 0.276 μs until it achieves full penetration, as seen in Figure 4.6 (a) and (b). Within this time, a crest surrounding the hole starts to form above the top of the substrate due to the strong upward fluid flow. At the moment of the formation of the crest, the depth and width stay almost the same.

Figure 4.5 (c) shows the evolution of the absorptivity for copper. The absorptivity increases to 0.064 at 2.500μs, and remains at that value until 3.669μs. After that, the absorptivity increases rapidly and reaches 0.135, which is a 170% increase compared to the absorption coefficient on the flat surface. The sudden increase of absorptivity is highly related to the sudden increase of the penetration depth as seen in Figure 4.5 (a),

since a deeper penetration hole provides more space to increase the number of laser beam reflections [71, 97].

Figure 4.6 (c) shows the evolution of the absorptivity for aluminum. Absorptivity of aluminum increases gradually with several spikes at 0.317 and 0.380 μs due to the geometry of the L/V interface. The net increase of the absorptivity at the end of the simulation is 306.65%. Similarly, this increase is due to multiple reflections.

4.2.2.   Geometry, temperature distribution, and fluid flow

The three-dimensional geometry and temperature distribution during the laser cutting of copper are shown in Figure 4.7. At the beginning of the simulation, a small hole is observed as seen in Figure 4.7 (a)-(b). The crest on the edge of the deep penetration hole forms at 3.892 μs. This crest becomes higher and wider, as seen in Figure 4.7 (e)-(f). As this crest is developing, the wavy shape of the crest on the inner L/V interface is observed in Figure 4.7 (g). Then, this wavy shape of the crest merges with the outer L/V interface, as shown in Figure 4.7 (h). Relatively high temperature is observed on the top and front parts of the L/V interface. Furthermore, the rear part of the L/V interface and the crest on the entrance of the deep penetration hole also show relatively high temperature, due to the multiple reflections, as seen in Figure 4.7 (d)-(f).

Figure 4.8 shows melt pool flow. At 0.881μs, a melt pool is formed below the L/V interface. In this initial stage, the flow of liquid copper moves downward from the point of laser irradiation. After the flow of liquid copper meets the solid interface of copper at the bottom of the melt pool, it moves upward in the transverse direction. This upward flow in the transverse direction is redirected to the rear side of the melt pool. This
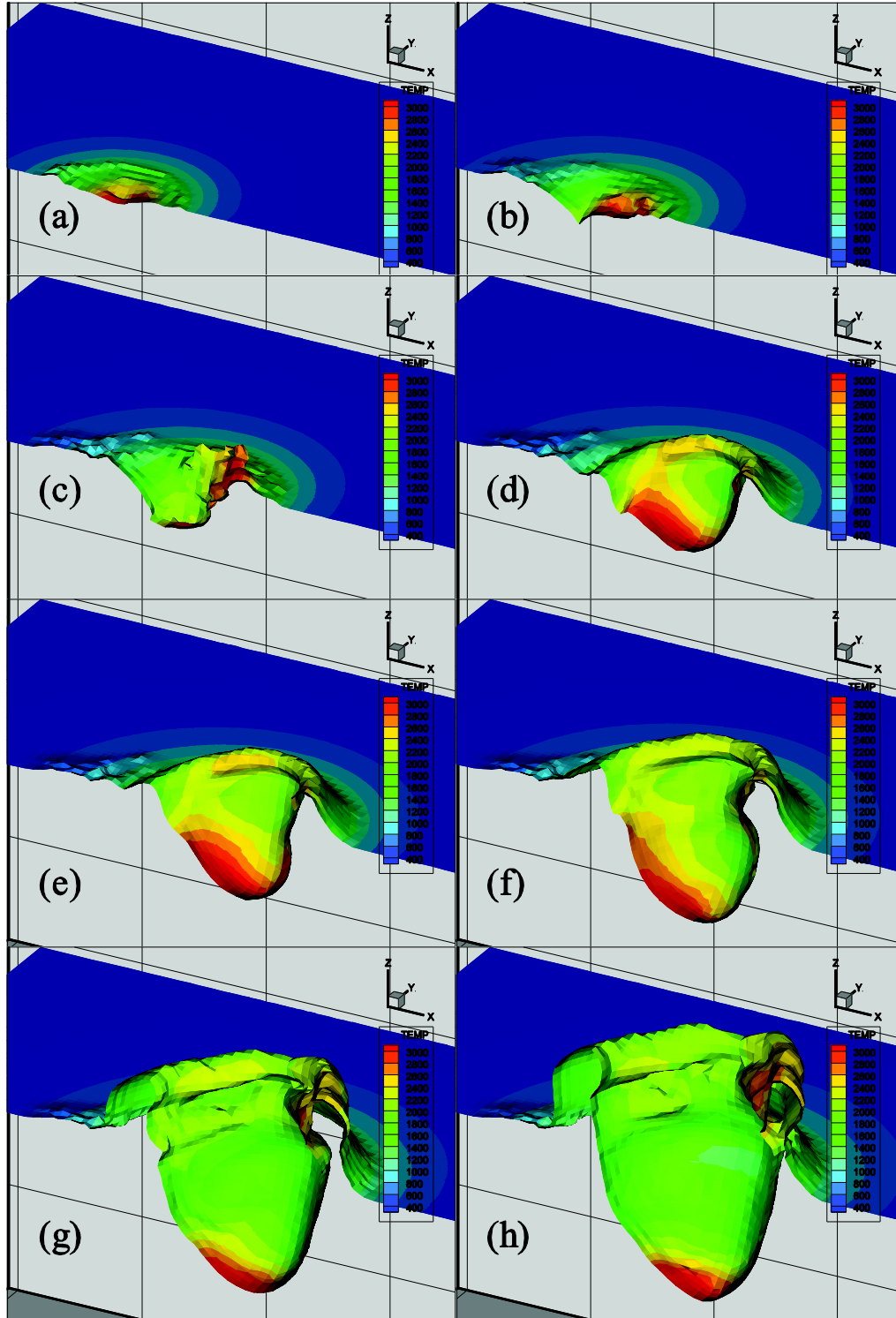
Figure 4.7.Temperature distribution and L/V interface geometry of copper (Laser power : 250W, Scanning speed : 3000 mm/s) at (a) 0.881μs, (b) 3.002 μs, (c) 3.974μs, (d) 4.068μs, (e) 4.246μs, (f) 4.397μs
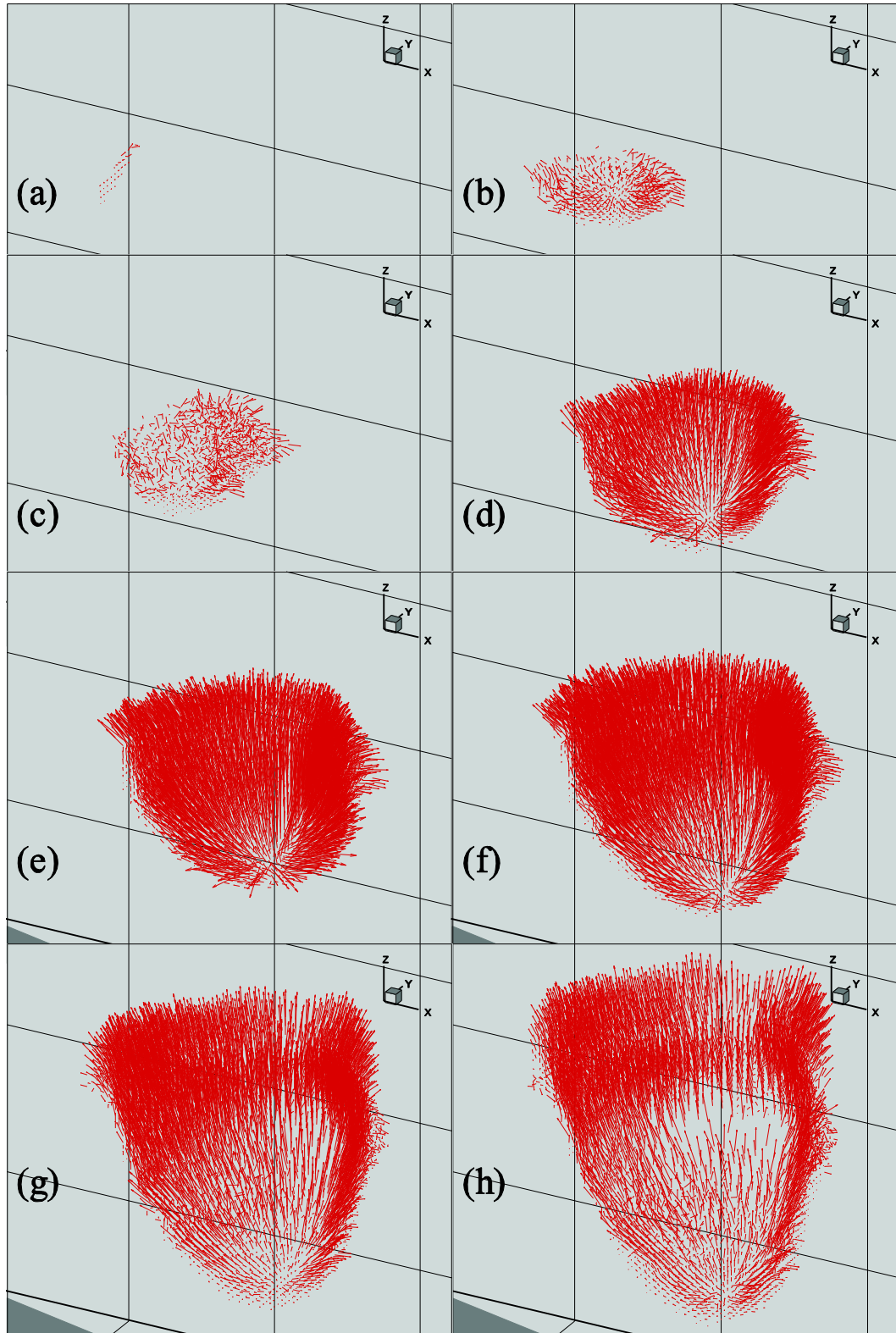
Figure 4.8. Melt pool flow of copper (Laser power : 250W, Scanning speed : 3000 mm/s) at (a) 0.881μs, (b) 3.002 μs, (c) 3.974μs, (d) 4.068μs, (e) 4.246μs, (f) 4.397μs

circulation pattern of the melt pool flow is commonly observed in studies of the laser-material interaction [39, 79, 83, 98]. The deep penetration hole forms at 3.002μs and a very thin liquid layer is observed near the bottom, due to high recoil pressure. The speed of liquid flow becomes faster due to the deeper penetration hole and higher recoil pressure. Therefore, liquid flow is moving outward from the tip of the deep penetration hole. As the liquid copper is removed from the bottom to the side of the deep penetration hole, the momentum of the liquid copper makes it move beyond the top surface of the copper substrate. This movement is the main cause for creating the crest during the cutting process, and this is seen in Figure 4.7 (d). The width of the deep penetration hole is widened and faster melt pool flow develops at 3.974μs. This corresponds to the point of the sudden depth increase, as shown in Figure 4.5 (a). Since absorptivity increases suddenly, as shown in Figure 4.5 (c), copper absorbs more energy so that it is evaporated more rapidly. This rapid evaporation generates even stronger recoil pressure. This stronger recoil pressure makes the melt pool flow faster and more liquid copper is removed. Thus, the penetration depth increases suddenly. The crest becomes higher at 4.068μs, and this crest changes the geometry of the deep penetration hole. Due to the momentum, the height of the crest is about 8μm from the top surface of the copper substrate at 4.397μs. This crest becomes a spatter or forms a recast layer when it solidified. Therefore, undesirable defects, formed by spatter or reattachment, can be prevented by controlling the magnitude of melt pool flow through laser parameters.

Figure 4.9 shows three-dimensional geometry and temperature distribution during the laser cutting of aluminum. In Figure 4.9 (c)-(d), a tilted deep penetration hole is observed due to the multiple reflections. The crest is created between Figure 4.9 (d) and
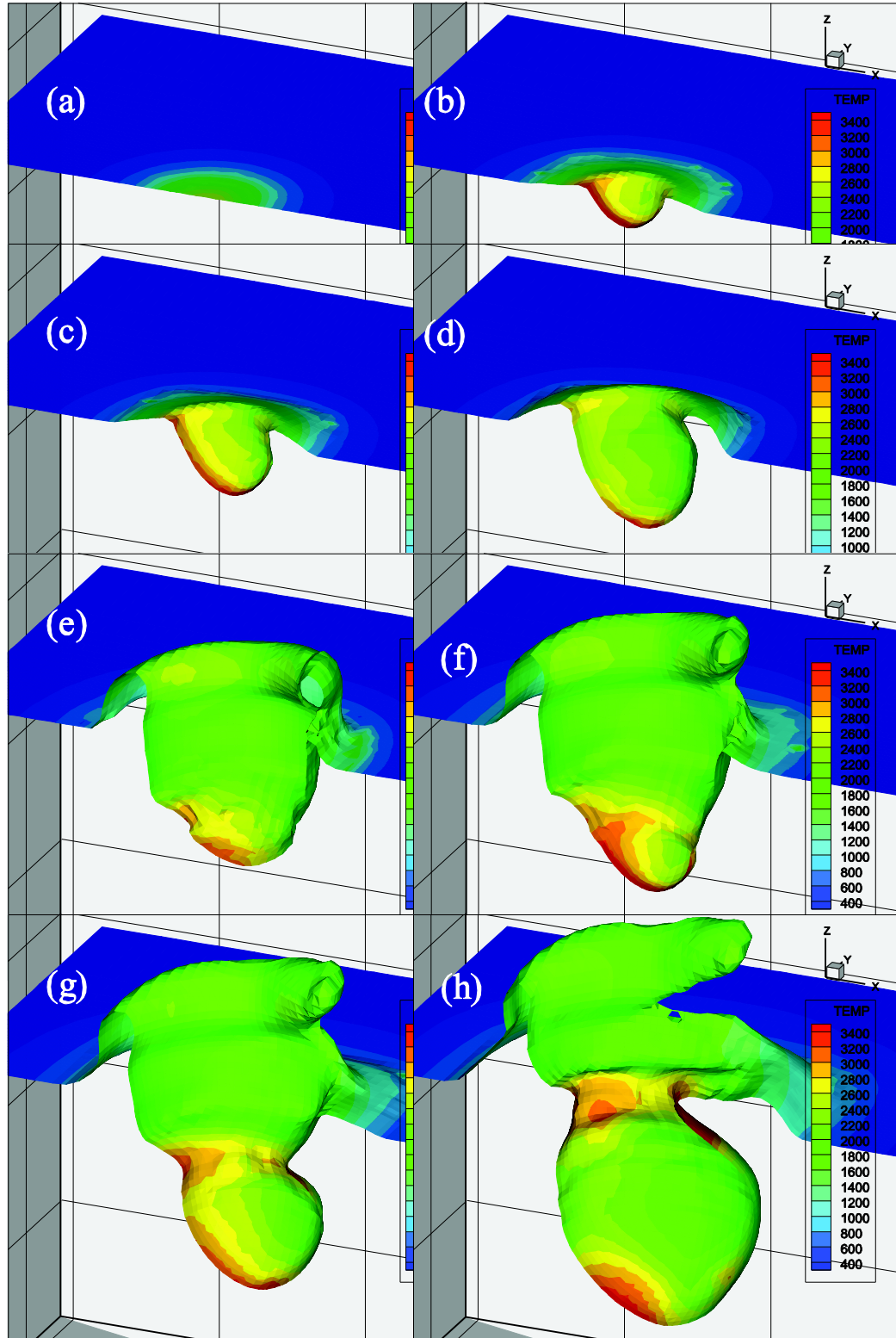
Figure 4.9.Temperature distribution and L/V interface geometry of aluminium (Laser power : 150W, Scanning speed : 3000 mm/s) at (a) 0.064 μs, (b)0.157 μs, (c)0.172 μs, (d)0.190 μs, (e)0.253 μs, (f)0.294 μs, (g)0.318 μs, (h)0.384 μs
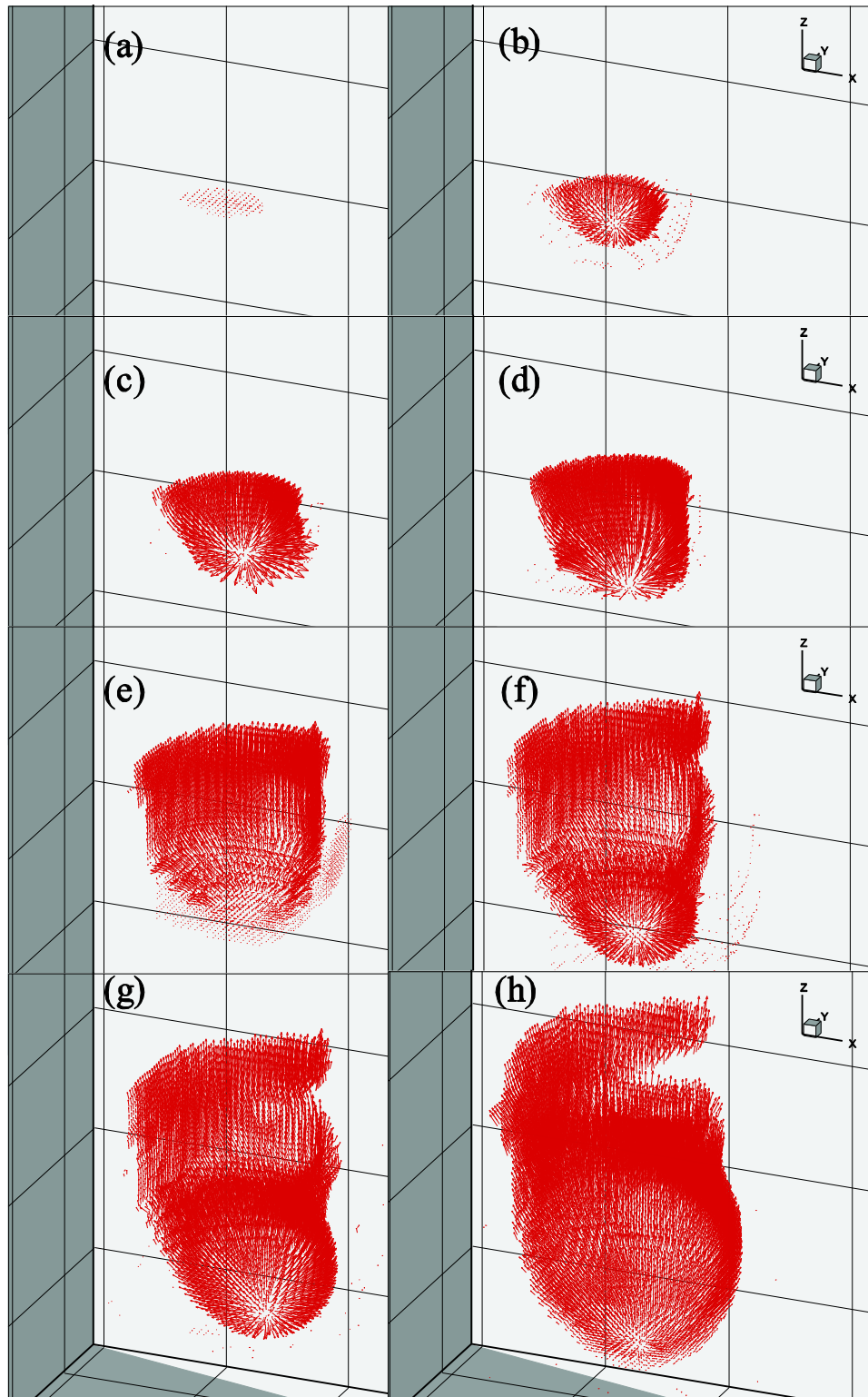
Figure 4.10. Melt pool flow of aluminum (Laser power : 150W, Scanning speed : 3000 mm/s) at (a) 0.064 μs, (b)0.157 μs, (c)0.172 μs, (d)0.190 μs, (e)0.253 μs, (f)0.294 μs, (g)0.318 μs, (h)0.384 μs

(e), which clearly corresponds to the region where the penetration depth and width stays the same as shown in Figure 4.6 (a) and (b). An initiation of a second deep penetration hole is shown in Figure 4.9 (f), and this second deep penetration hole creates a neck, shown in Figure 4.9 (g). The existence of the neck may form defects such as voids. The mechanism of deep penetration hole collapse is well explained in Lee *et al.*[39] and Kaplan *et al.* [40]. This neck formation almost closes the deep penetration hole and the laser beam is irradiated on the neck so that the temperature of the neck increases and is shown in Figure 4.9 (h). In addition, Figure 4.9 (h) also shows a spatter formation. When the crest meets the outer L/V interface, these two interfaces merge. After the interfaces merge, the crest separates from the body, since momentum of liquid aluminum moves its body outward and surface tension shrinks its surface.

Figure 4.10 shows melt pool flow. As seen in Figure 4.10 (b)-(e), strong outward flow patterns near the penetration hole are similar to the laser cutting of copper. However, the existence of the second deep penetration hole gives rise to the different flow pattern around the neck. There is strong melt pool flow at the tip of the second deep penetration hole. This strong flow meets the flow already developed by forming the first deep penetration hole and creates the neck. Since these two flows have the same direction, the flow near the neck shows the strongest flow, compared to the rest of the melt pool.

The simulation analysis in this study found that strong outward liquid flow and its momentum form the crest. In addition, even stronger flow through the formation of two deep penetration holes creates the spatter. These findings can be related to lithium-ion battery performance through the quality of cut surface. These crest and spatter result in

the surface deformation of melt pool. This surface deformation may give rise to composition change and sharp edge formation on the cut surface if there is an active electrode material on the top of the current collector. This composition change makes electrodes susceptible to higher electrical stress, which can lead to significant heat generation and possible thermal runaway during the electrochemical reaction in the lithium-ion battery cell. Furthermore, the sharp edge could penetrate a separator so that internal short circuit occurs.

4.3. Conclusions

The thresholds for the laser cutting as well as penetration time and depth have been investigated. For copper, laser power between 250W and 300W is the threshold for 5000 mm/s scanning speed. Laser power between 200W and 250W is the threshold for both 3000 mm/s and 1000 mm/s scanning speeds. For aluminum, laser power between 100W and 150W is the threshold for 5000, 3000, and 1000 mm/s. Given the presented results, we could conclude that the copper laser cutting is a laser intensity and interaction time dependent process. The aluminum laser cutting depends more on laser intensity than interaction time.

In addition, the effects of physical characteristics on surface quality near the threshold of the laser cutting of current collectors are studied. The penetration time of aluminum is 10.94 times faster than that of copper, even with a thicker substrate, less value of conductivity, and less laser power. The absorptivity of copper and aluminum increases 170% and 306.65%, respectively, compared to the absorption coefficients as

flat surfaces. The penetration depth and width of copper increase along two different slopes (8.207 m/s and 1.208 m/s), due to the transition from partial to full penetration laser cutting and crest formation. Aluminum increases both its penetration depth and width relatively smoothly, except during a certain time span. At this time span, the crest starts to form above the top of the substrate, due to the strong upward fluid flow and its momentum.

The three-dimensional geometry, temperature distribution, and melt pool flow during the laser cutting of copper and aluminum are observed and related with the penetration time, depth, width and absorptivity of each material. Near the penetration hole, both materials show the outward flow pattern. Furthermore, due to the momentum of the liquid melt pool, crests are created for both materials. With deeper penetration holes observed, the flow speeds are faster and the crests are higher. These conditions provide the possibility of forming a spatter or a recast layer. For the laser cutting of aluminum, not only the crest but also two consecutive deep penetration holes form. These two consecutive holes give rise to a neck and stronger flow speed around the neck. The mechanism of the spatter formation is explained with the merger and shrinkage of the L/V interface.

These undesirable defects, formed by spatter or reattachment, during the laser cutting of current collectors can be prevented by controlling the magnitude of melt pool flow through carefully chosen laser parameters. This finding will be utilized as critical information to obtain desired cut surfaces of electrodes. Furthermore, understanding the characteristics of copper and aluminum will be essential knowledge for the investigation of the behaviors of electrodes for lithium-ion batteries.

CHAPTER V

LASER CUTTING OF ELECTRODES

CW Gaussian laser beam is used and scanned in the positive x direction. A focused beam diameter is 11 μm. It is assumed that the beam profile has no z dependency. The laser power and scanning speed chosen for anode are 450W and 5000 mm/s, respectively. The laser power and scanning speed chosen for cathode are 150W and 5000 mm/s, respectively. The computational domain of the simulation is 55μm x 30μm x 130μm. The smallest discrete mesh distance is chosen as 0.6μm. One side graphite-coated copper and $LiCoO_2$–coated aluminum are chosen as the substrate material, where the thicknesses of the anode and cathode are 100 μm. Graphite of 90 μm and copper of 10μm are placed as the top and bottom layers of the anode, respectively. $LiCoO_2$ of 85μm is used as the top layer and aluminum of 15μm is used as the bottom layer. The properties of copper and graphite are shown in Table 4.1 and Table 5.1, respectively. The material properties of $LiCoO_2$ are barely available. Available material properties such as the melting temperature, solid thermal diffusivity, and solid density are used directly [8]. However, unavailable material properties are obtained by the law of fraction and the material properties of $LiCoO_2$ are shown in Table 5.5. The material

properties of Lithium, Cobalt, and Oxygen are shown in Table 5.2, Table 5.3, and Table 5.4, respectively.
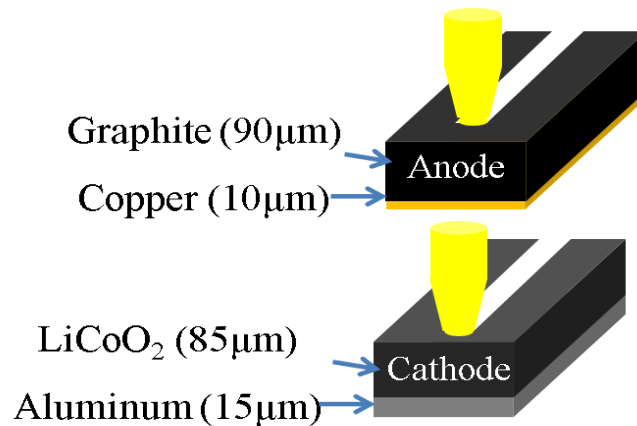
Figure 5.1. Electrodes used for simulations and experiments

5.1. Anode

5.1.1. Characteristics of the anode laser cutting

In the following sections, the top layer (90 μm) is called the graphite region; the bottom layer (10 μm) is called the copper region. Penetration depth, width, and absorptivity with evolution of time are shown in Figure 5.2. A deep penetration hole reaches a material interface between graphite and copper at 0.1646 μs. Around this material interface, several interesting overall behaviors are observed. The slope of the depth increase of the deep penetration hole changes over time. Before the deep penetration hole reaches the material interface, its slope of the depth increase is 722.16 m/s. Once the depth of the deep penetration hole reaches the material interface, the slope decreases to 288.00 m/s. The width increases gradually and it becomes 31.196 μm when the deep penetration hole reaches the material interface. This gradual increase of width is possible since the width is measured on the top surface of the anode. At the beginning of

109

the simulation, the absorptivity is 0.81, which is the absorption coefficient of graphite as a flat substrate. This absorptivity increases almost immediately to its maximum value within 0.1μs. The maximum absorptivity is 0.9588 at which point the deep penetration hole reaches the material interface. After obtaining the maximum value at 0.1646μs, absorptivity starts to decrease gradually with fluctuation and then it increases again before it has completed thorough cutting.

Table 5.1. Material properties of Graphite

Property	value
Sublimation temperature (T_b)	4800 (K)[99]
Critical point temperature (T_{cr})	7811 (K) [100]
Solid density (ρ_s)	1730 (Kg/m^3)[101]
Latent heat of sublimation (L_v)	5.98E+07 (J/kg) [101]
Solid thermal conductivity (k_s)	18.1 (W/mK) [101]
Solid constant-pressure specific heat (C_{ps})	2092.48 (J/kgK) [101]
Solid thermal diffusivity (α_s)	5.00E-06 (m^2/s) [101]
Laser absorptivity for flat surface (A_o)	0.81

Table 5.2. Material properties of Lithium

Property	value
Melting temperature	453.85 (K)
Normal boiling temperature	1609.15 (K)
Critical point temperature	3223 (K)
Liquid density	512.5 (Kg/m^3)
Solid density	533.4 (Kg/m^3)
Kinematic viscosity	1.002E+02 (m^2/s) [102]
Surface tension	0.306 (N/m)
Latent heat of vaporization	2.273E+07 (J/kg)
Latent heat of fusion	4.339E+05 (J/kg)
Liquid thermal conductivity	42.332 (W/mK)
Solid thermal conductivity	44.000 (W/mK)
Liquid constant-pressure specific heat	4225.8 (J/kgK)
Solid constant-pressure specific heat	3514.6 (J/kgK)
Liquid thermal diffusivity	1.954E-05 (m^2/s)
Solid thermal diffusivity	2.347E-05 (m^2/s)
Laser absorptivity for flat surface	0.015
Atomic weight	6.941 (g/mol)

Table 5.3. Material properties of Cobalt

Property	value
Melting temperature	1768.15 (K)
Normal boiling temperature	3173.15 (K)
Critical point temperature	6000 (K)
Liquid density	7750 (Kg/m^3)
Solid density	8832 (Kg/m^3)
Kinematic viscosity	5.000E-07 (m^2/s) [103]
Surface tension	1.698 (N/m) [104]
Latent heat of vaporization	7.209E+06 (J/kg)
Latent heat of fusion	2.920E+05 (J/kg)
Liquid thermal conductivity	30.404 (W/mK) [105]
Solid thermal conductivity	69.040 (W/mK)
Liquid constant-pressure specific heat	654.894 (J/kgK)
Solid constant-pressure specific heat	414.000 (J/kgK) [106]
Liquid thermal diffusivity	5.990E-06 (m^2/s)
Solid thermal diffusivity	1.888E-05 (m^2/s)
Laser absorptivity for flat surface	0.0085
Atomic weight	58.9332 (g/mol)

Table 5.4. Material properties of Oxygen

Property	value
Melting temperature	54.36 (K)
Normal boiling temperature	90.20 (K)
Critical point temperature	154.59 (K)
Liquid density	1141 (Kg/m^3)
Solid density	1535 (Kg/m^3)
Kinematic viscosity	2.366E-06 (m^2/s) [107, 108]
Surface tension	0.0178 (N/m) [109]
Latent heat of vaporization	2.131E+05 (J/kg)
Latent heat of fusion	1.388E+04 (J/kg)
Liquid thermal conductivity	0.1999 (W/mK) [110]
Solid thermal conductivity	5.8200 (W/mK)
Liquid constant-pressure specific heat	1675.062 (J/kgK) [111]
Solid constant-pressure specific heat	125.0046 (J/kgK)
Liquid thermal diffusivity	1.046E-07 (m^2/s)
Solid thermal diffusivity	3.033E-05 (m^2/s)
Laser absorptivity for flat surface	0.487
Atomic weight	31.9988 (g/mol)

Table 5.5. Material properties of LiCoO$_2$

Property	value
Melting temperature	1130 (K) [112]
Normal boiling temperature	2054.29 (K)
Critical point temperature	3891.95 (K)
Liquid density	5076 (Kg/m^3)
Solid density	4900 (Kg/m^3)
Kinematic viscosity	1.12E-06 (m^2/s)
Surface tension	1.050 (N/m)
Latent heat of vaporization	6.022E+06 (J/kg)
Latent heat of fusion	2.111E+05 (J/kg)
Liquid thermal conductivity	21.4 (W/mK)
Solid thermal conductivity	46.6 (W/mK)
Liquid constant-pressure specific heat	1241.67 (J/kgK)
Solid constant-pressure specific heat	539.40 (J/kgK)
Liquid thermal diffusivity	5.02734E-06 (m^2/s)
Solid thermal diffusivity	2.29504E-05 (m^2/s)
Laser absorptivity for flat surface	0.17

Characteristics of penetration depth and absorptivity change significantly at the point where the deep penetration hole reaches the material interface. These observations are closely related to each other and due mainly to the composition change at the material interface. An absorption coefficient changes its value depending on the mass fraction on the surface, since the absorption coefficient is obtained by a summation of the two absorption coefficients of the graphite and copper with mass fractions as described in Eqn. (2.58). Increasing the copper concentration around the material interface contributes to decreasing the absorption coefficient of the mushy zone so that absorptivity decreases. The decrease of absorptivity provides less energy absorption on the L/V interface. Therefore, the rate of depth increase changes. After the deep penetration hole reaches the material interface, it takes less than 0.05μs to have the full penetration of copper. However, it takes 0.3762 μs to have the full penetration during the laser cutting of

copper, as seen in Table 4.4. Since graphite absorbs 95.88% of the laser energy and has the relatively high value of conductivity, the absorbed heat energy can be transferred to the copper region with relatively faster speed. This heat energy may preheat the copper and expedite the evaporation process of copper. Therefore, the existence of graphite increases the penetration time of copper.
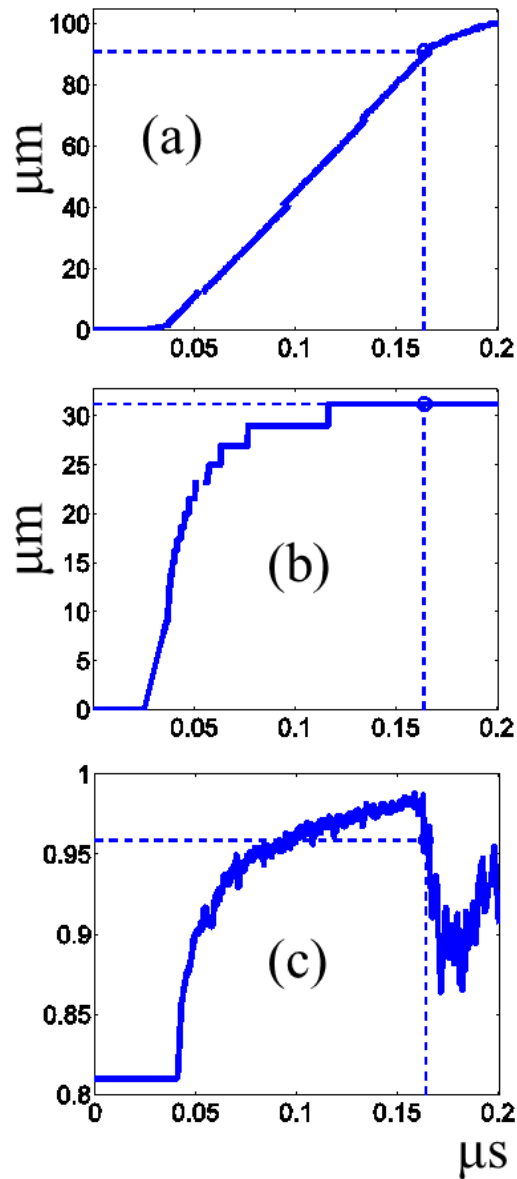
Figure 5.2. Penetration (a) depth, (b) width, and (c) absorptivity with time
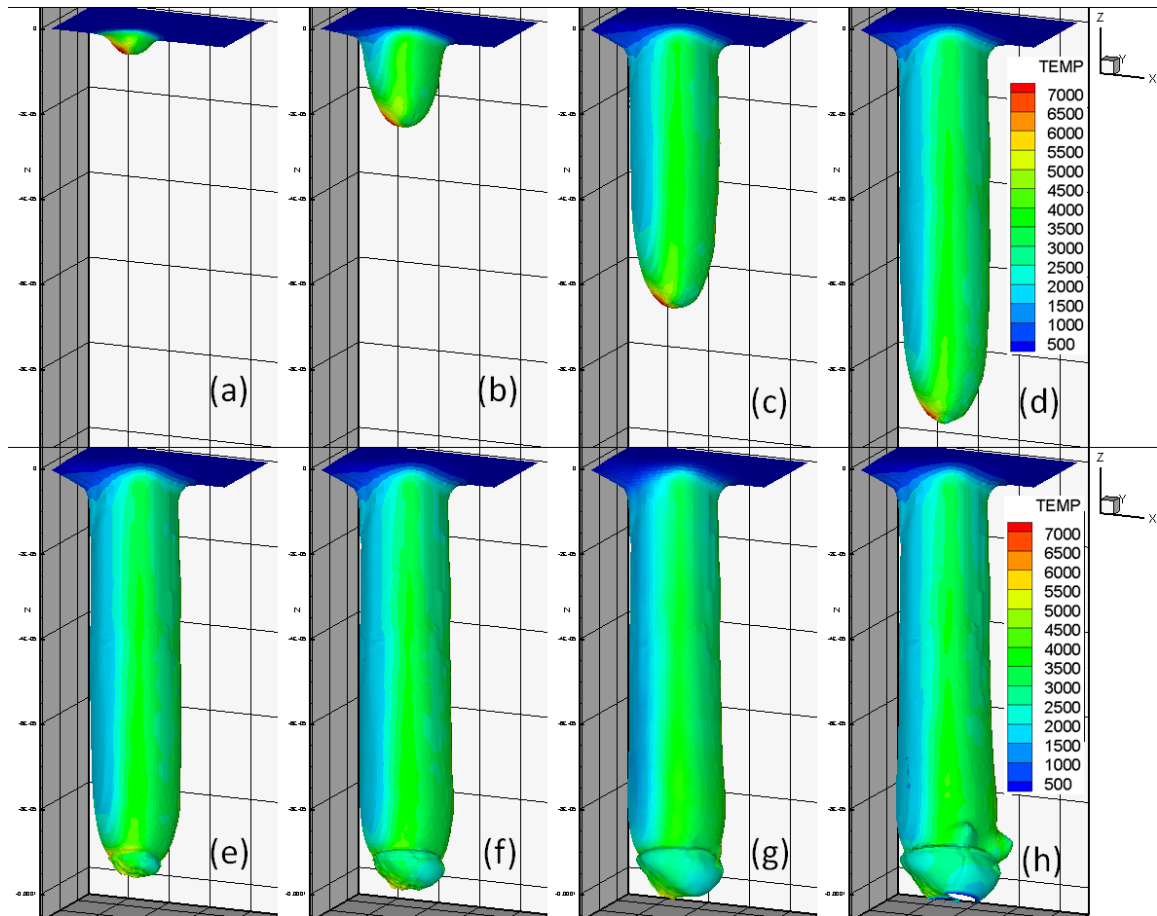
Figure 5.3.Temperature distribution and L/V interface geometry of anode (Laser power : 450W, Scanning speed : 5000 mm/s) at (a) 0.043μs, (b) 0.066μs, (c) 0.126μs, (d) 0.164μs, (e) 0.172μs, (f) 0.183μs, (g) 0.192μs, (h) 0.200μs

5.1.2. Temperature distribution and L/V interface geometry

Temperature distribution and L/V interface geometry are shown in Figure 5.3. At the beginning of the simulation, the deep penetration hole shows a very smooth and clean surface as seen in Figure 5.3 (a) – (c). The surface shows clearly the characteristic of the laser cutting of graphite, which was investigated in the study of laser cutting on an active electrode material [113]. No liquid phase exists for graphite since it sublimates. Hence, the resulting surface is smooth and clean. In addition, high temperatures are observed in

the front and back side of the L/V interface due to multiple reflections. When the deep penetration hole reaches the material interface, a melt pool starts to form as seen in Figure 5.3 (d). After this initial melt pool formation, the melt pool develops and shows the two-level surface, or two-step-like shape, as shown in Figure 5.3 (g). Penetrations on the side and front of the deep penetration hole at the moment of full penetration are observed as shown in Figure 5.3 (h). This two-level surface can be explained by the different material properties between graphite and copper. While no surface changes in the graphite region due to its sublimation property, melt pool flow observed in the copper region changes the geometry of the bottom part of the deep penetration hole. The movement of the liquid copper causes the fluctuation motion of the deep penetration hole and creates an uneven melt pool shape in the copper region. This uneven shape reflects a laser beam toward the graphite region and graphite sublimates due to the absorption of reflected laser energy. Hence, the reflected laser beam forms the front and side penetrations as well as the two-level surface, and changes the L/V interface geometry dramatically around the material interface. From the study of the laser cutting of copper in the previous section, the laser cutting of copper shows crests. However, no crest is observed during the laser cutting of anode since the existence of graphite placed on the top of copper prevents liquid copper from flowing over the top surface of copper.
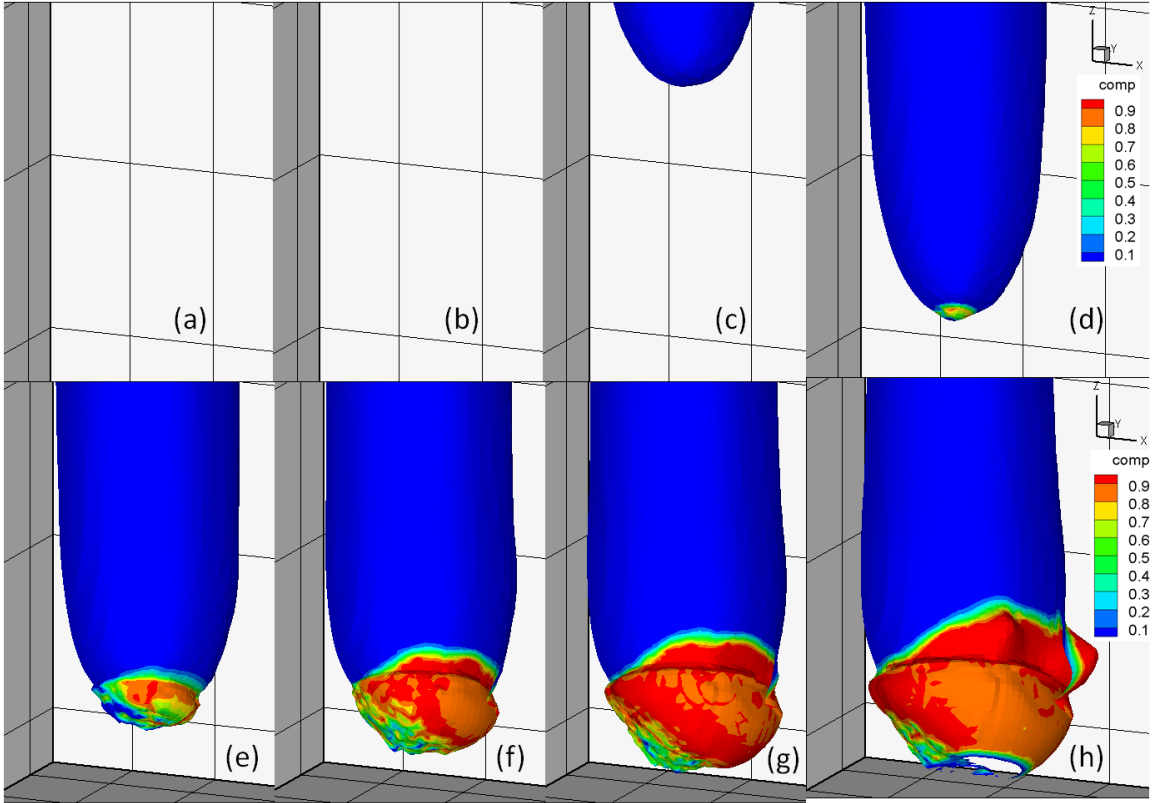
Figure 5.4. Copper composition distribution (Laser power : 450W, Scanning speed : 5000 mm/s) at (a) 0.043μs, (b) 0.066μs, (c) 0.126μs, (d) 0.164μs, (e) 0.172μs, (f) 0.183μs, (g) 0.192μs, (h) 0.200μs

5.1.3. Copper composition distribution and melt pool flow

Figure 5.4 and Figure 5.5 show copper composition distribution and melt pool flow, respectively. No copper composition and melt pool flow are shown in Figure 5.4 (a)-(c) and Figure 5.5 (a)-(c) since the deep penetration hole forms in the graphite region. When the deep penetration hole reaches the material interface, energy transfers from the graphite surface to the solid copper. The copper increases its temperature to the melting point so that the copper starts to melt and the melt pool forms. Next, the copper concentration starts to increase at the material interface, as seen in Figure 5.4 (d) and Figure 5.5 (d). At the beginning of the mass transfer, higher values of the copper concentration are observed on the front and side walls of the deep penetration hole as

116

shown in Figure 5.4 (e). In Figure 5.4 (f)-(h), as the deep penetration hole is becoming deeper, the copper concentration is distributed more uniformly on the copper region; copper concentration on the graphite region increases around the deformed graphite surface. However, the back side of the deep penetration hole in the copper region shows less copper concentration. The front melt pool provides stronger melt pool flow, as seen in Figure 5.5 (e) – (h). Furthermore, melt pool flow is observed on the graphite region due to the existence of the liquid copper. When a full penetration occurs, as shown in Figure 5.4 (h), the copper concentration is relatively low around the bottom of the penetrated hole. Stronger flow is observed around the deformed graphite surface, as shown in Figure 5.5 (h).
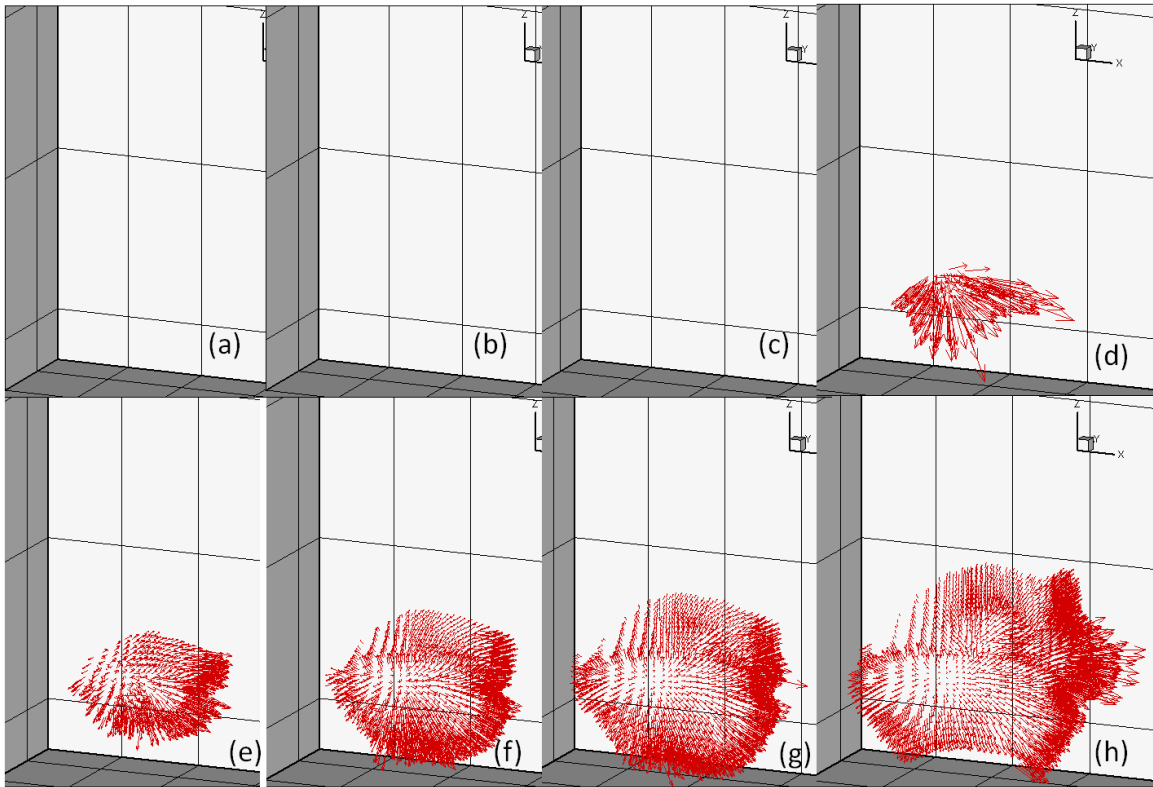

Figure 5.5. Melt pool flow of anode (Laser power : 450W, Scanning speed : 5000 mm/s) at (a) 0.043μs, (b) 0.066μs, (c) 0.126μs, (d) 0.164μs, (e) 0.172μs, (f) 0.183μs, (g) 0.192μs, (h) 0.200μs

5.2. Cathode

5.2.1. Characteristics of the cathode laser cutting

In the following sections, the top layer (85 μm) is referred to as the $LiCoO_2$ region; the bottom layer (15 μm) is referred to as the aluminium region. Penetration depth, width, and absorptivity with evolution of time are shown in Figure 5.6. A deep penetration hole reaches the material interface between $LiCoO_2$ and aluminium at 0.7207 μs and it takes 0.062 μs to achieve the full penetration. Several interesting overall behaviors are observed around the material interface.

First, the slope of the depth-increase of the deep penetration hole changes over time, as seen in Figure 5.6 (a). The slopes of the depth-increase both before and after the material interface are 125.32 m/s and 274.40 m/s, respectively. The reason for the slope change will be discussed along with the melt pool flow and geometry changes. Second, absorptivity drops suddenly, as seen in Figure 5.6 (c). At the beginning of the simulation, the absorptivity is 0.17, which is the absorption coefficient of $LiCoO_2$ as a flat substrate. The absorptivity reaches its maximum value, or 0.4637, at 0.3863 μs. Due to the liquid flow of $LiCoO_2$, absorptivity starts to fluctuate. Subsequently, at the material interface, the absorptivity drops significantly from 0.3753 to 0.2648, which is due to the aluminum composition change. The absorption coefficient is obtained by the linear summation of the two materials with the consideration of mass fraction. The absorption coefficient decreases, since aluminum has the absorption coefficient of 0.07. However, the value of absorptivity is still high compared to the absorption coefficient of aluminum due to the multiple reflections. The width is measured on the top surface and it increases gradually

until 28.71 μm, at which point the deep penetration hole has reached the material interface.
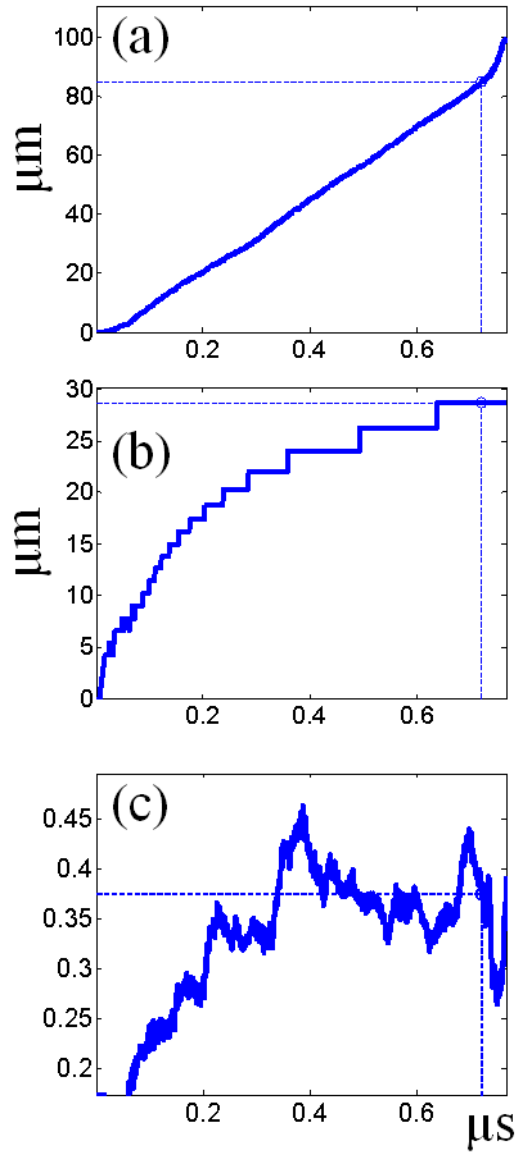
Figure 5.6. Penetration (a) depth, (b) width, and (c) absorptivity with time
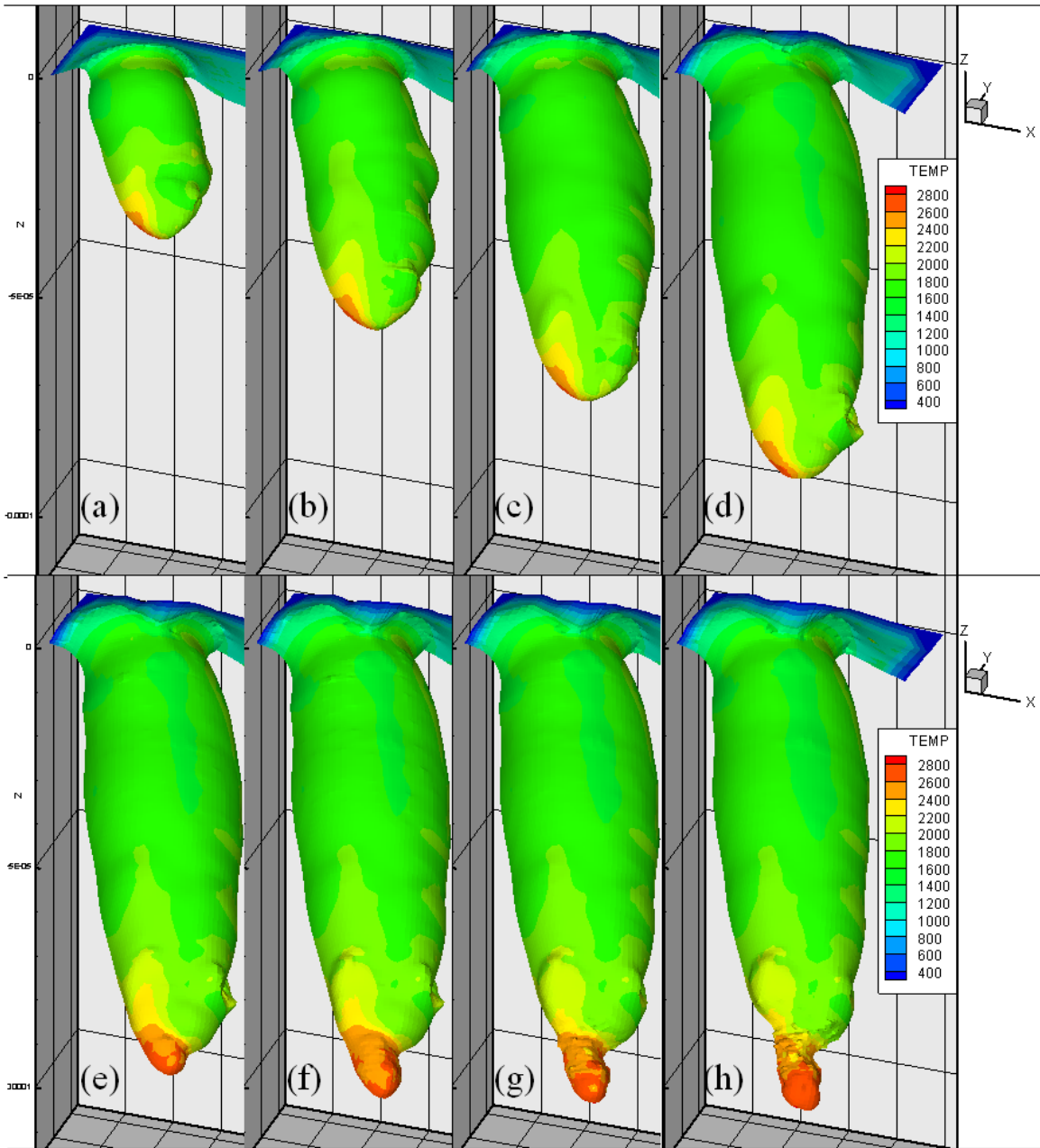
Figure 5.7. Temperature distribution and L/V interface geometry of cathode (Laser power : 150W, Scanning speed : 5000 mm/s) at (a) 0.308μs, (b) 0.464μs, (c) 0.595μs, (d) 0.732μs, (e) 0.751μs, (f) 0.760μs, (g) 0.763μs, (h) 0.768μs

5.2.2. Temperature distribution and L/V interface geometry

Temperature distribution on the liquid/vapor interface and L/V interface geometry are shown in Figure 5.7. At the beginning of the simulation, the deep penetration hole

shows an uneven surface and crests on the top surface as seen in Figure 5.7 (a) – (c), due to the liquid flow of $LiCoO_2$, which are seen in [36]. In Figure 5.7 (d), as the deep penetration hole deepens, uneven surfaces are observed near the tip of the deep penetration hole and relatively smoother melt pool surfaces are observed near the top surface. High energy concentrated on the tip of the deep penetration hole results in stronger flow due to evaporation. This stronger flow dissipates its momentum due to the viscous shear stress generated at the thin molten layer on the wall of the deep penetration hole. Moreover, if the flow momentum is insufficient to overcome the surface tension, the molten layer becomes thicker and surface tension subsequently changes the flow direction. Therefore, a protrusion can be formed in the front melt pool surface. This is seen in Figure 5.7 (d) as well as Figure 5.10. In addition, high temperatures are observed in the front and back sides of the L/V interface, due to multiple reflections.

When the deep penetration hole reaches the material interface, a narrower deep penetration hole forms in the aluminum region and temperature distribution is uniform inside the narrower deep penetration hole, as seen in Figure 5.7 (e)-(h). In this region, the smaller opening of the narrower deep penetration hole and the multiple reflections affect its temperature distribution significantly. In addition, since the opening of the narrower deep penetration hole is smaller than the beam diameter, the portion of the laser beam that did not reach inside the narrower deep penetration hole irradiates on the material interface of the $LiCoO_2$ region. This reflects to the side of the wall in $LiCoO_2$ region, and the geometry of the melt pool near the materials interface of the $LiCoO_2$ region subsequently deforms, as seen in Figure 5.7 (f)-(h).

121

Figure 5.8. Aluminum composition distribution (Laser power : 150W, Scanning speed : 5000 mm/s) at (a) 0.308μs, (b) 0.464μs, (c) 0.595μs, (d) 0.732μs, (e) 0.751μs, (f) 0.760μs, (g) 0.763μs, (h) 0.768μs
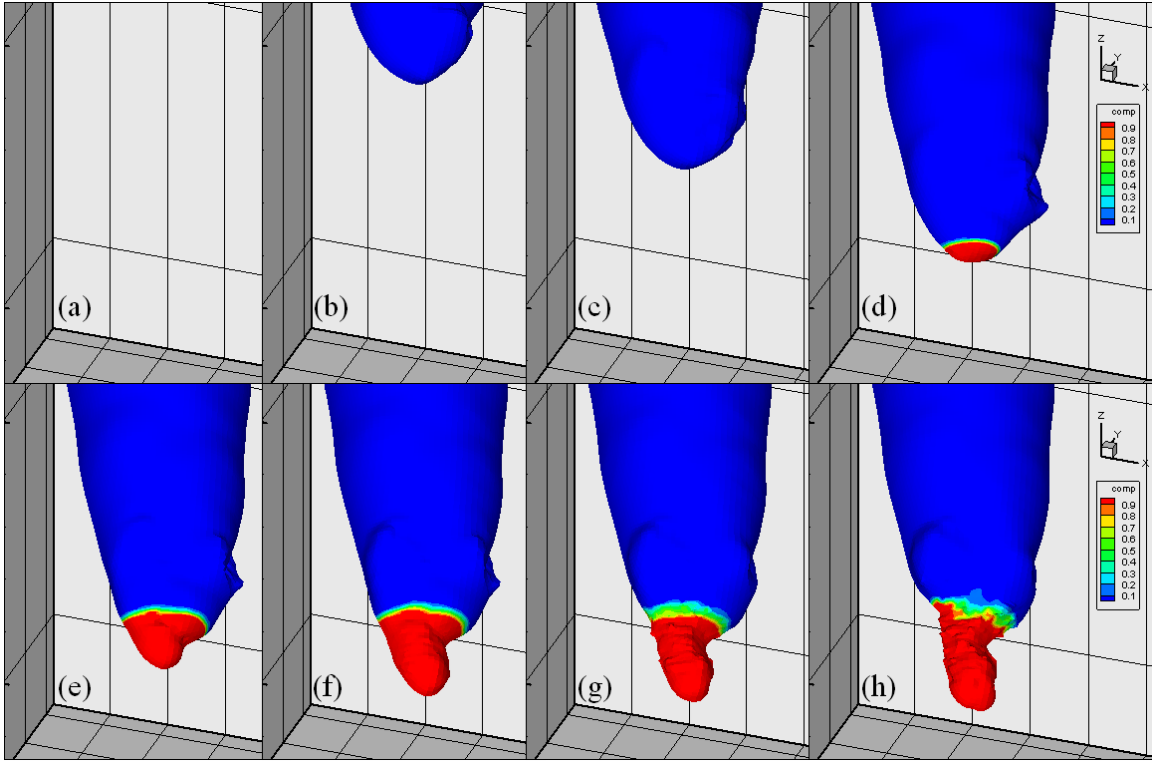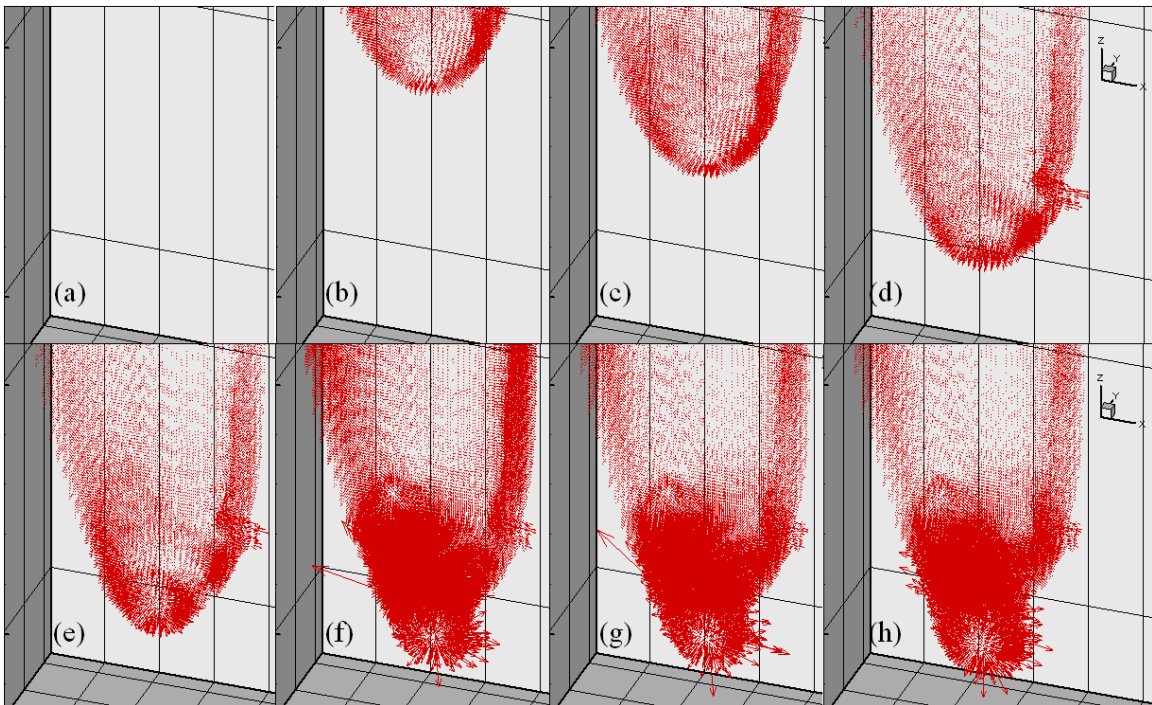

Figure 5.9. Melt pool flow of cathode (Laser power : 150W, Scanning speed : 5000 mm/s) at (a) 0.308μs, (b) 0.464μs, (c) 0.595μs, (d) 0.732μs, (e) 0.751μs, (f) 0.760μs, (g) 0.763μs, (h) 0.768μs

5.2.3. Aluminum composition distribution and melt pool flow

Figure 5.8 and Figure 5.9 show aluminum composition distribution on the L/V interface and melt pool flow, respectively. No aluminum composition is shown in Figure 5.8 (a)-(c), since the deep penetration hole forms in the $LiCoO_2$ region. Here, the melt pool flows outward from the tip of the deep penetration hole. As seen in many papers [33-35, 76], the front wall shows stronger flow, and liquid material is removed along the side wall of the deep penetration hole. Figure 5.10 shows the melt pool flow near the protrusion. As described in the previous section, the liquid material changes the flow direction and circulates along the protrusion. In addition, the dissipation of the flow momentum is clearly seen as the liquid moves upward.

When the deep penetration hole reaches the material interface, the aluminum increases its temperature to the melting point so that a high concentration of aluminum is observed in Figure 5.8 (d). After the initial formation of liquid aluminium, its concentration mostly remains high in the aluminum region. Although a variation in the aluminum composition can be observed near the material interface, this variation remains minor, as seen in Figure 5.8 (g)-(h). Both this phenomenon and the formation of the narrower deep penetration hole can be explained by the boiling points of the respective materials and the characteristic of melt pool flow. The boiling points of $LiCoO_2$ and aluminum are 2054K and 2792K, respectively. Since the tip of the deep penetration hole has the highest temperature, which is sufficient to evaporate aluminum as seen in Figure 5.7, a smaller area is evaporated within the aluminum region compared to the $LiCoO_2$ region. So, the differences of the boiling temperature of these materials can initiate the narrower deep penetration.

In addition to this smaller area of evaporation within the aluminum region, the melt pool flow plays a key role in the formation of the narrower deep penetration hole and aluminum composition variation. The melt pool flows in the Y-Z plane are shown in Figure 5.11. The liquid material from the $LiCoO_2$ region flows downward and the liquid material from the aluminum region flows upward along the wall of the solid material. These two flows meet near the material interface and merge. The merged flow moves toward the center of the deep penetration hole. This is well shown in Figure 5.11 (a). Due to the direction of the merged flow, the L/V interface also moves in the same direction as the merged flow. Therefore, the entrance of the deep penetration hole becomes smaller and the narrower deep penetration hole forms. As the narrower deep penetration becomes deeper, this phenomenon is shown again, as seen in Figure 5.11 (b)-(c). Therefore, while the conductivity of the aluminum is greater than that of $LiCoO_2$, the narrower deep penetration hole forms in the aluminum region due to both the difference of the boiling points and the melt pool flow patterns of $LiCoO_2$ and aluminum.
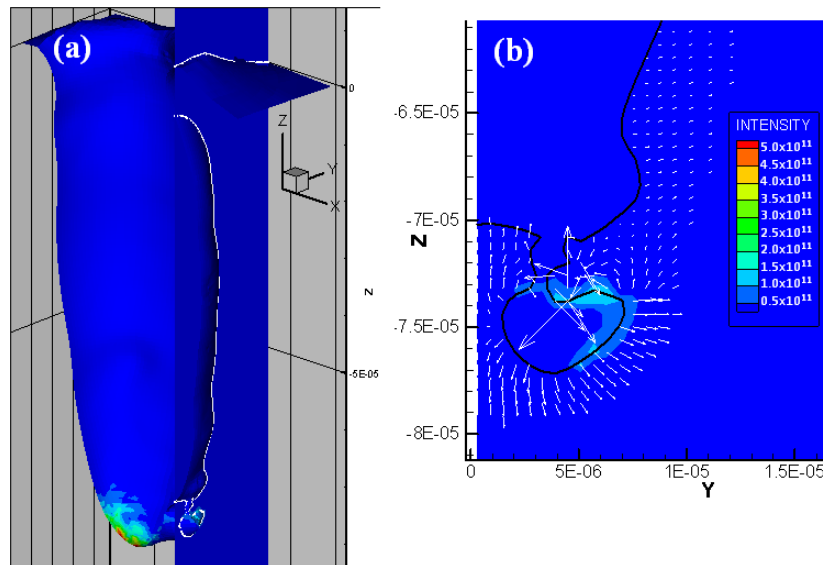
Figure 5.10. (a) Location of the YZ plane near the protrusion, (b) melt pool flow of cathode at 0.732μs (Laser power : 150W, Scanning speed : 5000 mm/s)
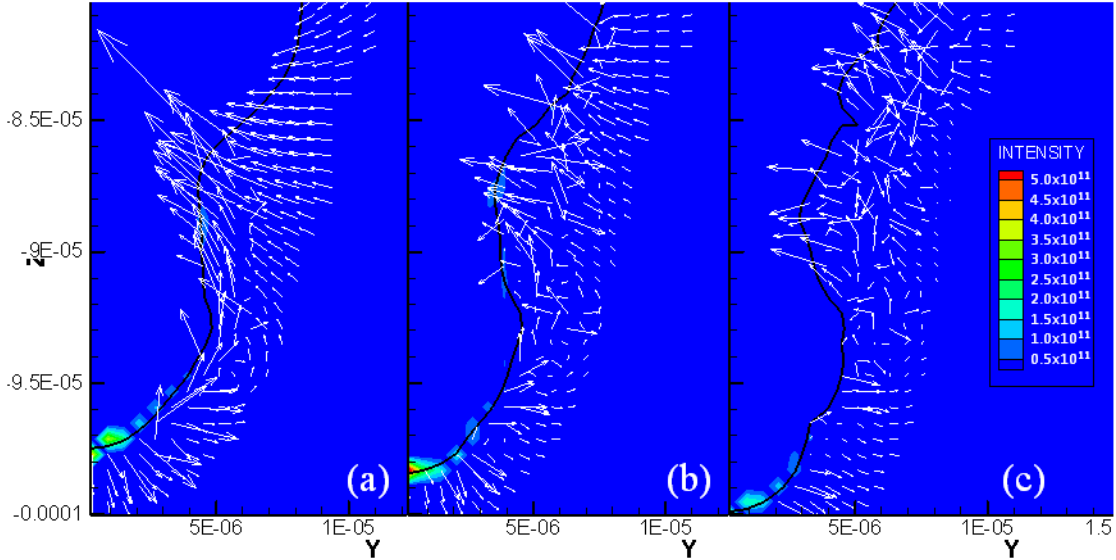
Figure 5.11. Intensity distribution and L/V interface geometry of cathode (Laser power : 150W, Scanning speed : 5000 mm/s) at (a) 0.760μs, (b) 0.763μs, (c) 0.768μs

5.3.   Conclusions

The analysis of simulation results present the characteristics of the laser cutting of anode and cathode for lithium-ion batteries. Characteristics of penetration depth and absorptivity change significantly at the point where the deep penetration hole reaches the material interface due mainly to the melt pool flow pattern, L/V interface geometry, material properties and the composition change at the material interface.

(a) The characteristics of the laser cutting of anode for lithium-ion batteries are examined at the beginning of the simulation.

Before the deep penetration reaches the material interface, the L/V interface shows a smooth and clean surface due to the sublimation characteristics of graphite. Furthermore, absorptivity increases almost immediately after the laser irradiation and

125

the top layer of the anode absorbs 95.88% of laser energy before the deep penetration hole reaches the material interface.

(b) When the deep penetration hole reaches the material interface of anode, interesting phenomena, such as two-level surface, liquid copper diffusion, and melt pool flows in the graphite region, are observed.

A melt pool starts to form, develops and results in a two-level surface due mainly to the sublimation property of graphite and the melt pool flow of liquid copper. In addition, higher values of the copper concentration, which are above 0.9, are observed around the material interface. When the deep penetration hole is becoming deeper, the copper concentration is distributed more uniformly and the front melt pool provides strong melt pool flow in the copper region. In the graphite region, the copper concentration increases around the deformed graphite surface and melt pool flow is observed due to the existence of the liquid copper. Penetrations on the side and front walls of the deep penetration hole at the moment of full penetration are observed since uneven melt pool shape in the copper region reflects the laser beam to the graphite region. The copper concentration is relatively low around the bottom of the penetrated hole. Stronger flow is observed around the deformed graphite surface.

(c) L/V interface geometry and melt pool flow are investigated for cathode at the beginning of the simulation

The deep penetration hole shows an uneven surface and creates crests on the top surface. In addition, as the deep penetration hole deepen, uneven surfaces are observed near the tip of the deep penetration hole and relatively smoother melt pool

surfaces are observed near the top surface due to stronger flow at the tip of the deep penetration hole and the dissipation of flow momentum due to viscous shear stress. During the laser cutting, a protrusion is formed in the $LiCoO_2$ region, since the flow momentum of the material is insufficient to overcome the surface tension and viscous shear stress.

(d) The melt pool flow pattern forming the narrower deep penetration hole and aluminum concentration distribution in the aluminum region are analyzed when the deep penetration hole reaches the material interface.

The formation of the narrower deep penetration hole is due to the differences of boiling temperatures between the two materials as well as a merged flow pattern that moves toward the center of the deep penetration hole. In addition, the merged flow pattern contributes to the aluminum composition change, which remains high in the aluminum region.

(e) The proposed mathematical model of the laser cutting of electrodes for lithium-ion batteries can be utilized to predict and prevent the defects or thermal stresses.

These defects and stresses can be predicted by analyzing the L/V interface geometry, melt pool flow pattern, composition change and temperature distribution through the proposed model. Therefore, the analysis of the proposed model can provide useful information to prevent these defects and stresses.

CHAPTER VI

EXPERIMENTAL VERIFICATION AND LASER PARAMETER OPTIMIZATION TO THE LASER CUTTING OF ELECTRODES

6.1. Experimental setup

The schematic of the remote laser cutting process is shown in Figure 6.1 and Figure 1.5 (a). An IPG single mode CW fiber laser working at 1070nm with the maximum output power of 500W is used as the laser source. The laser beam is fiber-delivered using a 10µm core-fiber diameter. A 2D galvo-scanner from Scanlab is used to deflect and move the laser beam at high dynamic speeds with maximum speeds up to 5000 mm/s. A 80mm F-theta objective mounted on the scanner keeps the scanning image field flat within a 37.5 X 37.5mm square field size. The measured spot size at the focus position is approximately 11µm with a small Rayleigh length of 70µm and M2 value (86%) of 1.3. The spot is symmetrical and has a closely Gaussian energy distribution and measured laser beam intensity distribution is shown in Figure 6.2. Given the small Rayleigh length, it is essential to hold the material flat on the fixture during the entire cutting process. A vacuum fixture is used to hold electrodes and prevent any movement during the cutting process. A narrow groove (< 1 mm) is machined in the top plate of the fixture right underneath where the cutting takes place to prevent any melt attachments

that come out of the cutting kerf. The fixture is mounted horizontally on two orthogonal axes of a CNC motion system while the scanner is mounted on its third vertical axis. This precise 3-axis positioning is required for the setup to align the fixture with the scanner and to position the scanner at the correct vertical distance from the electrode foil. There is no process gas applied during cutting since applying shielding gas provide no significant improvement in cut quality [114]. Cutting is performed in a clean and dust free environment with suitable fume exhaust systems. Materials used for the laser cutting are uncoated copper and aluminum foils for current collectors with a thickness of 10μm and 15μm, respectively. One-sided coating has been used for electrodes. Graphite-coated copper and $LiCoO_2$-coated aluminum are selected for anode and cathode, respectively. Active electrode materials are coated on the top of the current collectors. The total thickness of the anode and cathode are 100μm, with the graphite and $LiCoO_2$ being 90μm and 85μm thick, respectively. Electrodes are seen in Figure 5.1.

From the steady state keyhole welding model, "drilling" velocity can be defined with the penetration time and depth of the front wall [55, 115-117]. Due to the nature of the laser cutting, there is very fast "drilling" velocity compared to the scanning speed of the laser cutting. Hence, the kerf widths obtained at the initial and transient stages of the laser cutting are compared with the kerf widths of experimental samples. The shortcoming of this validation is that the final stage of the laser cutting simulation may have discrepancy since the final stage may be more affected by temperature and fluid flow pattern compared to the initial and transient stages, as discussed in the Chapter 3.
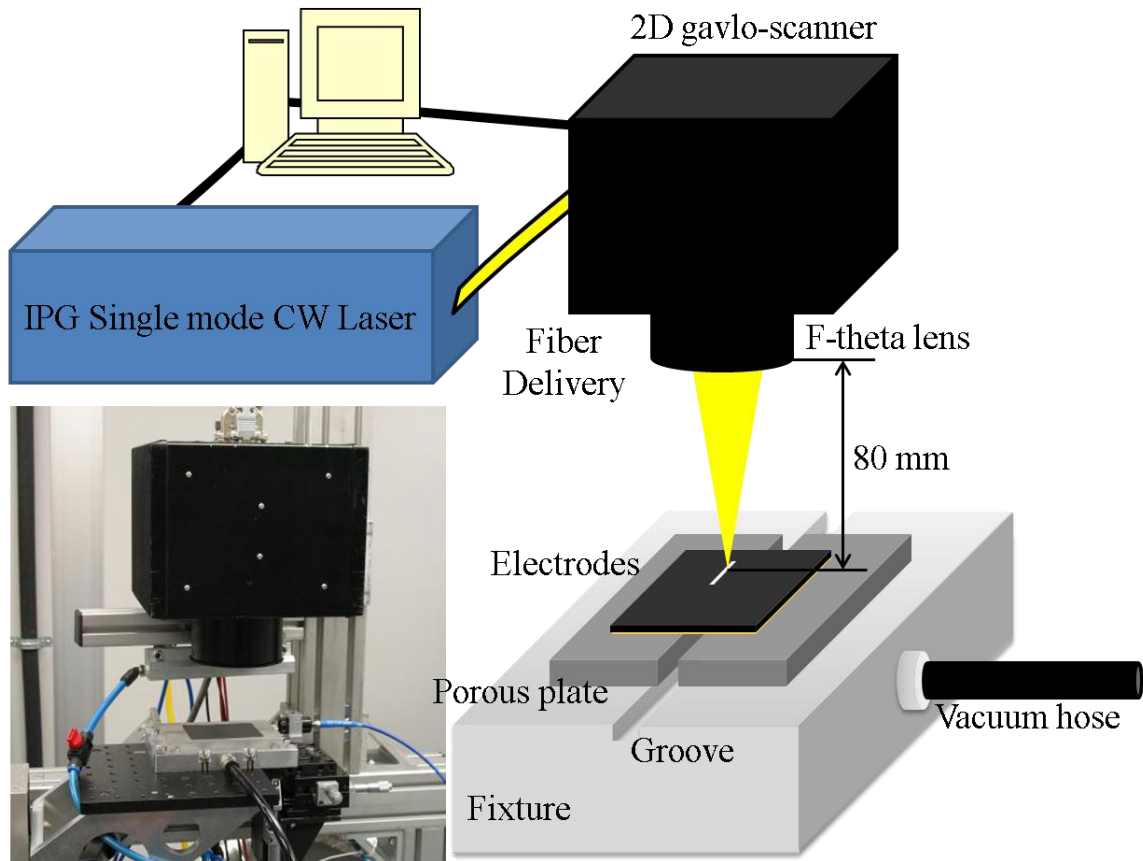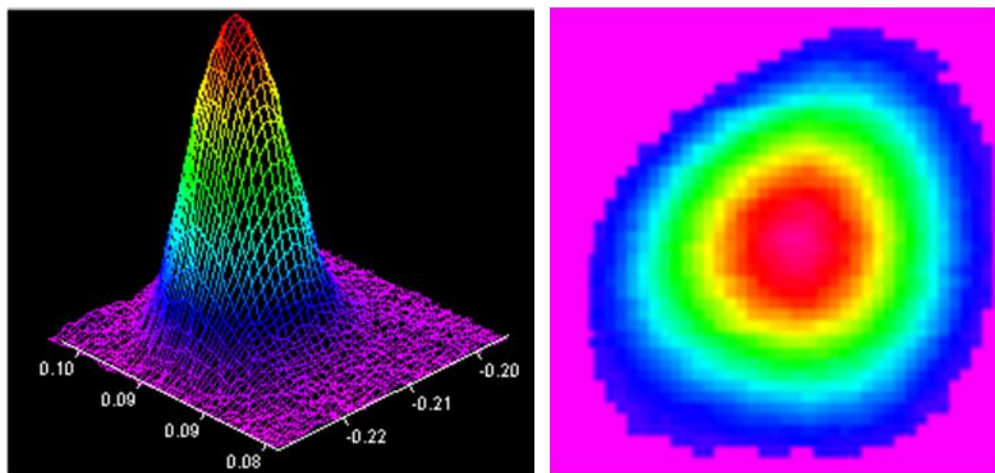
Figure 6.1. Experimental set-up

Figure 6.2. Measured laser beam intensity distribution

6.2. Experimental validation for current collectors

A series of linear laser cutting tests of the current collectors are performed for validation with combinations of the laser parameters, as shown in Table 4.3. Here the laser power is the calibrated power output on the workpiece and includes all the beam delivery losses. During all cutting tests, the focus of laser beam was positioned on the surface of the current collectors. The length of cut was fixed at 25 mm and only a single pass of laser beam was used for cutting. The start and stop regions of the cut length were not considered for analysis to avoid any effects of scanner acceleration and deceleration at high speeds. To ensure accuracy of test results, cutting tests were repeated. Among these experimental results, SEM analysis is done for the cases that have laser power and laser scanning speeds near to full penetration cutting thresholds. The threshold, which is highlighted area, and top view of the copper laser cuttings are shown in Figure 6.3, using a different combination of laser parameters. The kerf widths obtained from the aluminum laser cutting simulations are drawn with dashed lines on the top of SEM images. The kerf widths of the experimental and simulation results show a good agreement for the full penetration of high-speed cutting cases. Figure 6.3 (a) shows almost no cutting. The small area of full penetration is barely seen. Reattachments in the cut surface are shown in Figure 6.3 (c). A bubble-shape recast is observed with inconsistent kerf width in Figure 6.3 (e). This bubble-shape recast creates the bad cut surface of the electrodes so that battery performances could be deteriorated. On the other hand, Figure 6.3 (b) and Figure 6.3 (d) show clear cutting and consistent kerf width. Even though 250W and 1000 mm/s laser beam create the full penetration, bubble-shape recast is seen in Figure 6.3 (f).

Figure 6.3. Threshold and kerf width based on simulation results and experimental results of laser cutting on Copper - dashed line is the kerf width of the simulation (a) 250 W, 5000 mm/s; (b) 300 W, 5000 mm/s; (c) 200 W, 3000 mm/s; (d) 250 W, 3000 mm/s; (e) 200 W, 1000 mm/s; (f) 250 W, 1000 mm/s

Figure 6.4 shows the threshold, which is highlighted area, and top view of the laser cutting of aluminum. Dashed lines depict the kerf widths obtained from the simulation. The kerf widths of the experimental and simulation results show a good agreement for the full penetration cases. Figure 6.4 (a) shows reattachment at the cutting zone. These reattachments bridge the two separated foils. Depending on the size of this reattachment, some of them dissociate easily when merely touched. Similar phenomena could be observed in Figure 6.4 (c). Thus, we could treat these cases as the partial

penetration cutting. On the other hand, full penetration cutting is achieved in Figure 6.4 (b), (d), and (f), which are 150W laser power cases, as predicted by the simulation results. However, Figure 6.4 (e) shows full penetration cutting.
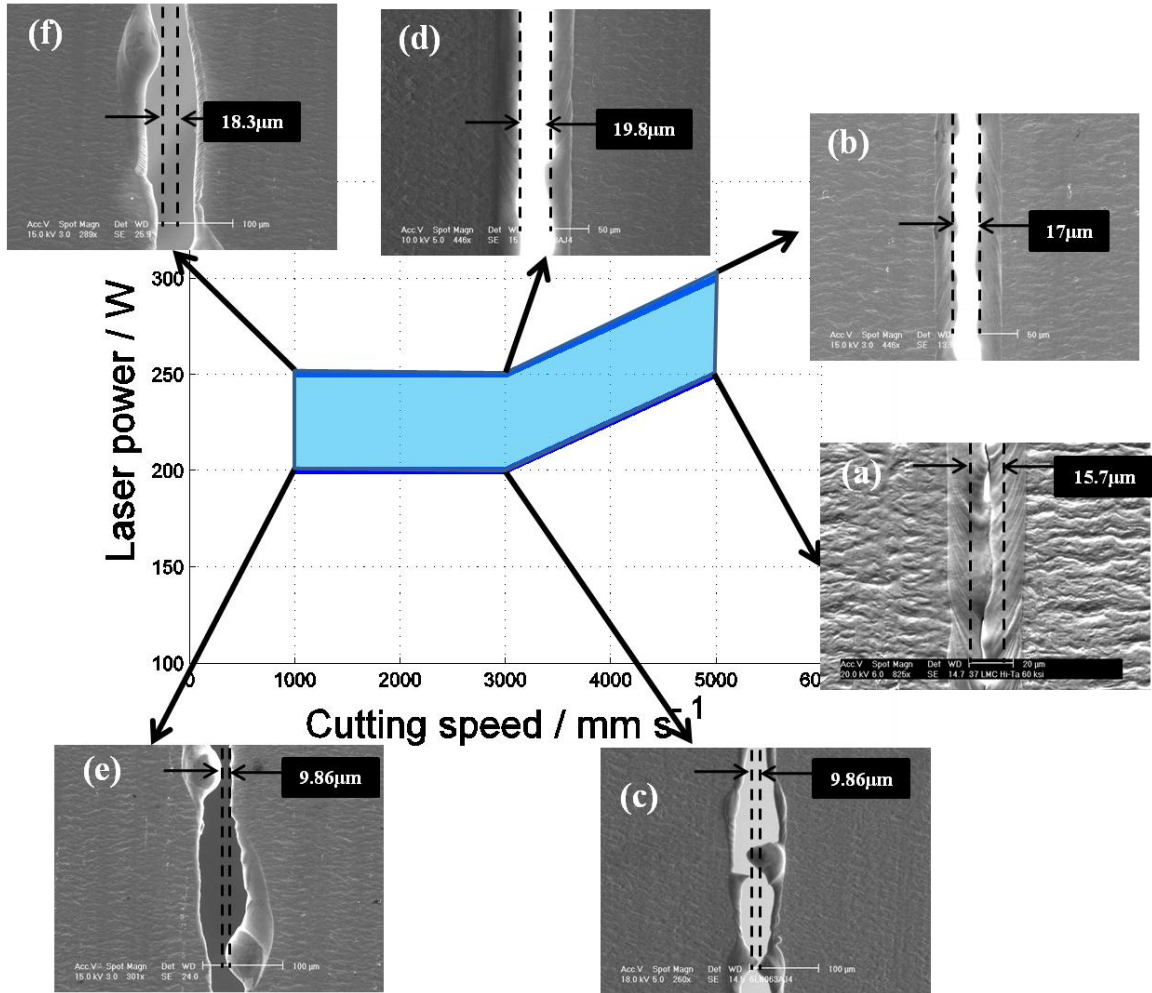

Figure 6.4. Threshold and kerf width based on simulation results and experimental results of laser cutting on Aluminum - dashed line is the kerf width of the simulation (a) 100 W, 5000 mm/s; (b) 150 W, 5000 mm/s; (c) 100 W, 3000 mm/s; (d) 150 W, 3000 mm/s; (e) 100 W, 1000 mm/s; (f) 150 W, 1000 mm/s

Therefore, simulation results match well with experimental studies for the high speed laser cutting, such as 5000 mm/s and 3000 mm/s, of the current collector materials. However, there is a discrepancy for the low speed cutting, such as 1000 mm/s. The

reason for this might be that the mathematical model used a constant absorption coefficient. Therefore, including a temperature dependent absorption coefficient might improve the mathematical model for low speed cutting.
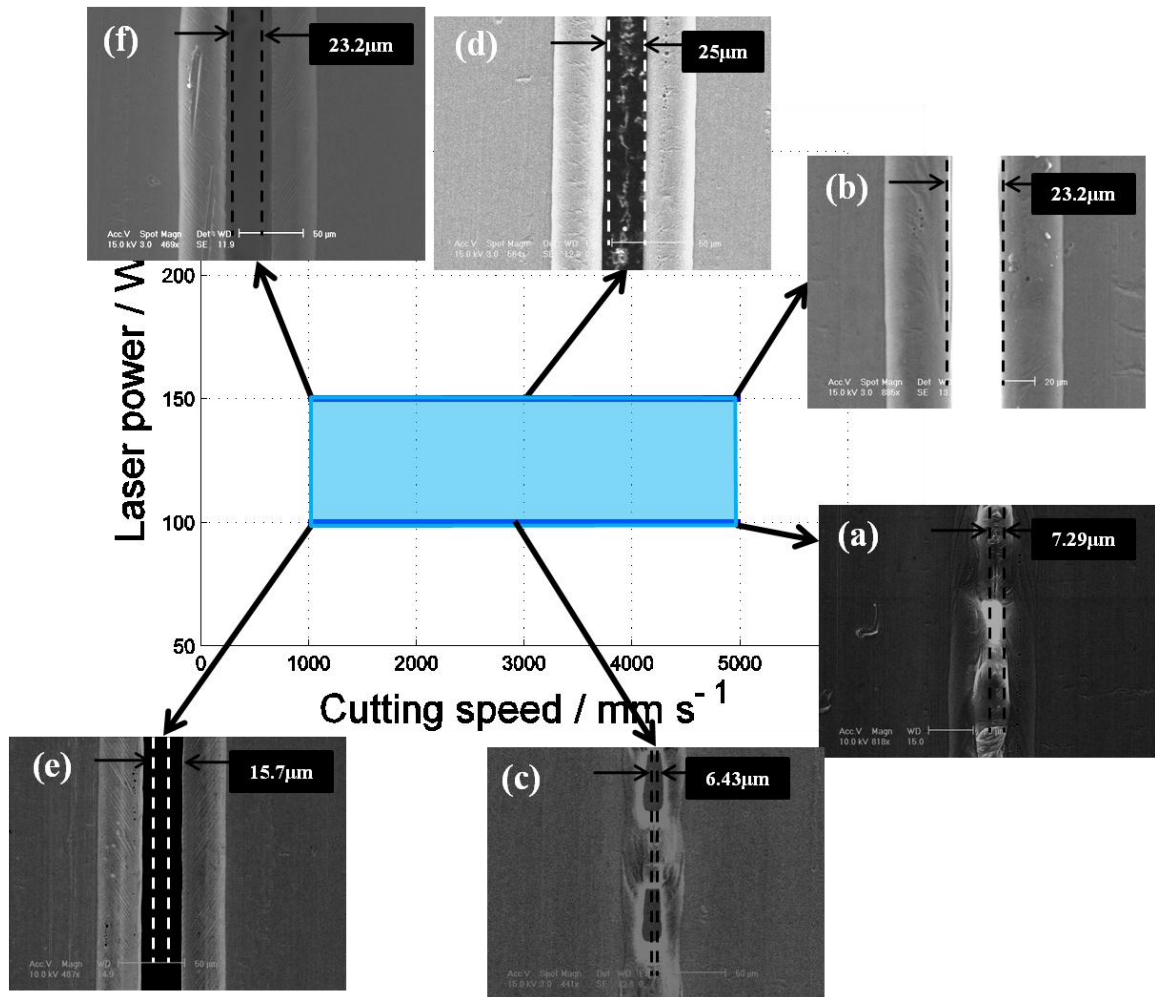

Figure 6.5. Threshold and kerf width based on simulation results and experimental results of laser cutting on Anode - dashed line is the kerf width of the simulation (a) 250 W, 5000 mm/s; (b) 300 W, 5000 mm/s; (c) 200 W, 3000 mm/s; (d) 250 W, 3000 mm/s; (e) 200 W, 1000 mm/s; (f) 250 W, 1000 mm/s

The kerf widths and thresholds of current collectors obtained by simulation are compared to the experimentally obtained results of current collectors in the presence of the active electrode materials to validate the proposed mathematical model in a more

realistic situation. The threshold of copper laser cutting and top view of the single side-coated anode laser cuttings are shown in Figure 6.5. Only graphite is sublimated in Figure 6.5 (a). Figure 6.5 (b) shows the partial cutting of copper. Thus, the laser power of 300 W provides not enough energy to obtain full penetration cutting with the 5000 mm/s scanning speed. With the 3000 mm/s scanning speed, simulation results match well with experimental studies as shown in Figure 6.5 (c) and (d). Although the kerf width of copper in Figure 6.5 (d) shows a good agreement, wider kerf widths are observed for graphite. Both Figure 6.5 (e) and (f) show full penetration cutting with 3.7 times wider kerf widths compared to simulation results. Figure 6.6 shows the thresholds of aluminium laser cutting and top view of the single side-coated cathode laser cuttings. No cutting is observed in Figure 6.6 (a). Regardless of laser scanning speeds, the laser power of 150W provides full penetration cutting as seen in Figure 6.6 (b), (d), and (f). This full penetration is predicted by the simulation results. Furthermore, the kerf widths of aluminum obtained experimentally and numerically are in good agreement, as shown in Figure 6.6 (b), (d), and (f). However, Figure 6.6 (c) and (e) show full penetration cutting and these are different to results estimated by simulation.
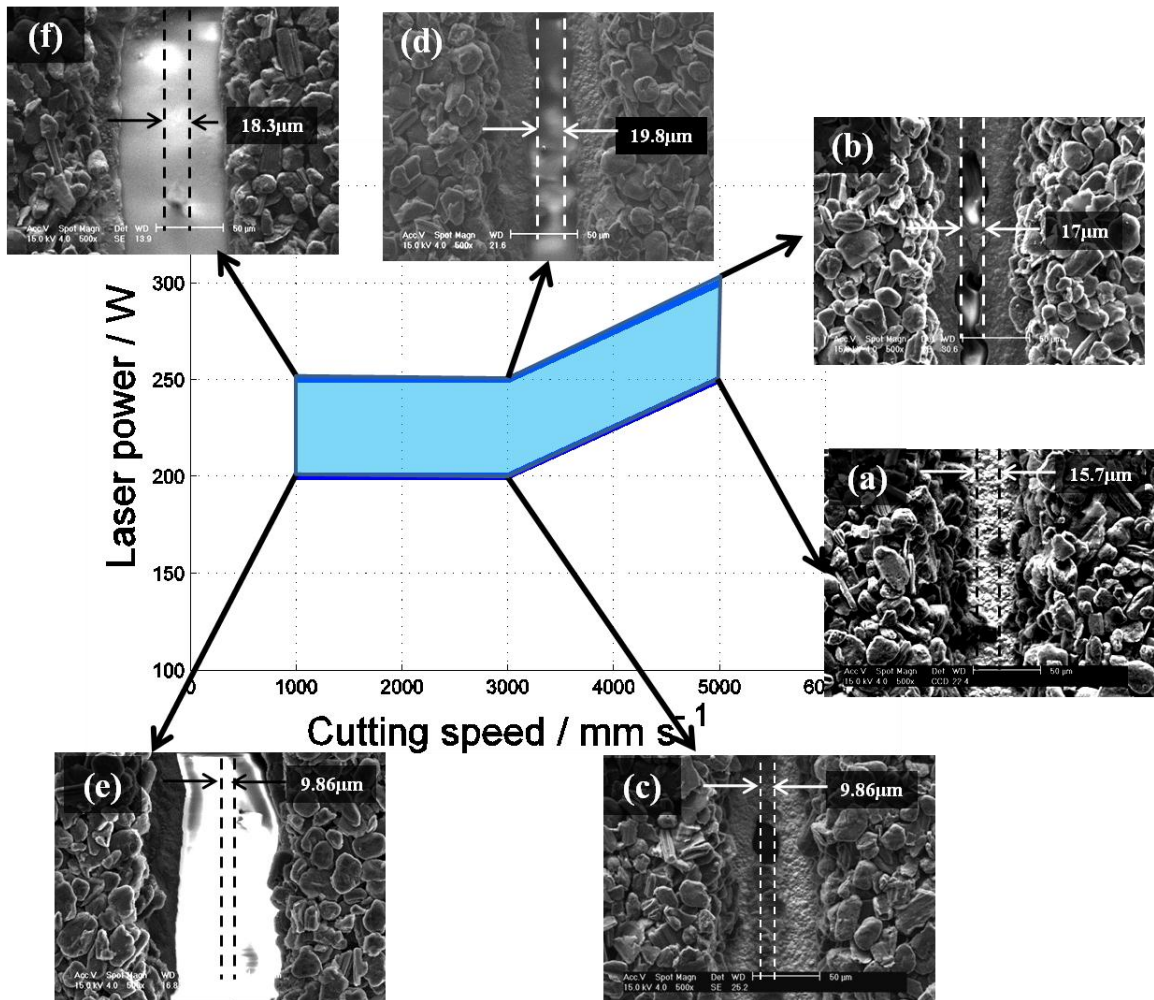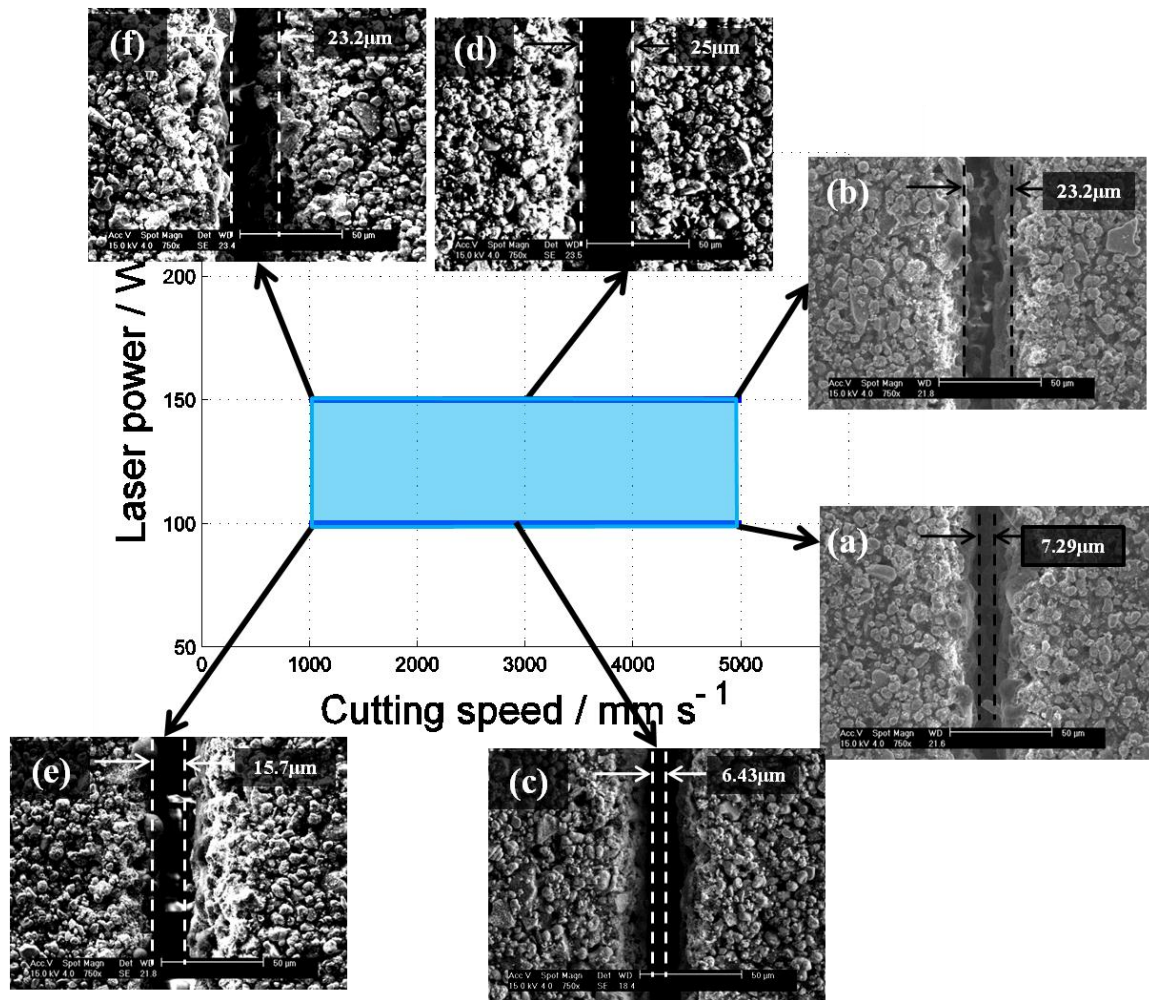
Figure 6.6. Threshold and kerf width based on simulation results and experimental results of laser cutting on Cathode - dashed line is the kerf width of the simulation (a) 100 W, 5000 mm/s; (b) 150 W, 5000 mm/s; (c) 100 W, 3000 mm/s; (d) 150 W, 3000 mm/s; (e) 100 W, 1000 mm/s; (f) 150 W, 1000 mm/s

Simulation and experimental results of copper with the single side-coated graphite are in good agreement in the case of the 3000 mm/s scanning speed. In addition, simulation results of aluminium with single side-coated $LiCoO_2$ match well with experimental studies in the case of 5000 mm/s. The other cases show discrepancies. These discrepancies can be caused by the different absorption coefficients between current collectors and active electrode materials. Furthermore, the sublimation characteristic of graphite might affect these discrepancies. Finally, the composition

136

variation of current collector materials between the interface of current collectors and active electrode materials may result in discrepancies between simulation and experimental results.

6.3. Experimental validation for electrodes

6.3.1. Anode

The single side-coated anode is used. The anode is placed on the fixture as graphite faces upward and the laser beam irradiates on the graphite surface. Thickness of graphite and copper are 90μm and 10μm, respectively. The laser power and scanning speed chosen are 450W and 5000 mm/s, respectively.

The top view of a laser cut anode is shown in Figure 6.7. Kerf widths on the top and bottom layers are 97.60 μm and 27.90 μm, respectively. Luetke *et al.* [27] defined the clearance width of the metal foil of anodes for lithium-ion batteries, which is the ablation width of the upper coating. This study also observes the clearance width of 29.10μm. These experimental results clearly show the two-level surface on the material interface, which is also observed in the simulation result. The kerf width obtained by simulation is 31.19μm and shown in Figure 6.7 with a dashed line. The simulation result overestimates the kerf width of the bottom layer by 7.18%, which is in good agreement with the experimental measurement. However, the kerf width of the top layer shows discrepancy compared to the kerf width obtained by the simulation. The discrepancy of the kerf width, which is characterized by the clearance width, can be explained by the computational

study in the section 5.1.2. The fluctuation motion of the deep penetration hole due to the liquid flow of copper creates uneven melt pool shape at the tip of the deep penetration hole. The reflected laser beam toward the graphite region from the uneven melt pool shape sublimates graphite. Hence, the kerf widths of the graphite region and copper region are different. The side view of the laser cut anode is shown in Figure 6.8. It shows good quality of cut surface. No delamination, edge banding, burrs, or micro-size attachments on the material interface are observed. At the bottom of the anode, debris caused by re-solidification is observed. Copper concentrations, which are obtained by both the simulation and experiment, are analyzed along the perpendicular line as shown in Figure 6.9 and its values are plotted in Figure 6.10. The copper concentration of the experimentally obtained anode sample was obtained through Energy-Dispersive X-ray spectroscopy (EDX) analysis.
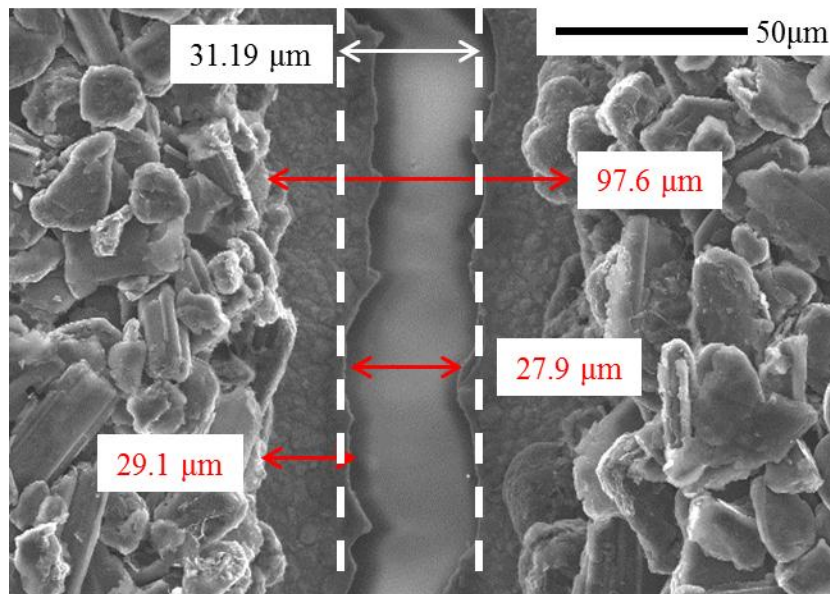

Figure 6.7. Top view of laser cut anode with the laser power of 450w, and scanning speed of 5000 mm/s
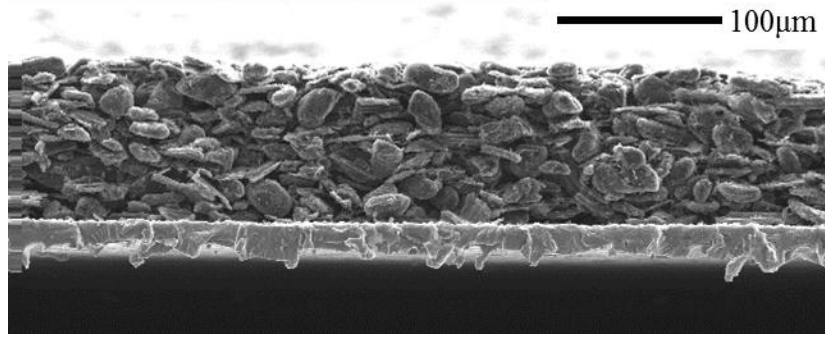
Figure 6.8. Side view of laser cut anode

From the top surface to the depth of 71.31 μm, the experimentally measured copper concentration is lower than 10% and shows no trend. The copper concentration increases significantly from the depth of 71.31μm to 82.55μm and reaches its value of 99.68% at the depth of 82.55μm. As it become deeper, the copper concentration gradually decreases from the 99.68% to 16.12%, from the depth of 82.55μm to the material interface, and then it increases again and becomes 100% copper concentration at the depth of 100μm. For the computationally obtained copper concentration, there is no copper concentration observed from the top surface to the depth of 73.96 μm. From the depth of 73.96μm to 74.56μm, a small amount of copper concentration is found. The copper concentration increases significantly and becomes 100% at the depth of 84.73μm. The copper concentration stays at 100% until at the depth of 89.52 μm and then decreases up to 78.02% at the depth of 99.10μm. Both experimentally and computationally obtained copper concentrations share three characteristics. First, the copper concentration starts to increase its value at least 10μm above the material interface. Second, it increases very sharply up to 100% copper concentration after its initial increase. Third, the copper concentration decreases once 100% copper concentration is achieved.
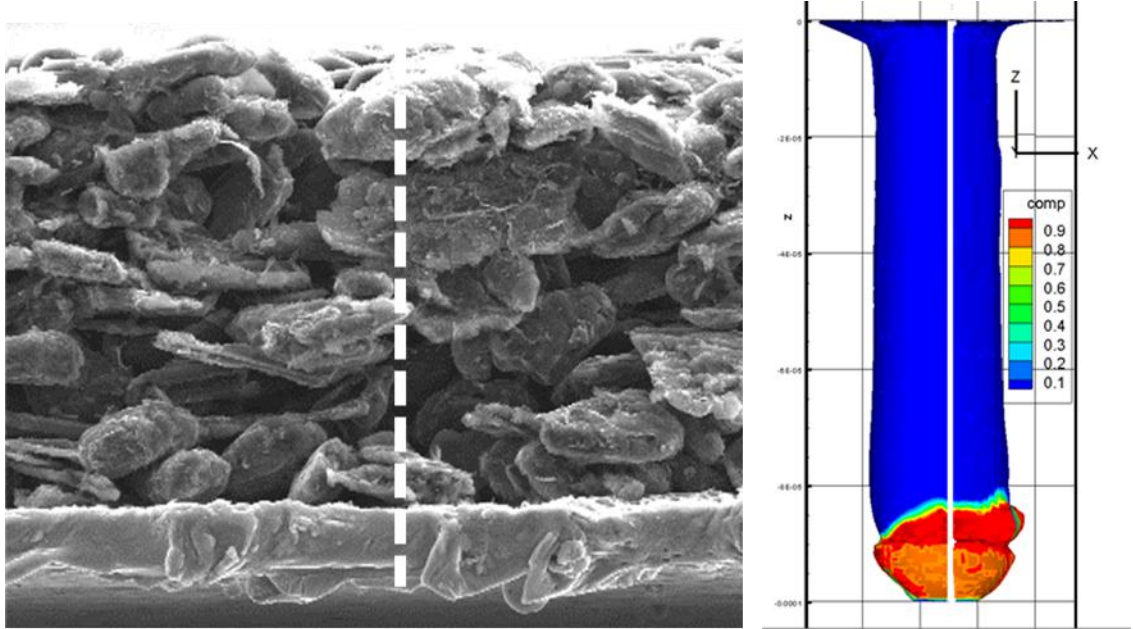
Figure 6.9. Copper composition variation along the line both for experimental sample (a) and simulation(b)
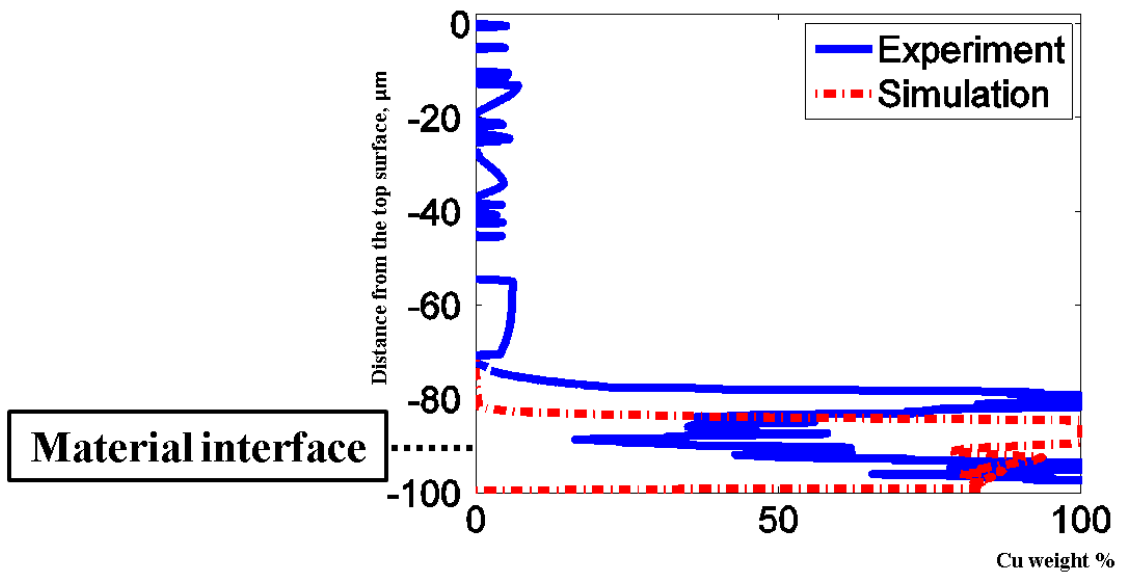
Figure 6.10. Comparison of the copper composition between experiment and simulation

Although both computational and experimental results share similar trends, there is a discrepancy in terms of kerf widths and the copper concentration. The discrepancy may be caused by three main factors. First, graphite is mixed with additives and binders during the graphite coating process. Hence, its material properties could be different from

the material properties of pure graphite, adapted in this simulation. Second, the extended copper and graphite binary diagram may give rise to this discrepancy. The liquid fraction can be overestimated since the binary diagram is extended. Finally, the simulation does not take into account the reactions with oxygen, or the air suction to hold the sample surface flat.

The simulation analysis in this study found strong outward liquid flow at the front of the deep penetration and composition changes on the graphite region. The strong outward flow of liquid copper gives rise to composition change and sharp edge formation on the cut surface. The composition change on the material interface may result in non-uniform electrochemical reactions and higher electrical stress, which can lead to significant heat generation and possible thermal runaway during the use of the lithium-ion battery cell. In addition, the sharp edge could penetrate the separator so that an internal short circuit occurs.
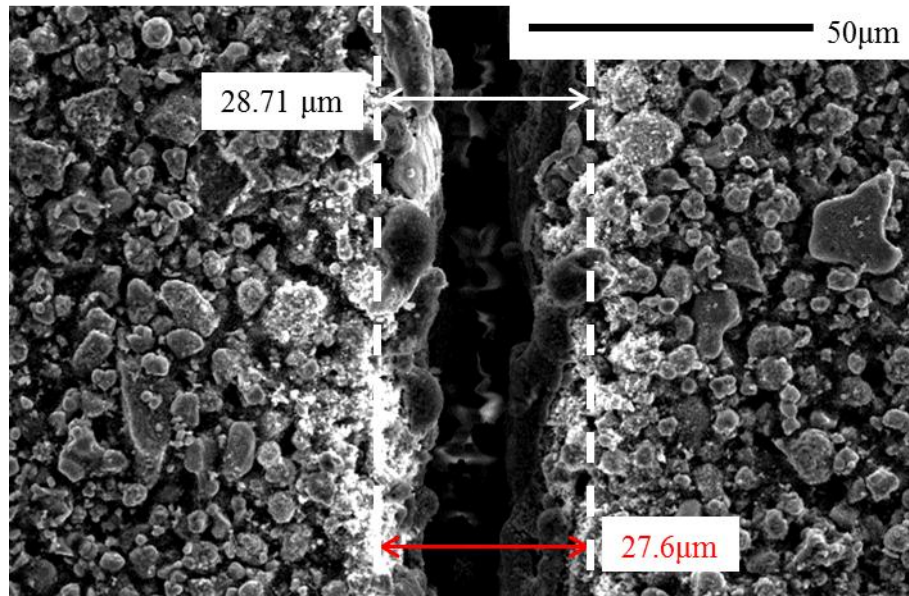
Figure 6.11. Top view of laser cut cathode

141
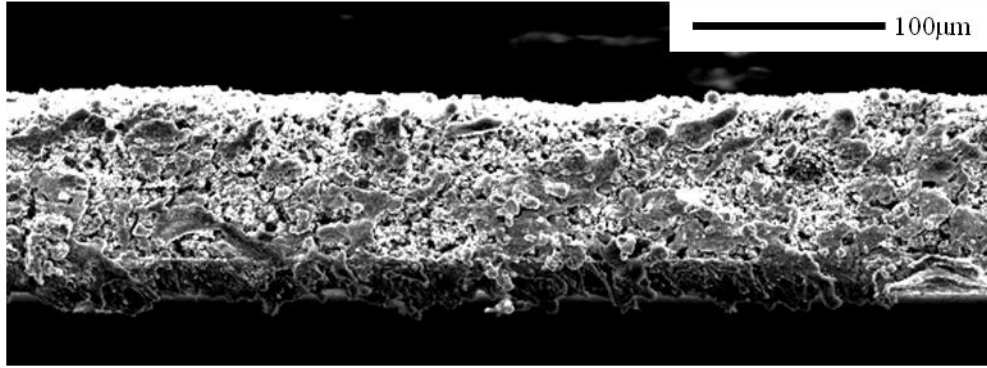
Figure 6.12. Side view of laser cut cathode

6.3.2. Cathode

The single side-coated cathode is used. The cathode is placed on the fixture as $LiCoO_2$ faces upward and the laser beam irradiates on the $LiCoO_2$ surface. Thickness of $LiCoO_2$ and aluminum are 85μm and 15μm, respectively. The laser power and scanning speed chosen are 150W and 5000 mm/s, respectively. The top and side views of a laser cut cathode are, as shown in Figure 6.11 and Figure 6.12, respectively. The kerf width is 27.6 μm. The dashed line depicts the kerf width obtained from the simulation. The kerf width obtained by simulation is 28.71μm and the simulation result overestimates by 4.02%, which is in good agreement with the experimental measurement. The side view of the laser cut cathode shows a good quality of cut surface. No delamination, edge banding, burrs, or micro-size attachments on the material interface are observed.

Figure 6.13. Aluminum composition variation along the line both for (a) experimental sample and (b) simulation

Figure 6.14. Comparison of the aluminum composition between experiment and simulation

Aluminum concentrations, obtained by both the simulation and experiment, are analyzed along the perpendicular line, as shown in Figure 6.13, and its values are plotted

in Figure 6.14. The aluminum concentration of the experimental cathode sample is obtained through EDX analysis. In Figure 6.14, the x-axis is weight percent of aluminum and the y-axis is the distance from the top surface to the bottom surface of the cathode.
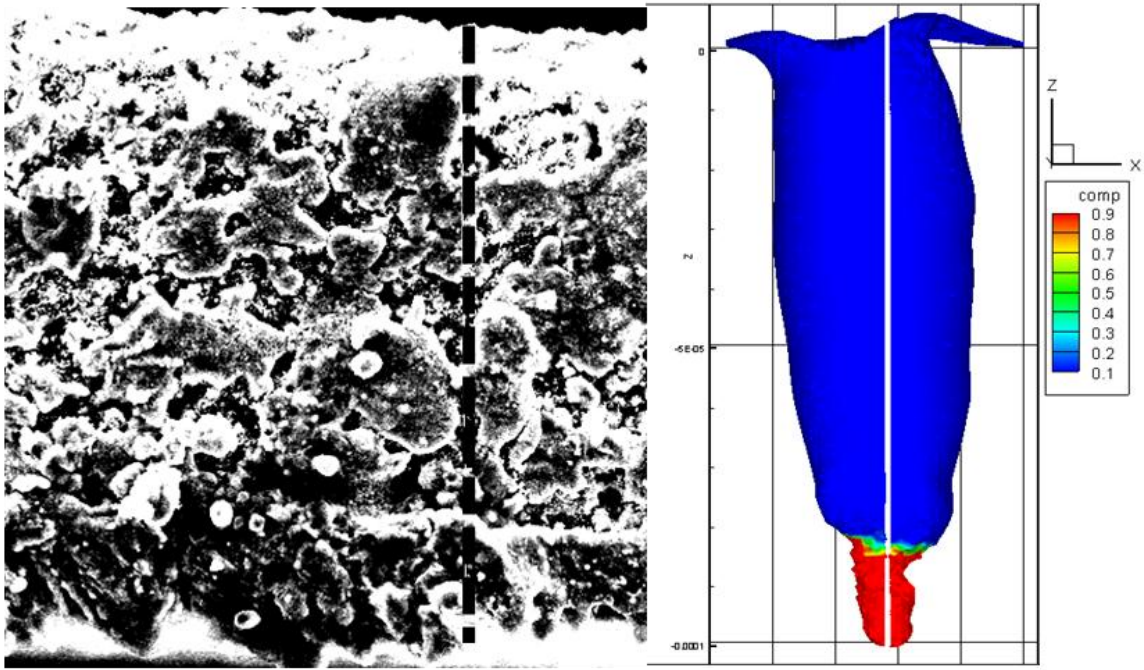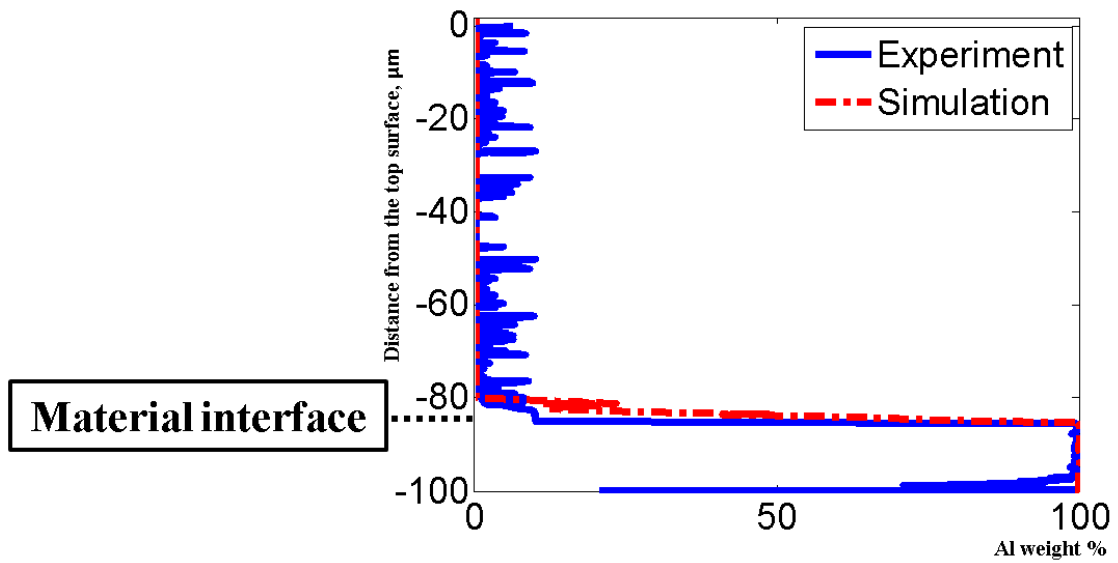
Even though the experimentally measured aluminum concentration varies, its weight percentage is less than 10%, and has no trend from the top surface to the depth of 81.36μm. The aluminum concentration increases significantly from the depth of 81.36μm to 85.63μm, where its value reaches 99.41%. Continuing from the depth of 85.63μm to 97.47μm, the aluminum concentration fluctuates between the weight percent of 98.46% and 100%. Finally, its value decreases to 73.86% at the depth of 98.63 μm. From the simulation result, the aluminum concentration starts to increase at the depth of 79.77μm. After this increase, it reaches 23.44% at 80.97μm, decreases to 12.02% at 82.16 μm, and then, reaches 100% aluminum concentration at 85.16 μm and maintains their value until 100 μm. Both the simulation and experimental results show that the aluminum concentration increases significantly around a depth of 80μm and reaches almost 100% around a depth of 85μm. In the alumimum region, from a depth of 85μm to 100μm, the aluminum concentration over the weight percent of 98.46% remains. The variation of the aluminum concentration predicted by the simulation is in good agreement with the experimental result.

Although both computational and experimental results share similar trends, there is a discrepancy. The discrepancy may be caused by three main factors. First, the material properties of $LiCoO_2$ used in the model are obtained by the law of fraction, while the experimental $LiCoO_2$ is mixed with additives and binders during the coating process. Hence, its material properties are likely different from the material properties of $LiCoO_2$,

adapted in this simulation. Second, the aluminum and cobalt binary diagram may give rise to this discrepancy. Although the mole fractions of lithium and oxygen are small, these may affect the physical phenomena during the high speed laser cutting of the cathode. Finally, the simulation does not take into account the reactions with oxygen, lithium, or cobalt.

6.4. Laser parameter optimization of electrodes

Based on the understanding of the laser cutting of electrodes through mathematical model, physical phenomena and its effects on the laser cutting of current collectors and electrodes are understood. Moreover, the mathematical model proposed in this study is verified by experimental measurements. Based on these understandings, laser parameters are optimized.
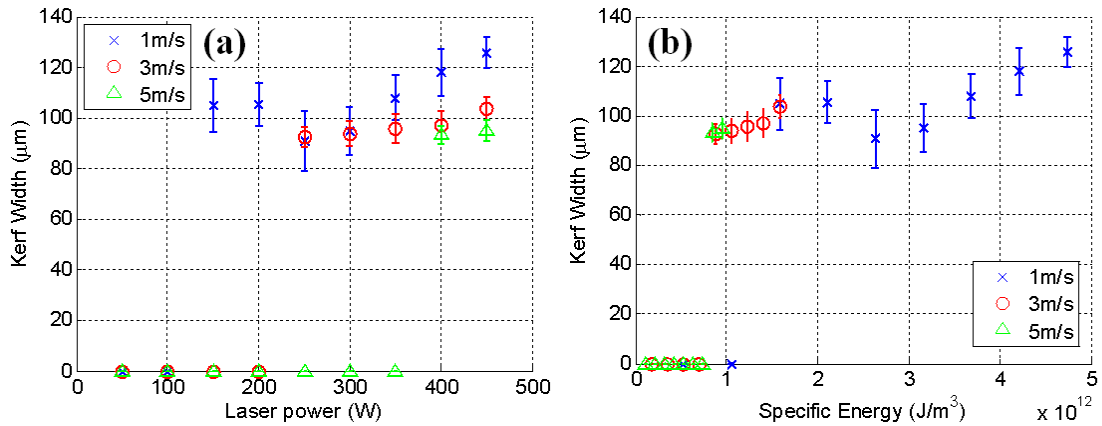

Figure 6.15. (a) Kerf width of anode VS laser power, (b) Kerf width of anode VS specific energy

As opposed to the conventional laser cutting process, remote cutting process provides less number of laser parameters to be controlled. In this section, laser power and scanning speed are chosen as laser parameters to be optimized. To investigate the effects

145

of these laser parameters, a wide range of laser power and scanning speed are utilized. These parameters are summarized in Table 6.1 for both anode and cathode. Graphite-coated copper and LiCoO$_2$-coated aluminum are the materials selected for anode and cathode, respectively. Both materials are single coated materials and active electrode materials are coated on the top of current collectors. Total thickness of anode and cathode are 100 μm. Graphite and LiCoO$_2$ has 90 μm and 85 μm thick, respectively. Experimental set-up is described in section 6.1. The laser irradiates on the top surface of the electrodes.

The kerf width of the laser cutting of the anode are shown in Figure 6.15 in terms of (a) laser power and (b) specific energy. Specific energy, E, is obtained as follows

$$E = \frac{P_{laser}}{V_s \cdot A}$$ (2.156)

where P_{laser} is the laser power, V_s is the scanning speed, and A is the laser spot size. If there is no cutting, zero is assigned for the kerf width.

Table 6.1. Laser parameters for parameter optimization of electrodes

Exp #	Laser power (W)	Laser speed (mm/s)
1	50	
2	100	
3	150	
4	200	
5	250	1000
6	300	
7	350	
8	400	
9	450	
10	50	
11	100	3000
12	150	
13	200	

14	250	
15	300	
16	350	
17	400	
18	450	
19	50	
20	100	
21	150	
22	200	
23	250	5000
24	300	
25	350	
26	400	
27	450	

Figure 6.16. (a) Side view and (b) top view of anode when P_{laser} =200 W, V_s =1000 mm/s

For the scanning speed of 1000 mm/s, the kerf width suddenly decreases when the value of the laser power is between 200W and 250W, and then the kerf width increases as the laser power increases, as seen in Figure 6.15 (a). The reason can be clearly explained by comparing the cut surface of the anode for these parameters, as shown in Figure 6.16 and Figure 6.17. Figure 6.16 and Figure 6.17 (a) and (b) are the side and top views of the cut surface of an anode using the laser power of 200W, and Figure 6.17 (a) and (b) are

147

the side and top views of the cut surface of an anode with the laser power of 250W. Delamination is observed in Figure 6.17 (a). If there is high recoil pressure, strong fluid flow of liquid copper at the material interface can be formed. This strong fluid flow can push the graphite upward so that delamination may be created. Furthermore, since laser energy contributes to not only the penetration of the material, but also the separation of graphite from copper, it can be possible that the kerf width decreases. Laser powers stronger than 250W provide delamination and show a linear relationship of laser power and kerf width, as shown in Figure 6.15 .
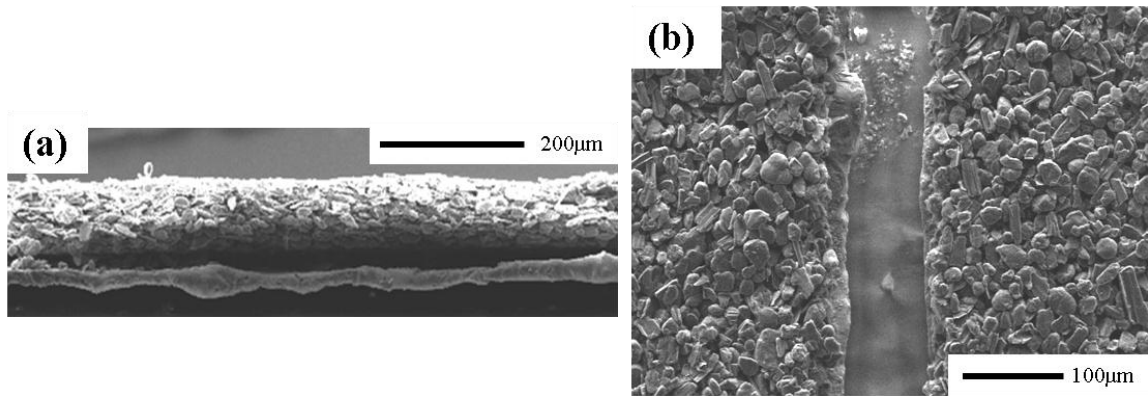
Figure 6.17. (a) Side view and (b) top view of anode when P_{laser} =250, V_s =1000 mm/s
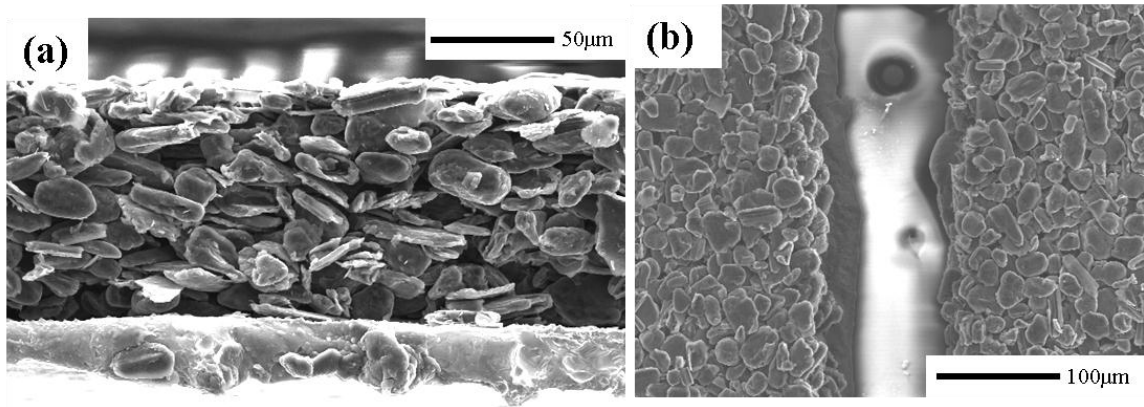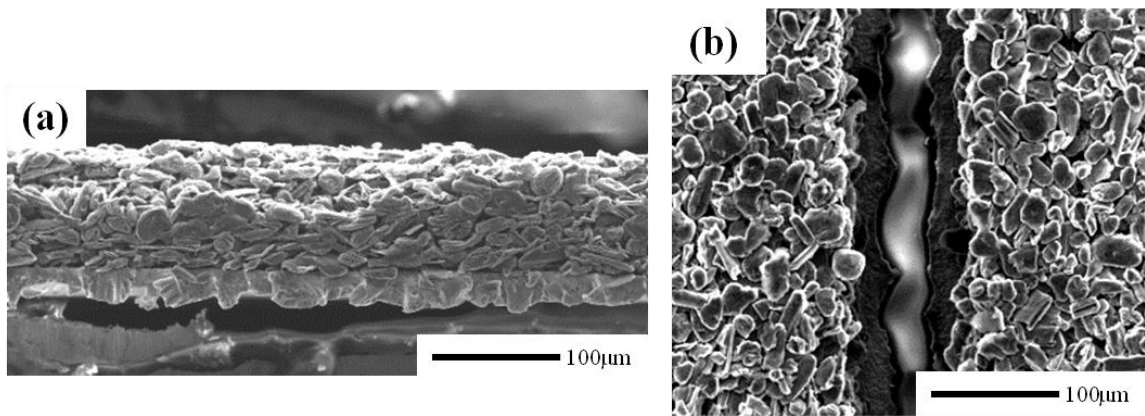

Figure 6.18. (a) Side view and (b) top view of anode when P_{laser} = 450, V_s =3000 mm/s

For the scanning speed of 3000 mm/s, clear cut surfaces are observed when laser powers are greater than 250W, which provides thorough cutting. Kerf width increases gradually until the maximum laser power used in these experiments is reached. No cutting occurs when the laser power is less than 200W, since the laser power is not sufficient to penetrate copper, which is obviously seen in Lee *et al.*'s paper [36] and in Figure 6.19.
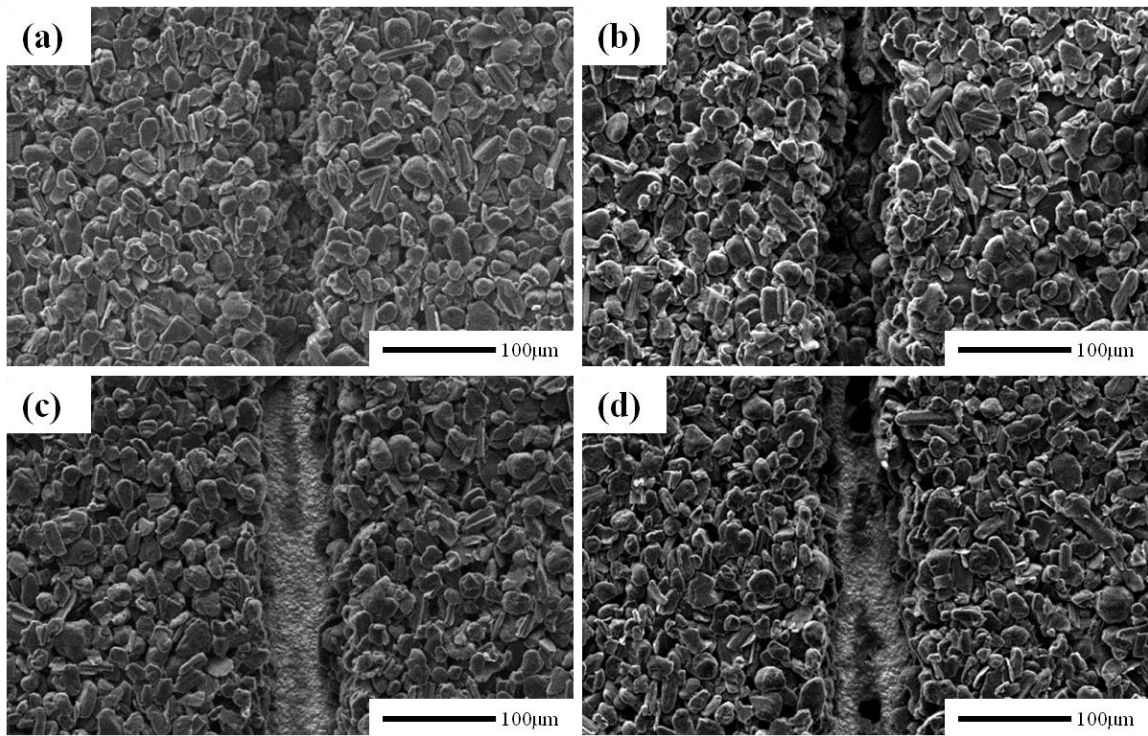
Figure 6.19. Top view of anode when V_s =3000 mm/s and (a) P_{laser} = 50, (b) P_{laser} = 100, (c) P_{laser} = 150, (d) P_{laser} = 200.
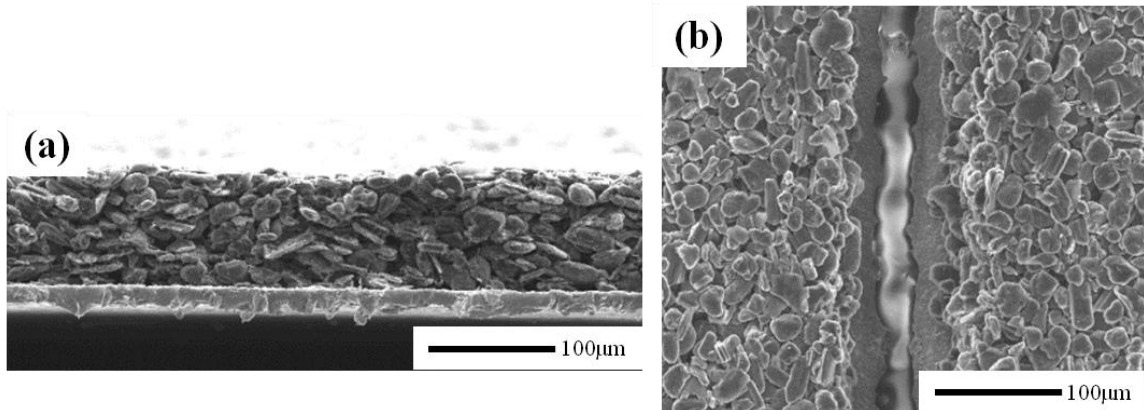
Figure 6.20. (a) Side view and (b) top view of anode when P_{laser} = 450, V_s =5000 mm/s
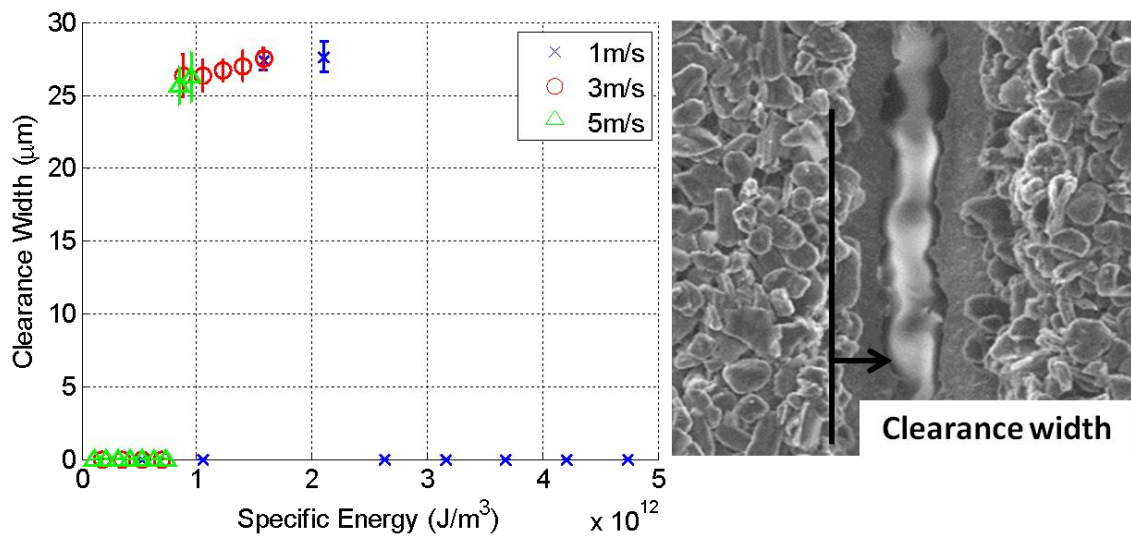
Figure 6.21. Clearance width of anode VS specific energy

For the scanning speed of 5000 mm/s, laser powers greater than 400W provide thorough cutting and show similar results to the case of scanning speed of 3000 mm/s, as shown in Figure 6.20. The effects of the controlled laser variables are even clearer when the kerf width is plotted with respect to the specific energy, as shown in Figure 6.15 (b). When the line energy is greater than 2.5×10^{12} J/m^3, delamination occurs. Moreover, the kerf width suddenly drops at this line energy, and it increases as the line energy increases. There is no cutting observed when the line energy is less than 0.8×10^{12} J/m^3. With line

energies between 0.8×10^{12} and 2.5×10^{12} J/m^3, an interesting phenomenon is observed: the kerf width of graphite is wider than that of copper, as seen in Figure 6.18 (b). Matthias *et al.* [27] defined this as a clearance width of the metal foil of anodes for lithium-ion batteries, which is the ablation width of the upper coating. The trend of clearance width of anode can be seen in Figure 6.21. The average value of the clearance width is almost gradually increasing from 25.61µm and 27.62µm. However, the difference of the clearance width in this line energy range is not significant. This clearance width is acceptable cutting quality, according to the study done by Matthias *et al.* [27]. There is no clearance width observed when the delamination exists. Therefore, the line energy between 0.8×10^{12} and 2.5×10^{12} J/m^3 provide a good quality of cut surface, and this can be used for the anode production.
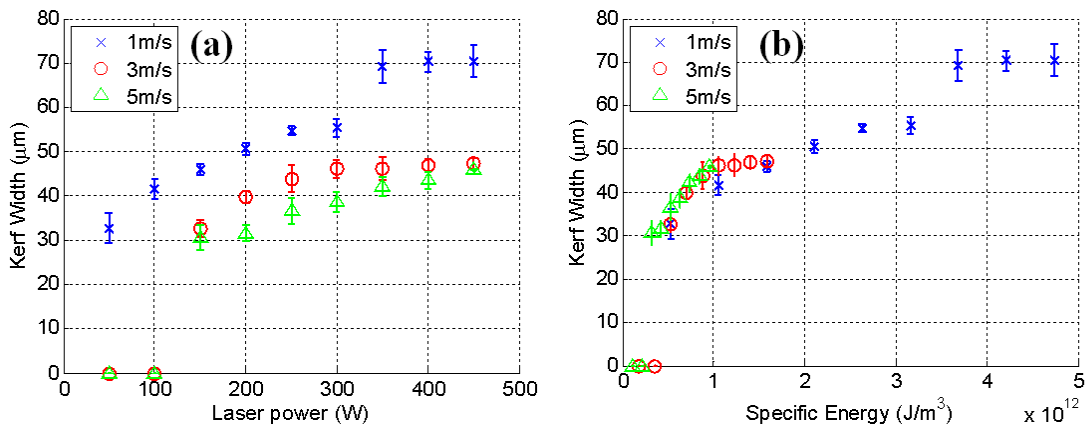
Figure 6.22. (a) Kerf width of cathode VS laser power, (b) Kerf width of cathode VS specific energy

The kerf width of the laser cutting of the cathode is shown in Figure 6.22 in terms of laser power (a) and specific energy (b). For the laser scanning speed of 1000 mm/s, thorough cutting occurs for the given laser powers. Under these given laser powers, no defects, such as burrs, delamination, or edge bending, are observed. The SEM images show the good quality of the cut surface, as seen in Figure 6.23. The kerf width of the

151

cathode increases gradually while increasing laser power up to 300W and then there is

sudden increase of kerf width observed at the laser power of 350W. After this sudden

increase, it increases gradually as the laser power increases. Although there is the sudden

increase of the kerf width of cathode, the quality of the cut surface is still good, as seen in

Figure 6.24.
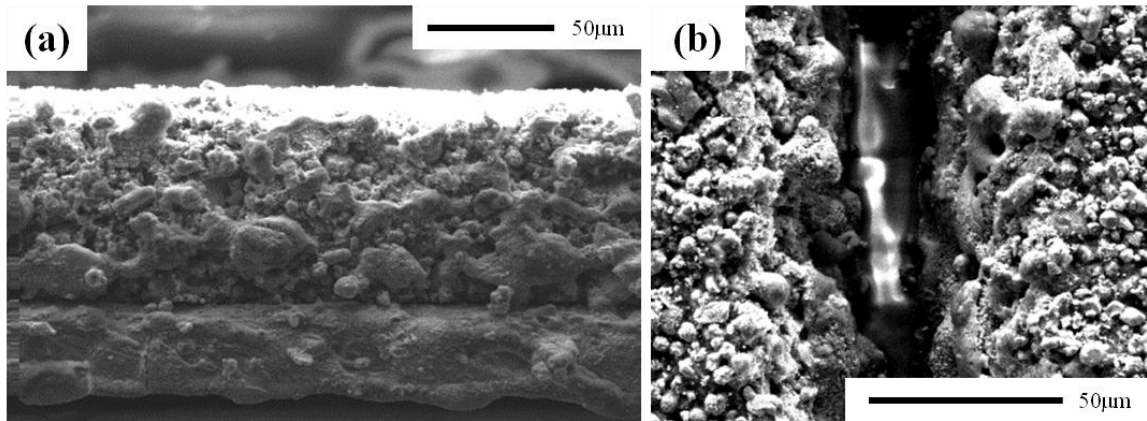
Figure 6.23. (a) Side view and (b) top view of cathode when $P_{laser} = 300$, $V_s = 1000$ mm/s
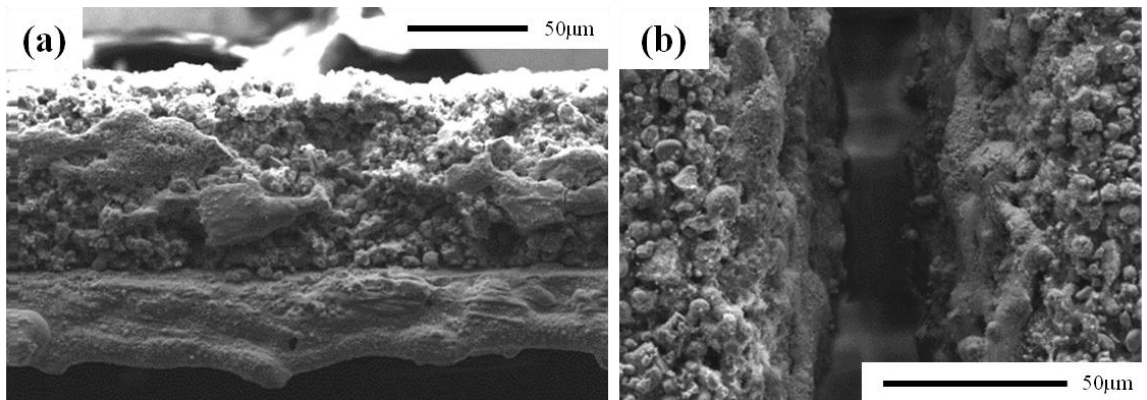
Figure 6.24. (a) Side view and (b) top view of cathode when $P_{laser} = 450$, $V_s = 1000$ mm/s
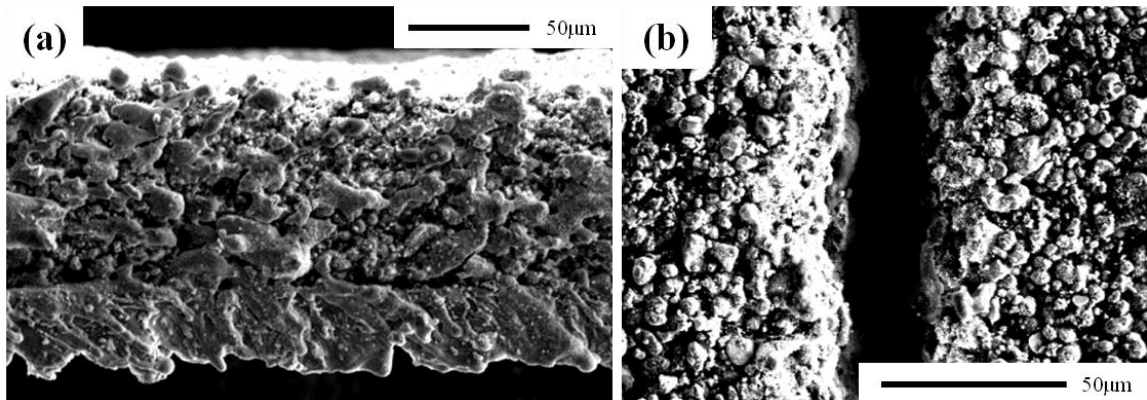
Figure 6.25. (a) Side view and (b) top view of cathode when $P_{laser} = 150$, $V_s = 3000$ mm/s

For the laser scanning speed of 3000 mm/s, the kerf width increases gradually from 32.63μm to 46μm and then it saturates to 46μm when the laser power is greater than 300W. Under the given laser power and speed, the good quality of cut surface is observed as shown in Figure 6.25.
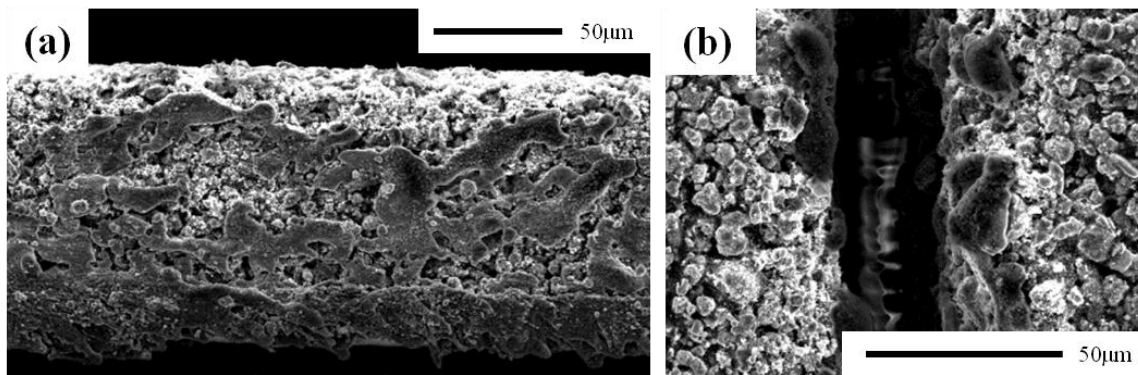
Figure 6.26. (a) Side view and (b) top view of cathode when $P_{laser} = 300$, $V_s = 5000$ mm/s

For the laser scanning speed of 5000 mm/s, thorough cutting occurs if the laser power is 150W and greater. Again, the good quality of cut surface is observed for all thorough cutting cases, as shown in Figure 6.26. All the three cases of scanning speed show similar trends with increasing laser power. This trend is even clearer if the kerf width is plotted in terms of the specific energy, as seen in Figure 6.22 (b), and can be categorized into three regions. The first region is the no cutting region when the line energy is less than 0.31×10^{12} J/m^3. If the line energy is greater than 0.31×10^{12} J/m^3 and less than 3.5×10^{12} J/m^3, a clear cut surface can be seen. The kerf width increases significantly when the line energy is greater than 3.5×10^{12} J/m^3 with a good quality of cut surface.

6.5. Conclusions

In this chapter, the simulation results of the laser cutting of current collectors and electrodes are validated by comparing experimental results. In addition, the optimal laser parameters providing good cut surface quality are obtained. Experimental and simulation results of pure current collectors show a strong agreement for the high-speed cutting cases, such as 3000 and 5000 mm/s. A small discrepancy observed for low-speed cutting, or 1000 mm/s, can be improved by modifying the constant absorption coefficient to be a temperature dependent absorption coefficient. A bubble-shape recast observed from experimental results could deteriorate the cut surface of electrodes for lithium-ion batteries. Simulation results of pure copper are in good agreement with experimental results of pure copper with single side-coated graphite when a laser scanning speed is 3000 mm/s. Experimental results of pure aluminum with single side-coated $LiCoO_2$ match well with simulation results of pure aluminum when a laser scanning speed is 5000 mm/s.

The cut surface, kerf width, and copper composition of the experimentally obtained anode sample are measured by SEM and EDX analyses. A good cut surface is obtained. Kerf widths show a discrepancy with simulation results. The discrepancy may be caused by the properties of the graphite sample used for the experiments, the extended copper and graphite binary diagram in the simulation, or the lack of oxygen reaction and air suction included in the simulation. In spite of these discrepancies, both experimentally and computationally obtained copper concentrations share key characteristics. The copper concentration starts to increase its value at least 10μm above the material interface and increases very sharply up to 100% copper concentration after its initial increase. In

addition, the copper concentration decreases once 100% copper concentration is achieved.

The cathode simulation is also validated by the experiment in terms of the kerf width and aluminum composition changes along the vertical line of the cut surface through SEM and EDX analyses. The result predicted by the simulation is in good agreement with the experimental result. The kerf width from the simulation overestimates its value from the experimental result by 4.02%. Both simulation and experimental results share two characteristics of the aluminum concentration. It increases significantly around a depth of 80μm and reaches almost 100% around a depth of 85μm. In the aluminum region, the aluminum concentration over the weight percent of 98.46% is maintained. Discrepancies between the model and experiment may be due to the material properties of the $LiCoO_2$ obtained using the law of fraction, the binary diagram of aluminum and cobalt, and the lack of considerations of reaction with oxygen, lithium, or cobalt.

The high speed remote laser cutting of electrodes for lithium-ion batteries are experimentally performed to obtain the optimal laser parameters. The line energy is defined as dividing laser power by scanning speed and spot size. When the line energy is between 0.8×10^{12} and 2.5×10^{12} J/m^3, a good quality of cut surface of the anode is achieved. The clearance width is observed and its values are less than 29.1 μm, which is acceptable. If the line energy is greater than 0.31×10^{12} J/m^3 and less than 3.5×10^{12} J/m^3, a clear cut surface of cathodes can be seen. The line energy ranges obtained above provide a good cut surface quality of electrodes with no defects, such as delamination, burrs, edge bending, or micro-sized material attachments.

Therefore, these optimized laser parameters can provide a critical guideline for the future developments of laser cutting of electrodes for lithium-ion batteries for different applications, since electrode sizes vary depending on applications. In addition, such electrodes with good cut quality in the lithium-ion battery cells can prevent internal short circuits, thermal stress, significant heat generation, and eventually a catastrophic failure of the entire module. Furthermore, the high speed remote laser cutting would improve the productivity and reduce manufacturing cost.

CHAPTER VII

CONTRIBUTIONS, LIMITATIONS AND FUTURE WORK

7.1. Contributions

The presented study has many contributions to the knowledge base of the physical phenomena that take place during the laser cutting of electrodes for lithium-ion batteries. In summary:

1. A self-consistent three-dimensional transient model was developed for the high speed remote laser cutting of electrodes for lithium-ion batteries, based on the mathematical model of the laser-material interaction. Physical phenomena including heat and fluid flow, composition change, multiple reflections, recoil pressure, surface tension, evaporation, solidification, melting, and composite materials, were modeled and solved numerically. The developed model is applied to single materials, such as, mild steel, aluminum and copper as well as composite materials, such as graphite-coated copper and $LiCoO_2$-coated aluminum, using proper modifications.

2. The effects of laser beam modes on the laser-material interaction are investigated to a have better understanding of important physical phenomena for each case, such as keyhole formation, keyhole collapse, melt pool flow

patterns, and response times. With the given laser parameters, the TEM_{00} and Top-hat laser beam cases are of the deep penetration mode. Hence, TEM_{00} and Top-hat laser beam cases might be more efficient for high intensity laser manufacturing processes, i.e. cutting. The criteria of the keyhole collapse are provided. The TEM_{01*} and TEM_{22} laser beam cases are of the conduction mode, where the depth gradually grew and was maintained without severe fluctuation during the entire simulation. Therefore, these cases could be utilized more efficiently for surface treatment processes.

3. The model was applied to the laser cutting of current collectors using a wide range of the laser parameters. The thresholds for the laser cutting are obtained. The analysis of the results shows that the copper laser cutting is a laser intensity and interaction time dependent process. Moreover, the aluminum laser cutting depends more on laser intensity than interaction time. Under the laser parameters near the thresholds of the laser cutting that provide thorough cutting, the penetration depth and width of copper increase along two different slopes, due to the transition from partial to full penetration laser cutting and crest formation. Aluminum increases both its penetration depth and width relatively smoothly, due to the strong upward flow and momentum of the liquid aluminum.

4. The model was applied to the laser cutting of electrodes. The characteristics of penetration depth and absorptivity change significantly at the point where the deep penetration hole reaches the material interface, due mainly to the

composition change at the material interface, melt pool flow pattern, L/V interface geometry, and material properties.

5. At the beginning of the simulation, the L/V interface shows a smooth and clean surface for the anode. For the cathode, the deep penetration hole shows an uneven surface and creates crests on the top surface and the protrusion. In addition, as the deep penetration hole deepens, uneven surfaces are observed near the tip of the deep penetration hole, and smoother melt pool surfaces are observed near the top surface.

6. When the deep penetration hole reaches the material interface, for the anode, a melt pool starts to form, develops and results in a two-level surface. In addition, higher values of copper concentration are observed around the material interface. When the deep penetration hole becomes deepens, the copper concentration is distributed more uniformly and the front melt pool provides strong melt pool flow in the copper region. For the cathode, when the deep penetration hole reaches the material interface, the narrower deep penetration hole forms in the aluminum region. In addition, the merged flow pattern contributes to the aluminum composition change, which remains high in the aluminum region.

7. The proposed mathematical model is validated experimentally. Experimental and simulation results of pure current collector materials show a strong agreement for the high-speed cutting cases. For both the anode and cathode, a good cut surface is observed with the given laser parameters. For the anode, both experimentally and computationally obtained copper concentrations

share key characteristics. The copper concentration starts to increase its value at least 10μm above the material interface and increases very sharply-up to 100% copper concentration after its initial increase. In addition, the copper concentration decreases once 100% copper concentration is achieved in the copper region. For the cathode, the kerf width from the simulation estimates its value from the experimental result with an error of 4.02% for the cathode. Both simulation and experimental results share the following two characteristics of the aluminum concentration. It increases significantly around the depth of 80μm and reaches almost 100% around the depth of 85μm. In the aluminum region, the aluminum concentration over the weight percent of 98.46% is maintained.

8. The high speed remote laser cutting of electrodes for lithium-ion batteries are experimentally performed to obtain the optimal laser parameters. The optimal range of line energy is between 0.8×10^{12} and 2.5×10^{12} J/m^3 for the anodes and is between 0.31×10^{12} J/m^3 and 3.5×10^{12} J/m^3 for the cathodes. The line energy ranges obtained above provide a good cut surface quality of electrodes with no defects, such as delamination, burrs, edge bending, or micro-sized material attachments.

9. The proposed mathematical model of the laser cutting of electrodes for lithium-ion batteries can be utilized to predict and prevent defects, thermal stress, internal short circuits, significant heat generation, and the eventual catastrophic failure of the entire module by analyzing the L/V interface geometry, melt pool flow pattern, composition change and temperature

distribution. Furthermore, the high speed remote laser cutting would improve the productivity and reduce manufacturing cost.

7.2. Limitations and future work

The limitations of this study are caused by the simplifying assumptions. Those limitations along with any suggestions for improvements are summarized. Furthermore, possible future research directions and applications using the proposed model will be discussed.

Limitations of this model can be derived from the simplification of physical phenomena during the laser cutting of electrodes for lithium-ion batteries, such as material properties, the compressibility of gases, and plasma-laser interactions. Material properties of $LiCoO_2$ are obtained by the law of fraction, and the phase diagram of cobalt and aluminum was used due to the lack of the available data of $LiCoO_2$. The model could have provided a better prediction of the physical phenomena if more accurate material properties were available for cathode. Furthermore, the extension of the phase diagram of graphite and copper due to its limited solubility may affect the accuracy of the proposed model, There is a discrepancy for the low speed cutting of current collectors. The reason for this might be that the mathematical model used a constant absorption coefficient. Therefore, including a temperature dependent absorption coefficient might improve the prediction of the mathematical model for the low speed cutting. Gas flow is assumed to be incompressible for the sake of simplicity. Since gas flow is highly compressible, depending on laser beam intensity, a mathematical model of compressible flow in the gas

phase can be introduced while solving incompressible flow in the liquid phase. Plasma is not considered in this model. Due to the ionization and further heating of the metal vapor, the actual energy deposition on the L/V interface can be reduced by a significant amount. Hence, considering plasma-laser interaction can provide a more realistic estimation. Moreover, chemical reactions among the materials and oxygen are not considered in the governing equations. Addressing these limitations of the model would minimizing the error in a future model.

Unavailable material properties can be calculated using "Thermo-calc", which is a commercial software package used to perform thermodynamic and phase diagram calculations for multi-component systems of practical importance. Furthermore, Van der Ven *et al.* [118] provides an overview of the statistical mechanical tools that have been developed to predict both thermodynamic potentials, phase stability and diffusion coefficients in multi-component solids. Based on the review, they can calculate the diffusion coefficient as a function of Li concentration x in Li_xTiS_2 [119]. Applying this method to the $LiCoO_2$ can improve the accuracy of the mathematical model proposed in this study. Furthermore, Diffusion rate of lithium in aluminum at low temperature is given as a function of temperature between 150 and 240°C [120]. Considering the lithium diffusion in aluminum may improve the proposed model since it is highly related to the non-uniform electrochemical reaction, which leads to significant heat generation.

The findings of this study are restricted to one-side coated electrodes. If this model were to be evolved to two-side coated electrodes, it would provide the mathematical model with a flexibility to investigate not only the physical phenomena but also the effects of various types of electrodes for lithium-ion batteries. The mathematical

model developed in this study could also be utilized to study the influence of the thickness of active electrode materials and current collectors. The developed mathematical model including interaction physics, could also be modified and applied to the high intensity laser manufacturing of sandwiched composite materials, such as solar cells, liquid-emitting diodes (LED), and active-matrix organic light-emitting diodes (AMOLED).

BIBLIOGRAPHY

[1] T. Nakata, M. Rodionov, D. Silva, J. Jupesta, Science China-Technological Sciences, 53 (2010) 134-143.

[2] IEA, in, 2011.

[3] A. Zwaniecki, in.

[4] in, Boston consulting group report, 2009.

[5] M. Alamgir, A.M. Sastry, in: SAE Convergence, Detroit, MI, 2008.

[6] M. Winter, R.J. Brodd, Chemical Reviews, 104 (2004) 4245-4269.

[7] D.L. Anderson, in: Nicholas School of the Environment, Duke, 2009.

[8] M. Park, X. Zhang, M. Chung, G.B. Less, A.M. Sastry, Journal of Power Sources, 195 (2010) 7904-7929.

[9] M. Broussely, P. Biensan, B. Simon, Electrochimica Acta, 45 (1999) 3-22.

[10] Q. Wang, W. Zhang, Z. Yang, S. Weng, Z. Jin, Journal of Power Sources, 196 (2011) 10176-10182.

[11] T. Muraliganth, A.V. Murugan, A. Manthiram, Journal of Materials Chemistry, 18 (2008) 5661-5668.

[12] A.V. Murugan, T. Muraliganth, A. Manthiram, Journal of Physical Chemistry C, 112 (2008) 14665-14671.

[13] R. Amin, P. Balaya, J. Maier, Electrochemical and Solid State Letters, 10 (2007) A13-A16.

[14] H. Kim, J. Cho, Nano Letters, 8 (2008) 3688-3691.

[15] C.C. Nguyen, S.-W. Song, Electrochemistry Communications, 12 (2010) 1593-1595.

[16] H. Guo, H. Zhao, C. Yin, W. Qiu, Journal of Alloys and Compounds, 426 (2006) 277-280.

[17] M.N. Obrovac, L. Christensen, Electrochemical and Solid State Letters, 7 (2004) A93-A96.

[18] T. Zhang, J. Gao, L.J. Fu, L.C. Yang, Y.P. Wu, H.Q. Wu, Journal of Materials Chemistry, 17 (2007) 1321-1325.

[19] W. Communications, in.

[20] M.F. Zaeh, J. Moesl, J. Musiol, F. Oefele, Physics Procedia, 5, Part A (2010) 19-33.

[21] G. Antonova, G. Gladush, A. Krasyukov, F. Kosyrev, N. Rodionov, High Temperature, 38 (2000) 477-482.

[22] G. Tahmouch, P. Meyrueis, P. Grandjean, Optics & Laser Technology, 29 (1997) 307-315.

[23] H.J. Herfurth, R. Patwa, H. Pantsar, S. Heinemann, G. Newaz, in: Proceedings of the ICALEO, Temecula, CA USA, 2008.

[24] H.J. Herfurth, R. Patwa, H. Pantsar, in: Proceedings of the LPM, Germany, 2010.

[25] R. Patwa, H.J. Herfurth, H. Pantsar, S. Heinemann, J. Mazumder, D. Lee, in: Proceedings of the ICALEO, Anaheim, CA, 2010.

[26] W.M. Steen, J. Mazumder, SpringerLink (Online service), in, Springer-Verlag London, London, 2010.

[27] M. Luetke, V. Franke, A. Techel, T. Himmer, U. Klotzbach, A. Wetzig, E. Beyer, Physics Procedia, 12 (2011) 286-291.

[28] C.L. Chan, J. Mazumder, Journal of Applied Physics, 62 (1987) 4579-4586.

[29] A. Kar, J. Mazumder, Journal of Applied Physics, 68 (1990) 3884-3891.

[30] A. Kar, T. Rockstroh, J. Mazumder, Journal of Applied Physics, 71 (1992) 2560-2569.

[31] H. Ki, P.S. Mohanty, J. Mazumder, Journal of Physics D-Applied Physics, 34 (2001) 364-372.

[32] H. Ki, P.S. Mohanty, J. Mazumder, 20th Icaleo 2001, Vols 92 & 93, Congress Proceedings, (2001) 933-942.

[33] H. Ki, P.S. Mohanty, J. Mazumder, Metallurgical and Materials Transactions a-Physical Metallurgy and Materials Science, 33 (2002) 1817-1830.

[34] H. Ki, P.S. Mohanty, J. Mazumder, Metallurgical and Materials Transactions a-Physical Metallurgy and Materials Science, 33 (2002) 1831-1842.

[35] H. Ki, P.S. Mohanty, J. Mazumder, Numerical Heat Transfer Part B-Fundamentals, 48 (2005) 125-145.

[36] D. Lee, R. Patwa, H. Herfurth, J. Mazumder, Journal of Power Sources, 210 (2012) 327-338.

[37] C.J. Knight, Aiaa Journal, 17 (1979) 519-523.

[38] T. Ytrehus, S. Ostmo, International Journal of Multiphase Flow, 22 (1996) 133-155.

[39] J.Y. Lee, S.H. Ko, D.F. Farson, C.D. Yoo, Journal of Physics D-Applied Physics, 35 (2002) 1570-1576.

[40] A.F.H. Kaplan, M. Mizutani, S. Katayama, A. Matsunawa, First International Symposium on High-Power Laser Macroprocessing, 4831 (2003) 186-191.

[41] W.D. Bennon, F.P. Incropera, International Journal of Heat and Mass Transfer, 30 (1987) 2161-2170.

[42] H. Ki, Modeling and measurement of processes with liquid-vapor interface created by high power density lasers, 2001.

[43] s. Asai, I. Muchi, Trasaction ISIJ, 18 (1978) 90-98.

[44] G.A. Lopez, E. Mittemeijer, Scripta Materialia, 51 (2004) 1-5.

[45] M.B. Bever, C.F. Floe, Transactions of the American Institute of Mining and Metallurgical Engineers, 166 (1946) 128-143.

[46] M. Sussman, P. Smereka, S. Osher, Journal of Computational Physics, 114 (1994) 146-159.

[47] P. Smereka, in, Technical report, Lecture notes from a short course given at INRIA.

[48] H. Ki, J. Mazumder, P. Mohanty, Metallurgical and Materials Transactions A, 33 (2002) 1817-1830.

[49] R. Rai, G.G. Roy, T. DebRoy, Journal of Applied Physics, 101 (2007).

[50] J.-H. Cho, S.-J. Na, Journal of Physics D: Applied Physics, 39 (2006) 5372-5378.

[51] K. Shimoda, Introduction to laser physics, 2 ed., Springer-Verlag, Yokohama, 1986.

[52] P.J.O. R C Crafer, Laser processing in manufacturing, Cahpman & hall, London, 1993.

[53] J.F.B.H. J Wilson, Lasers: principles and applications, Prentice Hall, Essex, 1987.

[54] A.E. Siegman, Lasers, University sicence books, Mill Valley, 1986.

[55] R. Fabbro, K. Chouf, Journal of Applied Physics, 87 (2000) 4075-4083.

[56] S. Osher, J.A. Sethian, Journal of Computational Physics, 79 (1988) 12-49.

[57] J.A. Sethian, Level set tmethods and fast marching methods, 2nd ed., Cambridge University Press, Cambridge, 1999.

[58] C. Prakash, V. Voller, Numerical Heat Transfer Part B-Fundamentals, 15 (1989) 171-189.

[59] S.V. Patankar, Numerical heat transfer and fluid flow, Hemisphere Pub. Corp. ; McGraw-Hill, Washington

New York, 1980.

[60] S.V. Patankar, Numerical heat transfer and fluid flow, Hemisphere Pub. Corp. ; McGraw-Hill, Washington

New York, 1980.

[61] J.P. Vandoormaal, G.D. Raithby, Numerical Heat Transfer, 7 (1984) 147-163.

[62] J.A. Sethian, Level set methods and fast marching methods : evolving interfaces in computational geometry, fluid mechanics, computer vision, and materials science, 2nd ed., Cambridge University Press, Cambridge, U.K. ; New York, 1999.

[63] J.A. Sethian, J. Strain, Journal of Computational Physics, 98 (1992) 231-253.

[64] J. Enderlein, F. Pampaloni, J. Opt. Soc. Am. A, 21 (2004) 1553-1558.

[65] A.F.H. Kaplan, Applied Physics Letters, 70 (1997) 264-266.

[66] D. Triantafyllidis, J.R. Bernstein, L. Li, F.H. Stott, 15 (2003) 49-54.

[67] D. Triantafyllidis, L. Li, F.H. Stott, 18 (2006) 267-274.

[68] L. Han, F.W. Liou, International Journal of Heat and Mass Transfer, 47 (2004) 4385-4402.

[69] H. Ki, in: MECHANICAL ENGINNERING, UNIVERSITY OF MICHIGAN, ANN ARBOR, 2001, pp. 151.

[70] H. Ki, P.S. Mohanty, J. Mazumder, 14 (2002) 39-45.

[71] X.Z. Jin, Optics and Lasers in Engineering, 46 (2008) 83-93.

[72] X.Z. Jin, P. Berger, T. Graf, Journal of Physics D-Applied Physics, 39 (2006) 4703-4712.

[73] J.-H. Cho, S.-J. Na, 39 (2006) 5372-5378.

[74] W.W. Duley, Laser welding, Wiley, New York, 1999.

[75] V. Semak, A. Matsunawa, 30 (1997) 2541-2552.

[76] A. Matsunawa, V. Semak, 30 (1997) 798-809.

[77] H. Ki, J. Mazumder, P. Mohanty, 33 (2002) 1831-1842.

[78] R. Rai, G.G. Roy, T. DebRoy, 101 (2007) 054909-054911.

[79] L. Han, F.W. Liou, 47 (2004) 4385-4402.

[80] R. Rai, S.M. Kelly, R.P. Martukanitz, T. DebRoy, 39 (2008) 98-112.

[81] H. Wang, Y. Shi, S. Gong, 39 (2006) 4722-4730.

[82] X.-H. Ye, X. Chen, 35 (2002) 1049-1056.

[83] R.D. Seidgazov, Journal of Physics D-Applied Physics, 42 (2009) 7.

[84] L. Quintino, A. Costa, R. Miranda, D. Yapp, V. Kumar, C.J. Kong, 28 (2007) 1231-1237.

[85] D.P. C. Benter, R. poprawe, in: Interational WLT-Conference on Lasers in Manufacturing, Munich, 2005.

[86] J.Y. Lee, S.H. Ko, D.F. Farson, C.D. Yoo, 35 (2002) 1570-1576.

[87] R. Fabbro, K. Chouf, 87 (2000) 4075-4083.

[88] A.F.H. Kaplan, M. Mizutani, S. Katayama, A. Matsunawa, 35 (2002) 1218-1228.

[89] M.J. Assael, K. Kakosimos, R.M. Banish, J. Brillo, I. Egry, R. Brooks, P.N. Quested, K.C. Mills, A. Nagashima, Y. Sato, W.A. Wakeham, Journal of Physical and Chemical Reference Data, 35 (2006) 285-300.

[90] B.B. Alchagirov, A.M. Chochaeva, V.B. Bekulov, K.B. Khokonov, High Temperature, 41 (2003) 472-476.

[91] R. Brandt, G. Neuer, International Journal of Thermophysics, 28 (2007) 1429-1446.

[92] E.H. Buyco, F.E. Davis, Journal of Chemical and Engineering Data, 15 (1970) 518-&.

[93] N.Y. Konstantinova, P.S. Popel, D.A. Yagodin, High Temperature, 47 (2009) 336-341.

[94] T. Matsumoto, H. Fujii, T. Ueda, M. Kamai, K. Nogi, Measurement Science & Technology, 16 (2005) 432-437.

[95] M.A. Bramson, in, Plenum Press, New York,, 1968, pp. xii, 623 p.

[96] D. Lee, J. Mazumder, in: Proceedings of the ICALEO, Laser institute of America, Anaheim, California, 2010.

[97] J.H. Cho, S.J. Na, Journal of Physics D-Applied Physics, 39 (2006) 5372-5378.

[98] A. De, T. DebRoy, Journal of Applied Physics, 95 (2004) 5230-5240.

[99] M. Musella, C. Ronchi, M. Brykin, M. Sheindlin, Journal of Applied Physics, 84 (1998) 2530-2537.

[100] H.R. Leider, O.H. Krikorian, D.A. Young, Carbon, 11 (1973) 555-563.

[101] M. Shusser, Journal of Applied Physics, 101 (2007).

[102] Y. Ito, K. Minami, A. Nagashima, International Journal of Thermophysics, 10 (1989) 173-182.

[103] V.I. Lad'yanov, A.L. Bel'tyukov, K.G. Tronin, L.V. Kamaeva, Jetp Letters, 72 (2000) 301-303.

[104] W.J. Yao, X.J. Han, M. Chen, B. Wei, Z.Y. Guo, Journal of Physics-Condensed Matter, 14 (2002) 7479-7485.

[105] T. Nishi, H. Shibata, H. Ohta, Y. Waseda, Metallurgical and Materials Transactions a-Physical Metallurgy and Materials Science, 34A (2003) 2801-2807.

[106] X.J. Han, J.Z. Wang, M. Chen, Z.Y. Guo, Journal of Physics-Condensed Matter, 16 (2004) 2565-2574.

[107] E.W. Lemmon, R.T. Jacobsen, International Journal of Thermophysics, 25 (2004) 21-69.

[108] Vanitter.A, H. Zink, Helleman.J, Physica, 32 (1966) 489-&.

[109] S.D. Bembenek, Journal of Chemical Physics, 124 (2006).

[110] D. Celik, S.W. Van Sciver, Cryogenics, 45 (2005) 620-625.

[111] R.D. Goodwin, L.A. Weber, Journal of Research of the National Bureau of Standards Section a-Physics and Chemistry, A 73 (1969) 1-&.

[112] W. AG, in, Wyon AG, Switzerland.

[113] D. Lee, J. Mazumder, in: Proceedings of the ICALEO, Laser institute of America, Orlando, Florida, 2011.

[114] J. Mazumder, D. Lee, J. Tübke, K. Pinkwart, H. Herfurth, R. Patwa, in, University of Michigan

Fraunhofer, 2011.

[115] S. Katayama, N. Seto, J.D. Kim, A. Matsunawa, Laser Materials Processing Conference, Pts 1 & 2, (1997) G83-G92.

[116] V.V. Semak, W.D. Bragg, B. Damkroger, S. Kempka, Journal of Physics D-Applied Physics, 32 (1999) L61-L64.

[117] R. Fabbro, K. Chouf, High-Power Lasers in Manufacturing, 3888 (2000) 104-112.

[118] A. Van der Ven, J.C. Thomas, Q. Xu, J. Bhattacharya, Mathematics and Computers in Simulation, 80 (2010) 1393-1410.

[119] J. Bhattacharya, A. Van der Ven, Physical Review B, 83 (2011).

[120] C. Moreau, A. Allouche, E.J. Knystautas, Journal of Applied Physics, 58 (1985) 4582-4586.